Sustainable Building Materials and Technologies 2020

Lead Guest Editor: Nadezda Stevulova
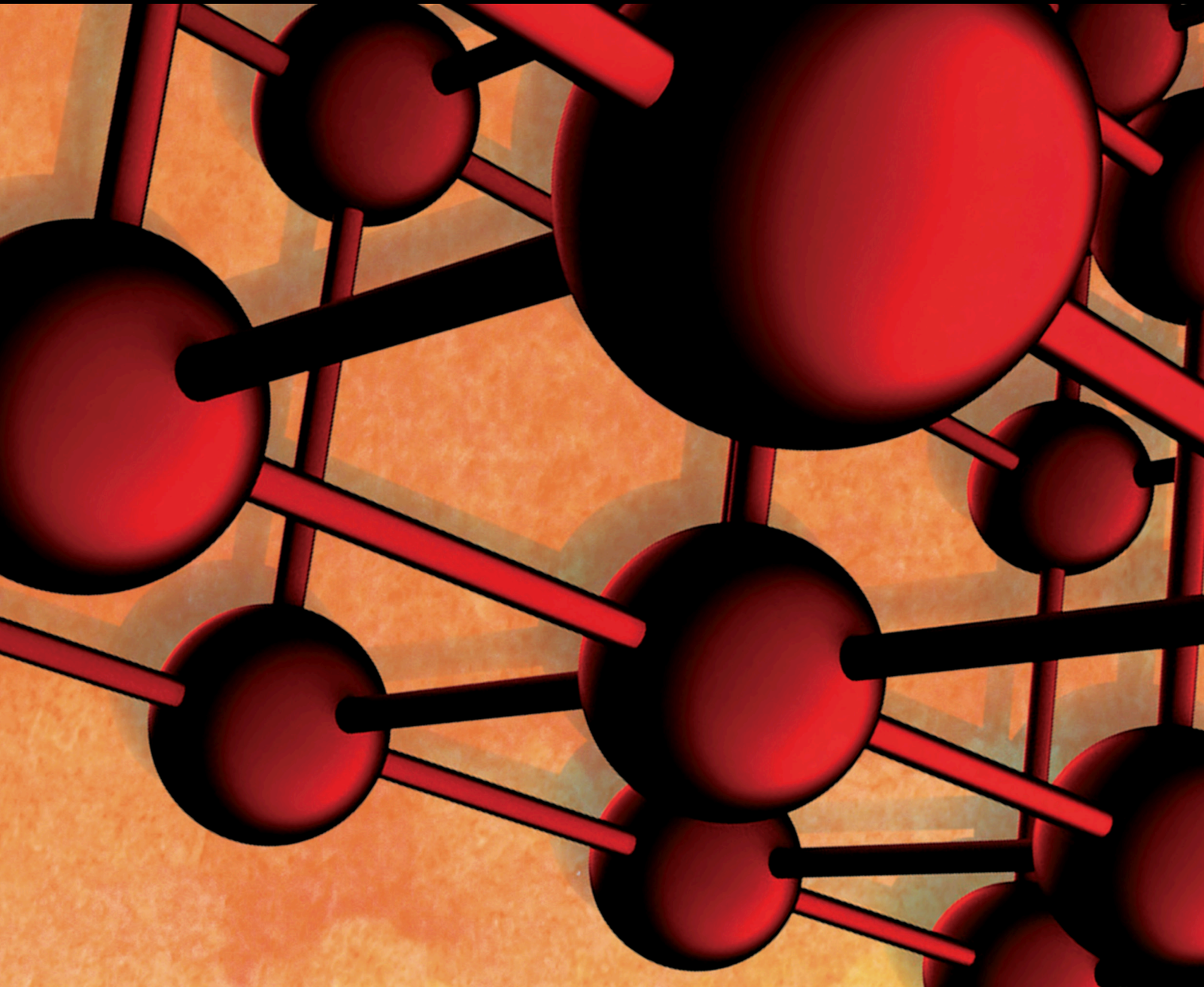Guest Editors: Kestutys Baltakys, Adriana Estokova, Vojtěch Václavík, and Sanja Dimter

Sustainable Building Materials and Technologies 2020

Sustainable Building Materials and Technologies 2020

Lead Guest Editor: Nadezda Stevulova
Guest Editors: Kestutys Baltakys, Adriana Estokova,
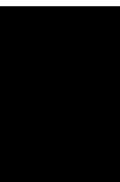Vojtěch Václavík, and Sanja Dimter

Fernando Rubio-Marcos, Spain
Francesco Ruffino, Italy
Mark H. Rümmeli, China
Pietro Russo, Italy
F.H. Samuel, Canada
MariaGabriella Santonicola, Italy
Hélder A. Santos, Finland
Carlo Santulli, Italy
Fabrizio Sarasini, Italy
Michael J. Schu#tze, Germany
Raffaele Sepe, Italy
Mercedes Solla, Spain
Donato Sorgente, Italy
Charles C. Sorrell, Australia
Andres Sotelo, Spain
Damien Soulat, France
Adolfo Speghini, Italy
Antonino Squillace, Italy
Koichi Sugimoto, Japan
Sam-Shajing Sun, USA
Baozhong Sun, China
Youhong Tang, Australia
Shengwen Tang, China
Kohji Tashiro, Japan
Hao Tong, China
Miguel Angel Torres, Spain
Laszlo Toth, France
Achim Trampert, Germany
Tomasz Trzepieciński, Poland
Matjaz Valant, Slovenia
Luca Valentini, Italy
Lijing Wang, Australia
Zhongchang Wang, Portugal
Jörg M. K. Wiezorek, USA
Jiang Wu, China
Guoqiang Xie, China
Jinyang Xu, China
Zhonghua Yao, China
Yee-wen Yen, Taiwan
Wenbin Yi, China
Hao Yi, China
Tetsu Yonezawa, Japan
Hiroshi Yoshihara, Japan
Lenka Zaji#c#kova#, Czech Republic
Zhigang Zang, China
Michele Zappalorto, Italy
Jinghuai Zhang, China

Gang Zhang, Singapore
Mikhail Zheludkevich, Germany
Wei Zhou, China
You Zhou, Japan
Hongtao Zhu, Australia

Contents

Editorial

Sustainable Building Materials and Technologies 2020

Nadezda Stevulova [ID],[1] **Kestutys Baltakys** [ID],[2] **Adriana Estokova** [ID],[1] **Vojtech Vaclavik** [ID],[3] **and Sanja Dimter** [ID][4]

[1]*Technical University of Kosice, Kosice, Slovakia*
[2]*Kaunas University of Technology, Kaunas, Lithuania*
[3]*VSB-Technical University of Ostrava, Ostrava, Czech Republic*
[4]*Josip Juraj Strossmayer University of Osijek, Osijek, Croatia*

Correspondence should be addressed to Nadezda Stevulova; nadezda.stevulova@tuke.sk

Construction material production has a great impact on the depletion of natural resources and greenhouse gas emissions caused by fossil fuel combustion, thus affecting global climate change and ozone depletion. On the other hand, building materials are largely determining the energy consumption in buildings and having environmental impacts. The goal for sustainable future in building material production is development of new environmentally friendly materials and constructions for sustainable buildings securing long-term environmental, economic, and social viability.

Therefore, the main aim of this Special Issue was to provide a platform for publishing the latest knowledge about application of sustainability as one of the most important topics in development of sustainable building materials and technologies. Although call for papers included a wide range of potential topics, the Special Issue *Sustainable Building Materials and Technologies 2020* contains only 7 papers addressed to advances in application of supplementary cementitious materials as alternative binder components in concrete. The utilization of industrial waste, by-products, and vegetal fibres incorporated into cement mortar/concrete for hydration process, strength development, and durability improvement of high performance concrete is analysed in detail in some papers bringing innovative integrated solutions to key building materials.

The authors W. J. Cho et al. summarize recent research results about the potential utilization of ferronickel slag (FNS) as a supplementary cementitious material. The investigation of the effects of FNS use on mortar and concrete properties showed that replacement of cement by FNS resulted in the increase in setting times and workability by delaying the hydration process, in the formation of a more dense pore structure compared with cement mix, in an increase in compressive strength at the long-term curing ages, and in improvement of resistance to chloride penetration and sulfate attack due to the secondary hydration reactions creating C-S-H gel and hydrotalcite.

The behavior of calcined magnesium-based mineral powder as a potential alternative resource for the production of magnesium-based binder was investigated by G. Sugila Devi and K. Sudalaimani. Paste made of powdered thermally treated (1200°C) mineral mixture consisting of natural magnesite and steatite in a ratio of 3 : 1 with water and with and without addition of sodium tripolyphosphate salt was tested for its microscopic structural development, consistency, initial setting time, final setting time, and heat of hydration. As shown in the results, adding phosphate salt led to formation of hydration products such as magnesium hydroxide and struvite and to an increase in setting time and compressive strength.

The utilization of four waste materials such as fly ash, circulating fluidized bed combustion ash, and slag as mineral admixtures in different amounts (up to 30 wt.%) and 9 wt.% addition of silica fume into high-performance concrete (HPC) and their influence on the mechanical properties and durability of HPC were evaluated by Z. Cheng et al. Variation of mineral admixtures in concrete samples led to the

achievement of compressive strength values higher than 60 MPa after 28 days of hardening depending on the waste kind. Among all three admixtures, HPC with circulating fluidized bed combustion ash had the best frost resistance.

The effects of replacing fine aggregates with different contents of coal bottom ash (up to 100%) on the strength properties of high-strength concrete (>60 MPa) at curing ages of 28 and 56 days were investigated by In-H. Yang et al. The samples reached the level of high-strength concrete, and coal bottom ash could be utilized for fabrication of high-strength concrete as a partial or total substitution for fine aggregates. Equations for predicting the strength values of coal bottom ash concrete by using the ultrasonic pulse velocity were suggested.

H. Danso investigated the influence of incorporation of plantain pseudostem fibre (up to 1 wt.% of sand) and 10 wt.% cement replacement by lime on the physical and mechanical properties of cement mortars. An optimal fibre content of 0.25 wt.% is recommended for construction application.

E. Abu Zeiton with co-authors focused on the parameters affecting the properties of the generated hemihydrate and dihydrate after the 1st reaction cycle of hydration-dehydration process. Their major finding consisted of revealing the differences in the properties such as the particle size, specific surface area, surface morphology, and number of defects between the formed hemihydrate after the first hydration-dehydration compared to the unrecycled hemihydrate. The grinding process after the first hydration step and the calcination process responsible for increasing the number of defects on the crystal surface led to a change in setting time, microstructure, and compressive strength of the recycled hemihydrate.

T. Tofeti Lima and K. Yong Ann paid attention to recovering the concrete structures under chloride-induced corrosion by an efficient nondestructive treatment by three different electrolytes (tap water, calcium hydroxide, and lithium borate) applied temporarily to structures. Lithium borate was identified as the most efficient electrolyte for extracting chlorides, while calcium hydroxide had better performance on restoring the passive state after corrosion, healing the structure at another level, filling up possible cracks. The positive affect was also found due to a possible electrodeposition of the electrolyte ions on the cement matrix.

Conflicts of Interest

The Guest Editors declare that they have no conflicts of interest regarding the publication of this Special Issue.

Nadezda Stevulova
Kestutys Baltakys
Adriana Estokova
Vojtech Vaclavik
Sanja Dimter

Review Article

Characterization of Portland Cement Incorporated with FNS

Won Jung Cho [ID],[1] Min Jae Kim [ID],[2] and David Su Vin Lee[3]

[1]Department of Civil and Environmental System Engineering, Hanyang University, Ansan 15588, Republic of Korea
[2]Department of Civil, Environmental and Architectural Engineering, Korea University, Seoul 02841, Republic of Korea
[3]St. George's School, P.O. Box 1910, Newport, RI 02840-0190, USA

Correspondence should be addressed to Won Jung Cho; nelly91@hanyang.ac.kr

The potential use of ferronickel slag (FNS) as supplementary cementitious material has been widely researched in recent years. Although much research was carried out on utilizing FNS as a binder, its advantages and disadvantages are still not clear. To properly use FNS as a cement replacement, this paper summarizes the following. (1) Changes expected on the oxide composition of FNS powder are due to the forming ores, fluxing stone, and cooling method. (2) The decreasing of the hydration heat evolution rate was detected by hydration heat evolution test and this is due to the low content of CaO and Al_2O_3 component in FNS. (3) It was found that the incorporation of FNS forms a dense pore structure more than cement mix and this is due to the secondary hydration reactions. (4) Hydration characteristics of FNS were assessed by pozzolanic reactions unexpectedly detected and incorporation of FNS creates C-S-H gel and hydrotalcite. (5) The development of strength was tested by compressive strength, splitting tensile strength, and flexural strength. From the results, the reduction of compressive strength was detected at an early age but substantially increasing at the long-term curing ages. However, splitting tensile strength and flexural strength of concrete have shown various trends. (6) There is an improvement in the resistance to chloride penetration and sulfate attack while susceptible to carbonation. This is induced by the lowered pH in pore solution due to the reduction of $Ca(OH)_2$ by substituting FNS binder. Finally, (8) ternary blended mixtures with conventional cementitious materials are an option to properly use FNS as a binder.

1. Introduction

Ordinary Portland cement (OPC) has been widely used in various parts of the world until recently. However, technological advances and environmental problems have led to the increased use of other supplementary cementitious materials. Significantly, the environmental load on CO_2 emission, which arose from the cement production, is 4-5% out of the entire output of human beings, and it has become a considerable problem of construction [1]. Hence, Portland cement mixed with other materials, such as ground granulated blast furnace slag (GGBS) from pig iron smelting or fly ash from coal-fired power plants (PFA), have increased popularity. But, these traditional admixtures already cannot be easily obtained in many places due to the surge in use. Consequently, finding new construction materials is an important issue not only for the replacement of cement but also for complementation of conventional admixtures. From

this point of view, research on the direction in which ferronickel slag (FNS) can be used as a substitute for cement is actively conducted.

Ferronickel slag (FNS) is a by-product obtained from the primary industry of smelting of laterite ore in an electric arc furnace at a high temperature with a reducing agent for the production of ferronickel. It is assumed that 1 ton of ferronickel may generate about 14 tons of FNS [2–4]. In particular, 30 million tons of FNS is produced in China [5] and 2 million tons in South Korea annually [6].

The utilization of FNS in concrete has been studied as aggregate by using pelletized type [6]. Because of its characteristics of low absorption rate, dense structure, and high hardness, FNS is considered to be usable as a fine aggregate for concrete [7, 8] and road construction [9]. Recently, the strength properties of concrete [10] and alkali-silica reactivity due to the high content of amorphous silica in FNS [2, 11] have been studied. Also, durability characteristics of

mortar [12] and concrete [13] incorporating slag aggregate with traditional supplementary cementitious materials were examined.

Likewise, the physical properties of FNS are suitable to use as an alternative and in concrete [11]. Nevertheless, due to a significant silica amount, FNS has shown reactivity when used with cement or/and alkali in geopolymers [14]. As a result, most FNS are landfilled [6, 15] due to the potential reactivity and unexpected hazardous effect. And the disposal of FNS has been pointed out concerning heavy metal reaching on the landfill area [16] and health issues to the neighbors [17]. Thus, using the FNS wastes in concrete would be one solution to reduce the problem of a landfill and save energy in construction [6].

Though suspicious of its applicability, many studies about FNS as a binder reported good physical performance and reactivity. According to the literature [3], the replacement of cement with FNS increases the degree of polymerization of silica chains in C-S-H gel and improves the resistance of concrete to chloride ion penetration. Pozzolanic reaction of FNS was also observed in some studies [18, 19], in which, in other words, the arguments about soundness reactivity in FNS aggregate is in fact advantage of using FNS as binder since the reactivity is necessary for hydration [6]. Lately, to utilize ferronickel slag as a substitute material for cement, microhydration heat, flow, compressive strength, and drying shrinkage variations were investigated [20], which means that it can potentially perform as cementitious materials. Lately, the proper replacement ratio of FNS to replace OPC was also suggested at 20%, depending on fineness [21]. Therefore, the utilization of FNS can be beneficial to reduce cement production costs and less energy-consuming.

As stated above, recent studies show that there is a potential to utilize FNS as construction materials. However, the use of industrial by-products as cementitious materials may reveal different properties compared to conventional materials [22]. Moreover, its advantages and disadvantages as a cement replacement are not clearly determined, despite many research projects conducted in the field. Therefore, in order to properly use FNS, this paper summarizes recent research about using FNS as cementitious materials.

2. Characteristics of FNS as a Binder

2.1. Properties of FNS Powder.
The properties of FNS powder obtained from researches are tabulated in Table 1. FNS can be categorized into two categories. For example, FNS used in [15, 18] mainly consisted of SiO_2 and Fe_2O_2 while FNS used in other researches was generally composed of SiO_2, Fe_2O_2, and MgO. This can be explained because the composition of slag materials changes depending on the ores, fluxing stone, and cooling method. Generally, nickel slag generated from laterite ore contains a high amount of Fe_2O_3 and low MgO, whereas garnierite ore contains low Fe_2O_3 and high MgO [4]. Its minerals consist of crystalline phases such as enstatite, forsterite, fayalite, diopside, and spinel phase [11, 18, 23]. Generally, slag can be classified into their basicity index [6]. Nkinamubanzi et al. [24] suggest that the

potential reactivity of slag powder can be anticipated by calculating the simplest basicity coefficient of the raw materials from chemical composition. The basicity coefficient (CaO/SiO_2) of slag greater than 1 indicates higher reactivity since the formation of hydration products is possible under the alkali condition. Based on the suggested equation, the basicity ratio of FNS is seen around 0.01–0.66; thus, it can be assumed that FNS has low hydraulic reactivity.

Nowadays, ferronickel slag is usually categorized as electric furnace ferronickel slag and blast furnace ferronickel slag depending on the production process. The type of FNS used in references is also specified in Table 1. Figure 1 shows the shape of the electric arc furnace ferronickel slag (EFS) and blast furnace ferronickel slag (BFS). As shown in Figures 1(a) and 1(b), both EFS and BFS particles are irregular and exhibit light grey color, thus hard to distinguish. From the literature [3], EFS mainly consisted of SiO_2, Fe_2O_3, and MgO, while BFS are CaO, SiO_2, Al_2O_3, and MgO. Moreover, the CaO content in the EFS powders (1.01%–8.24%) is much lower than the BFS (22.50%–25.19%). Thus, types of FNS should be distinguished since the composition of these two types of FNS is significantly different. Moreover, in general, fineness is related to the operating condition and purpose of the application. Thus, the fineness of FNS used in research varied from 3,400 to 26,300, while the density of FNS ranged from 2.87 to 3.18, respectively. Moreover, in general, fineness is related to the operating condition and purpose of the application. Thus, the fineness of FNS used in research varied from 3,400 to 26,300 while the density of FNS ranged from 2.87 to 3.18, respectively.

2.2. Effect of FNS Properties of FNS Powder.
The hydration heat evolution is an exothermal chemical reaction based on the mineralogical composition of the cement composites. The reactivity of binders in the cement matrix can be estimated by observing the hydration heat evolution. The exothermic rate and cumulative hydration heat of cement mix with FNS were analysed using a TAM-Air isothermal calorimeter at a constant temperature of 25°C, according to ASTM C1702 [26]. The literature results are shown in Figure 2. Three electric arc furnace FNS powders (EFS1, EFS2, and EFS3) and two blast furnace FNS powders (BFS1 and BFS2) were used in this literature. The hydration process of FNS can be divided into three steps, which is similar to that of ordinary Portland cement. However, the second exothermic peak in the composite binders is obviously lower. As shown in Figure 1(b), the cumulative hydration heat curves of the binders containing the EFS powders are nearly identical, and the total heat released is much lower than the binders containing the BFS powders. This result may be arisen by the low content of active components, such as CaO and Al_2O_3, in the EFS powders. Therefore, the replacement of cement by FNS results in a decreased hydration heat evolution rate and a decreased second peak value compared to cement. Consequently, the use of FNS can reduce the amount of heat generation, which is relevant to the risk of thermal cracking in concrete and has important implications for using this material at the construction site.

TABLE 1: Chemical and physical properties of FNS as a binder.

| Oxides | References | | | | | |
	[3]	[6]	[15, 18]	[22]	[23]	[25]
SiO_2	29.95–50.48	40.46–40.81	41.18	37.47	48.23	51.0
Al_2O_3	3.08–26.31	2.65–3.64	5.98	21.37	3.59	2.20
Fe_2O_3	1.55–14.36	6.87–9.07	40.02	1.72	15.76	15.5
MgO	8.93–32.61	40.44–43.43	7.79	10.53	23.01	27.4
SO_3	0.04–1.31	0.26–0.53	0.64	0.32	0.50	0.1
CaO	1.01–25.19	3.61–6.60	4.12	24.82	6.28	0.6
Na_2O	0.12–0.32	0.02–0.04	0.09	—	—	—
K_2O	0.07–0.40	0.05–0.08	0.37	—	0.09	—
Cr_2O_3	1.37–2.47	0.73–0.95	2.75	—	—	—
NiO	0.02–0.19	0.02–0.05	0.13	—	—	—
LOI	—	−3.44		0.68	—	—
Physical characteristics						
Fineness (cm^2/g)	3,910–4,610	4,660–26,300	3,985	—	3,400	4,666
Density (g/cm^3)	2.87–2.97	3.02–3.05	3.18	—	3.14	3.05
Source (type)	China (electric arc furnace, blast furnace)	South Korea (electric arc furnace)	Greece (electric arc furnace)	China (—)	South Korea (electric arc furnace)	South Korea (—)
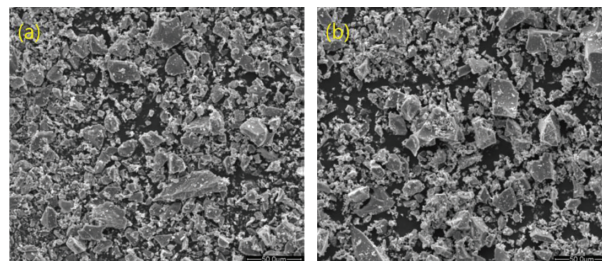
FIGURE 1: Morphology of FNS: (a) EFS and (b) BFS [3].
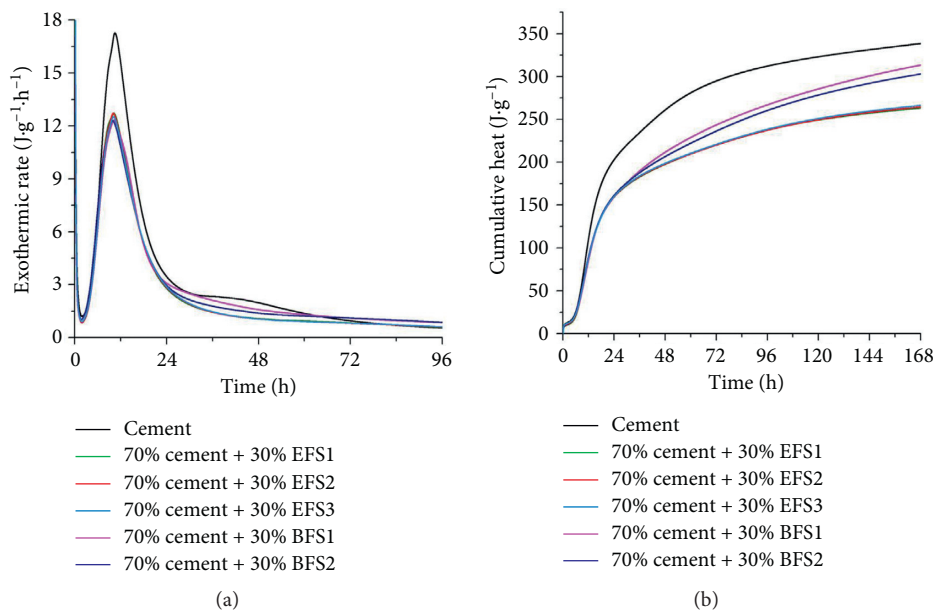
FIGURE 2: Effects of FNS on cement hydration kinetics. (a) Exothermic rate and (b) cumulative heat [3].

2.3. Effect on Pore Structure. Hydration reactions are attributed to the pore structure, and porosity generally decreases with age in the curing condition for cementitious materials [27]. For an evaluation of porosity in the cement matrix, many test methods, such as X-ray tomography, nitrogen adsorption, and nuclear magnetic resonance (NMR), have been applied. However, the mercury intrusion porosimetry (MIP) is the most conventionally used test to identify the pore structure of the cement matrix. Literature [3] applied MIP to the hardened FNS paste and divided the pore structure into four ranges: gel micropores (<4.5 nm), mesoporous (4.5–50 nm), middle capillary pores (50–100 nm), and large capillary pores (>100 nm). Then, by using a replacement ration of 30% in the cement paste with a blast furnace FNS, a similar range of large capillary pores volume was observed compared to OPC paste. Thus, it was suggested that it contributed to an improvement in the densification of the pore structure [6]. On the other hand, [28] classified the pore structure as macropore (>10 nm); large capillary (0.5–10 nm); small capillary (0.01–0.5 nm); and gel (<0.01 nm). Based on their classification, they suggested that the high fineness of FNS made the pore structure denser by ball bearing effect and presence of hydrotalcite. In addition, [25] also studied the MIP test results of 30% FNS paste at different curing ages. Results obtained at the curing age of 28 days and 90 days had a porosity of 30.12% and 29.13%, respectively. From the test results, the authors stated that the secondary hydration reaction of FNS creates C-S-H gel and hydrotalcite; subsequently, it induces the reduction of macropores. Thus, it was confirmed that the incorporation of FNS forms a dense pore structure and new hydration products due to the secondary reactions.

2.4. Effect of FNS on Fresh State. The concrete mix should have enough workability to facilitate the pouring and casting work at the construction site. The determination of the normal mortar flow was carried out according to ASTM C1437 [29]. Table 2 presents the fresh concrete properties of blended mix with FNS. The FNS containing cement demanded relatively less water than OPC, and the authors suggested that less water demand was attributed to the delayed hydration of slag. The flow tests confirmed the above results and showed that FNS addition improves the mortar workability. It was found that the replacement of cement with the less reactive admixtures leads to reduced amounts of hydration products formed during the early hydration stages, thus resulting in higher workability of the mortar.

The setting times of mixtures in literature [18, 30] were determined following the European Standard EN 196-3 [31] and Australian Standards [32] while [6] followed a standard test method [33]. All blended cement showed relatively longer setting times, rather than OPC. And the setting time generally increased with the increment of the percentage of the admixtures. The initial and final setting times for the highest FNS substituted specimen were found to be up to 140 min longer than those of OPC. The addition of FNS is then expected to delay the hydration process and increase

setting times, a fact that was confirmed by the results of the flow tests.

3. Physical Properties of FNS Mortar and Concrete

3.1. Compressive Strength. In the hardened state, for mortar and concrete containing supplement cementitious materials, compressive strength primarily depends on the replacement ratio, water-to-binder ratio, amount of cementitious materials, curing type, and curing age. The compressive strength results at 28 days of curing age for different FNS content mortar and concrete were collected from research papers and are presented in Figure 3. It clearly shows that compressive strength for FNS mortar and concrete was strongly dependent on FNS content; an increased replacement of cement by FNS resulted in a reduction in the compressive strength for FNS mortars. The blended cement containing 30% FNS substitution presented the lowest compressive strength in all previous research. In particular, [6] showed a strongly reduced compressive strength in a mix with 30% FNS, only 30.17 MPa, while the lower substitution rates of 5 and 10% accounted for 34.6–36.24 MPa, respectively. However, it is crucial to consider that the FNS used in their study had different fineness; for example, the fineness accounted for 4,660 cm^2/g at 30% replacement while 8,600 cm^2/g at 10% and 26,300 cm^2/g at 5%.

Furthermore, due to the replacement of clinker in cement by supplementary cementitious materials, the mixture further extends that curing age should be accompanied [34]. To evaluate the relationship between the development of compressive strength and curing ages, [18, 25] monitored the compressive strength at a later age with FNS contents varying as 5, 10, 15, 20, and 30%, as given in Figure 4. As shown in Figure 4, all FNS mortars developed relatively lower strength than OPC at all curing ages. However, the curve of 5% FNS from 28 days to 91 days shows an almost identical curve with OPC. Thus, it can be assumed that FNS showed less reactivity and retarded development of compressive strength. Moreover, at later ages, the gap between OPC and FNS mortars and concrete was gradually reduced. For example, the compressive strength of FNS mortars at 91 days was 62.8, 60.1, 59.1, and 58.2 MPa for 5, 10, 15, and 20% FNS, respectively, while OPC reached 63.5 MPa. Reference [25] found that the strength activity of 30% FNS mortar at 28 and 91 days was 79 and 86% while 95 and 100% for concrete, respectively. This result indicates that the reactivity increases over curing. Thus, it is evident that compressive strength for FNS mortar and concrete is strongly dependent on curing ages, which imply latent hydraulic or pozzolanic reaction.

3.2. Diverse Strength. Although the advantage of reduced water demand in the FNS mix was reported, low water-to-binder ratio induced delayed setting time and low early age strength. However, the enhancing effect of FNS concrete in strength development was reported by [6], as shown in Figure 5. These strength values were more or less in a limited range to OPC, depending on the fineness of FNS. As for the

TABLE 2: Summary of properties of FNS cement at the fresh state.

Reference (specimen)	Water-to-binder ratio	FNS content (%)	Water demand (%)	Flow (%)	Setting time (minute)	
					Initial	Final
[6] (mortar)	0.5	0	—	—	392	541
[6] (mortar)	0.5	5	—	—	433	557
[6] (mortar)	0.5	10	—	—	485	612
[6] (mortar)	0.5	30	—	—	493	680
[18] (paste)	0.25	0	27.8	97.5	145	185
[18] (paste)	0.25	5	27.6	100.2	150	195
[18] (paste)	0.25	10	27.0	104.7	160	200
[18] (paste)	0.25	15	26.5	107.9	170	215
[18] (paste)	0.25	20	26.1	110.5	175	220
[30] (paste)	0.5	0	30.0	—	130	190
[30] (paste)	0.5	20	29.0	—	130	200
[30] (paste)	0.5	30	28.0	—	130	200
[30] (paste)	0.5	40	27.5	—	140	200
[30] (paste)	0.5	50	27.0	—	130	200
[30] (paste)	0.5	65	27.0	—	150	230
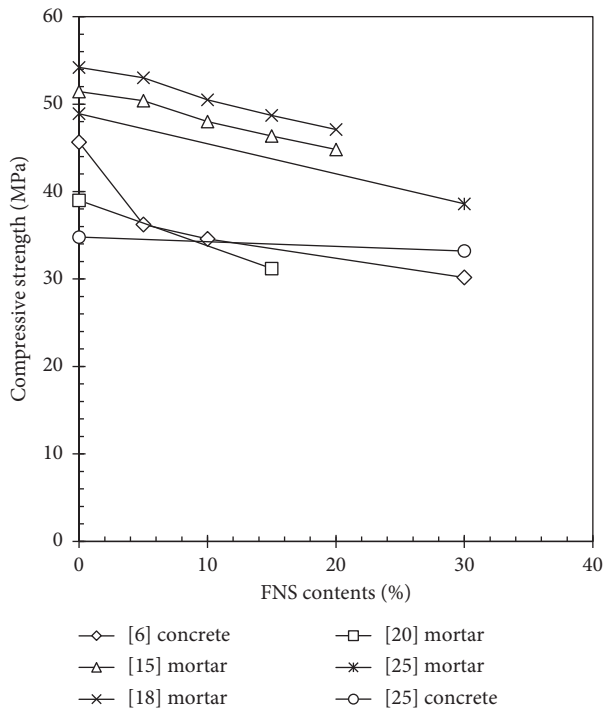
FIGURE 3: Compressive strength at 28 days of curing ages.

- —◇— [6] concrete
- —△— [15] mortar
- —✕— [18] mortar
- —□— [20] mortar
- —✳— [25] mortar
- —○— [25] concrete

FIGURE 4: Compressive strength at different ages.

- —◇— [18] (OPC mortar)
- —□— [18] (5 wt% FNS mortar)
- —△— [18] (10 wt% FNS mortar)
- —✕— [18] (15 wt% FNS mortar)
- —✳— [18] (20 wt% FNS mortar)
- ● [25] (OPC mortar)
- + [25] (30 wt% FNS Mortar)
- ■ [25] (OPC concrete)
- ▲ [25] (30 wt% FNS concrete)

flexural and splitting tensile strength, an increase in the fineness of FNS increased the strengths. On the contrary, the FNS concrete benefited against OPC ones in producing the shear strength; all mixes for FNS increased the shear strength by about 14.9–16.1% points to the original value of 7.85 MPa. This study suggested that due to limited hydraulic reactivity, a large margin of FNS could be used in filling-up voids and pores in cement paste and even at the interfacial region between aggregate and paste. Thus, the strength development of the FNS mortar and concrete significantly altered by a combination of replacement ratio and fineness.

4. Durability of FNS Mortar and Concrete

4.1. Influence on Physical Properties of FNS Mix. After hardening, even though concrete is well designed, it can expand and crack. The main reasons for this unsoundness are caused by the MgO hydrates or strains induced by shrinkage. Due to the high content of MgO in FNS, a soundness test is necessary for using FNS as a binder. Moreover, investigation of the risk of drying shrinkage can confirm the reduction effect of FNS on the hydration heat
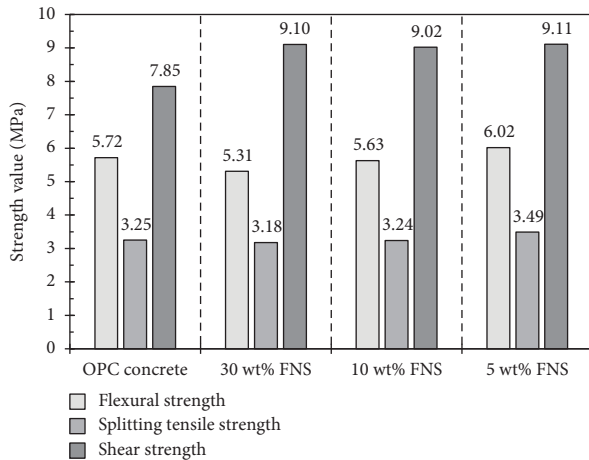
FIGURE 5: Strength characteristics of FNS concrete at flexural, splitting tensile, and shear strengths [6].

generation and water demand, which has been stated in some literature [3]. The autoclave expansion and drying shrinkage test were evaluated by [6, 30]. The autoclave expansion test, especially, is designed for measuring the potentially deleterious expansion by free MgO (periclase). According to [30], the autoclave expansion was not observed. Due to the reason that the MgO in FNS is in the form of crystalline, forsterite rather than free MgO, the autoclave expansion was not shown in FNS mortar. Reference [6] stated that the incorporation of FNS showed distinctively low drying shrinkage compared to OPC. The authors also added that high amount replacement of FNS instead of OPC could reduce microcracks in mass concrete structures, resulting in reduced maintenance cost.

4.2. Resistance to Chemical Degradation.

To assess the resistance of FNS concrete against chloride ion penetrability, many researchers conducted rapid chloride penetration resistance (RCPT) [35]. Reference [3] reported that the pozzolanic reaction due to the addition of FNS dramatically improves the resistance of the concrete to chloride ion penetration. The studies conducted by [6] also confirmed the high resistivity of FNS in chloride attack. According to [6], the denser pore structure in FNS concrete restricts pore connectivity for external chloride ions, and then the corrosion risk would decrease.

Additionally, reference [6] observed that a high replacement ratio of low fineness FNS appears to be the most resistive after sulfate attack. During hydration, the unhydrated FNS clinkers might further have formed hydrotalcite consuming ettringite, one of the problematic hydrates in concrete structure due to volume expansion if sulfate attack is applied. This improvement of sulfate attack resistivity happens as a factor of the previous stated latent hydraulic and pozzolanic reactivity of FNS.

However, a high replacement of cement by cementitious materials may induce carbonation. Reference [6] investigated the carbonation depth of FNS mortar and stated that the FNS binder had a more dangerous aspect of carbonation

than OPC. According to the literature, the principal reason is the lowered pH in pore solution due to the reduction of $Ca(OH)_2$ by substituting the FNS binder. Also, low CaO content in the FNS compound was attributed to the extreme condition of calcium carbonate formation accompanied by high SiO_2 content, which requires $Ca(OH)_2$ to consume.

4.3. Ternary Blended Cement Containing FNS.

To compensate for the disadvantages of the FNS binder, [18, 20, 23, 36] investigated ternary binders. It was found that ternary binders present relatively lower strength at all ages compared to OPC though the latter increased at later curing ages. The authors suggested that the reduction of strength development is attributed to the pozzolanic reaction at later ages. Reference [20] examined the characteristics of ternary mortar, including FNS with GGBS and PFA, replaced at 15% of cement weight. That study has shown that similar flow value and drying shrinkage were expected compared to binary mix with 100% replacement of FNS, while lower values are seen compared to OPC. Reference [18] investigated mixtures containing up to 20% of cement weight with FNS and/or natural pozzolans. They also concluded that delayed hydration and pozzolanic reaction appeared with the formation of secondary calcium silicate hydrate gel in the binary and ternary mix with FNS. Reference [23] studied the chemical reaction and performance of ternary blended binders by mixing FNS and PFA. It was confirmed that C-S-H gel was formed more than only PFA was mixed by the pozzolanic reaction of FNS and PFA. Reference [36] also states that the ternary mix using FNS and GGBS contributed to the dense pore structure. Likewise, ternary binders with conventional cementitious materials and FNS can optimize the properties of the FNS mix.

4.4. Summary and Future Research.

A summary of the test results of incorporating FNS as a binder is displayed in Table 3. The fresh concrete properties of FNS blends demanded relatively less water than OPC, and the flow tests confirmed FNS addition improves the mortar workability. In the case of setting time, the initial setting was delayed at least 3% to a maximum 26% while the final setting was increased at least 3% to a maximum 26%. The setting time results showed a large difference when compared between references, but a typical one shows that the hardening process is delayed when FNS is mixed.

As a result of measuring the compressive strength, it showed a tendency to decrease compared to OPC concrete varying from 1% to 33%, while there was a case where it increased depending on the fineness or curing age. Although FNS incorporation in the cement mix resulted in a decreased compressive strength compared to OPC, the difference was not significant.

As for diverse strength, tensile and splitting tensile strength values were more or less in a limited range to OPC while enhancing shear strength. Based on the strength development, the FNS mix has a high potential for structural concrete, considering that it accompanies a further reinforcement to compensate for the weakness.

TABLE 3: Summary of results for the incorporation of FNS in Portland cement as a binder.

Experiment	References				
	[3]	[6]	[15, 18]	[25]	[30]
Flow	—	—	↑	—	—
Water demand	—	—	↑	—	↑
Setting time	—	↑Initial (10–26%) ↑Final (3–26%)	↑Initial (3–21%) ↑Final (5–19%)	—	↑Initial (8–15%) ↑Final (5–21%)
Compressive strength	↓ (1.4–6.2%) or ↑ (0.8–4.9%)	↓(21%)	↓ (1–8%)	↓(14%) or ↑(100%)	↓(7–33%)
Flexural strength	—	Various	—	—	—
Splitting tensile strength	—	Various	—	—	—
Shear strength	—	Enhanced	—	—	—
Expansion	—	↓	↑(but moderate)	—	Moderate
Shrinkage	—	↓	—	—	—
Chloride resistance	Enhanced	Enhanced	—	—	—
Sulfate resistance	—	Various	—	—	—
Carbonation	—	↓	—	—	—

When it comes to durability, due to denser pore structure formation, the risk of penetration of external ions such as chlorides and sulfates will decrease. Especially for the case of sulfate attack, the high substitution of FNS is most resistive regarding consuming ettringite, which is one of the problematic hydrates if sulfate attack is applied. As seen in Table 3, carbonation was found to be a more dangerous aspect. And this is induced by the lowered pH in pore solution by replacing the FNS binder.

From the summary, the use of FNS has the potential to be a supplementary cementitious material and beneficial for the environment. It is evident that finding new cementitious materials is an urgent issue in the construction industry due to the demand for cement expected to increase. Currently, the utilization of FNS has been studied increasingly as a binder. Concerning the soundness reactivity, there is still caution of its application, but studies about FNS reported favorable environmental and physical performance. The leaching test conducted from [15] indicated that leachable heavy metals in FNS were substantially below the regulatory thresholds. Reference [30] reported that there is no soundness effect on the expansion.

The research that currently exists with respect to FNS use has reported that it has the potential to perform as cementitious materials. Cement with environmentally friendly materials such as FNS may become beneficial to be more employed. The benefits of cementitious materials application are not only constrained to the properties of concrete but also a significant reduction in economic and environmental costs [37]. Thus, FNS can be used as a binder with a positive effect on the environment. Notwithstanding the advantages of using industrial by-products, however, a study on the long-term durability and performance of FNS blends is not sufficient. As suggested in Table 3, recent research is insufficient for external environment resistance of concrete, such as freeze-thaw resistance and high alkali environments. Moreover, as shown in Table 1, the type of FNS used in references is not well documented. The difference in sources and manufacturing process produces a different chemical composition, although it has similar morphology. It is also important that MgO contained in FNS should not be confused as soundness because it is crystalline phases such as enstatite, forsterite, fayalite, diopside, and spinel phase [11, 18, 23] that are different from brucite $(Mg(OH)_2)$ which causes expansion. In other words, as CaO is divided by free CaO (lime), MgO must be divided by Free MgO. It should not be evaluated as suspicious without consideration of the form of oxide not only for utilizing FNS but also for improving the utility of industrial by-products as construction materials. Consequently, further research must be carried out to safely use and prevent inadequate properties of FNS.

5. Conclusion

This paper summarized the effects of FNS use on mortar and concrete properties, as shown in Table 3. And several insights have been gained through the conducted published literature:

(1) The composition of FNS powder changes depending on the ores, fluxing stone, and cooling method. Its minerals mainly consist of crystalline phases such as enstatite, forsterite, fayalite, diopside, and spinel phase due to the nickel ore.

(2) Based on the basicity coefficient equation, FNS has low hydraulic reactivity. Thus, the use of FNS can reduce the amount of heat generation that is relevant to the risk of thermal cracking in concrete. Also, the addition of FNS increases setting times and workability by delaying the hydration process.

(3) The replacement of cement by FNS results in an overall reduction in the compressive strength for FNS mortars and concrete. However, at later ages, the strength was gradually increased due to increased activity of FNS over curing.

(4) Limited hydraulic reactivity of FNS plays a role in a cement matrix as filling-up voids and pores in

cement paste and even at the interfacial region between aggregate and paste.

(5) Due to the presence of MgO in FNS in the form of crystalline rather than free MgO, no negative expansion was detected in the FNS mix. Furthermore, incorporation of FNS showed distinctively low drying shrinkage compared to mix with OPC only.

(6) The addition of FNS improves the resistance of concrete to chloride ion penetration and sulfate attack while it might be more vulnerable to carbonation due to the reduction of $Ca(OH)_2$ hydrates and a consequent reduction of pH.

(7) Ternary mix with conventional binders and FNS showed similar properties. Moreover, more C-S-H gel was formed in the ternary mix. The formation of additional C-S-H gel implies that the ternary mix may improve the properties of blended mixtures with FNS.

(8) Related to the FNS mix's performance, there is a lack of research for long-term durability and severe external resistance such as freeze-thaw resistance and a high alkaline environment. To properly use the FNS in the construction industry, further research should conduct.

(9) The oxide composition in FNS strongly depends on the sources and manufacturing process method. Therefore, the categorization of the FNS according to the chemical composition of the FNS should be conducted.

(10) MgO contained in FNS should not be confused as soundness because it is crystalline phases that are different from brucite ($Mg(OH)_2$) which causes expansion.

Data Availability

All data have been disclosed in this manuscript.

Conflicts of Interest

The authors declare that they have no known conflicts of financial interest or personal relationships that could have appeared to influence the work reported in this paper.

References

[1] P. K. Mehta and P. J. Monteiro, *Concrete Microstructure, Properties and Materials*, McGraw-Hill Education, New York, NY, USA, 2017.

[2] A. K. Saha and P. K. Sarker, "Expansion due to alkali-silica reaction of ferronickel slag fine aggregate in OPC and blended cement mortars," *Construction and Building Materials*, vol. 123, pp. 135–142, 2016.

[3] Y. Huang, Q. Wang, and M. Shi, "Characteristics and reactivity of ferronickel slag powder," *Construction and Building Materials*, vol. 156, pp. 773–789, 2017.

[4] A. K. Saha, M. N. N. Khan, and P. K. Sarker, "Value added utilization of by-product electric furnace ferronickel slag as

construction materials: a review," *Resources, Conservation and Recycling*, vol. 134, pp. 10–24, 2018.

[5] L. Pang, Z. Ma, and Y. Xie, "Preliminary study on the preparation of self-compacting concrete used by ferronickel slag micro powder," in *Proceedings of the 1st Conference on Solid Wastes Utilization and Eco-Materials*, pp. 68–72, Beijing, China, 2015.

[6] H. Kim, C. H. Lee, and K. Y. Ann, "Feasibility of ferronickel slag powder for cementitious binder in concrete mix," *Construction and Building Materials*, vol. 207, pp. 693–705, 2019.

[7] Y. Sakoi, M. Aba, Y. Tsukinaga, and S. Nagataki, "Properties of concrete used in ferronickel slag aggregate," in *Proceedings of the 3rd International Conference on Sustainable Construction Materials and Technologies*, pp. 1–6, Tokyo, Japan, 2013.

[8] JIS A 5011-2, *Slag Aggregate for Concrete—Part 2: Ferronickel Slag Aggregate*, Japanese Industrial Standards Committee, Tokyo, Japan, 2016.

[9] JIS A 5015, *Iron and Steel Slag for Road Construction*, Japanese Industrial Standards Committee, Tokyo, Japan, 2013.

[10] A. K. Saha and P. K. Sarker, "Compressive strength of mortar containing ferronickel slag as replacement of natural sand," *Procedia Engineering*, vol. 171, pp. 689–694, 2017.

[11] Y. C. Choi and S. Choi, "Alkali-silica reactivity of cementitious materials using ferro-nickel slag fine aggregates produced in different cooling conditions," *Construction and Building Materials*, vol. 99, pp. 279–287, 2015.

[12] A. K. Saha and P. K. Sarker, "Durability of mortar incorporating ferronickel slag aggregate and supplementary cementitious materials subjected to wet-dry cycles," *International Journal of Concrete Structures and Materials*, vol. 12, no. 1, pp. 1–12, 2018a.

[13] A. K. Saha and P. K. Sarker, "Durability characteristics of concrete using ferronickel slag fine aggregate and fly ash," *Magazine of Concrete Research*, vol. 70, no. 17, pp. 865–874, 2018b.

[14] I. Maragkos, I. P. Giannopoulou, and D. Panias, "Synthesis of ferronickel slag-based geopolymers," *Minerals Engineering*, vol. 22, no. 2, pp. 196–203, 2009.

[15] N. S. Katsiotis, P. E. Tsakiridis, D. Velissariou, M. S. Katsiotis, S. M. Alhassan, and M. Beazi, "Utilization of ferronickel slag as additive in Portland cement: a hydration leaching study," *Waste and Biomass Valorization*, vol. 6, no. 2, pp. 177–189, 2015.

[16] S. Kang, K. Park, and D. Kim, "Potential soil contamination in areas where ferronickel slag is used for reclamation work," *Materials*, vol. 7, no. 10, pp. 7157–7172, 2014.

[17] C. Han and Y.-C. Hong, "Adverse health effects of ferronickel manufacturing factory on local residents: an interrupted time series analysis," *Environment International*, vol. 114, pp. 288–296, 2018.

[18] N. Lemonis, P. E. Tsakiridis, N. S. Katsiotis et al., "Hydration study of ternary blended cements containing ferronickel slag and natural pozzolan," *Construction and Building Materials*, vol. 81, pp. 130–139, 2015.

[19] L. Mo, F. Zhang, M. Deng, F. Jin, A. Al-Tabbaa, and A. Wang, "Accelerated carbonation and performance of concrete made with steel slag as binding materials and aggregates," *Cement and Concrete Composites*, vol. 83, pp. 138–145, 2017.

[20] B.-S. Cho, K.-M. Koo, S.-J. Choi, and S. J. Choi, "Effect of ferronickel slag powder on microhydration heat, flow, compressive strength, and drying shrinkage of mortar," *Advances in Civil Engineering*, vol. 2018, Article ID 6420238, 7 pages, 2018.

[21] T. Yang, X. Yao, and Z. Zhang, "Geopolymer prepared with high-magnesium nickel slag: characterization of properties and microstructure," *Construction and Building Materials*, vol. 59, pp. 188–194, 2014.

[22] A. Qi, X. Liu, Z. Wang, and Z. Chen, "Mechanical properties of the concrete containing ferronickel slag and blast furnace slag powder," *Construction and Building Materials*, vol. 231, Article ID 117120, 2020.

[23] W.-J. Cho and K.-Y. Ann, "A study on the hydration characteristics and fundamental properties of ternary blended cement using ferronickel slag and fly ash," *Journal of the Korea Concrete Institute*, vol. 32, no. 1, pp. 27–35, 2020.

[24] P. C. Nkinamubanzi, M. Baalbaki, J. Bickley, and P. C. Aitcin, "The use of slag for making high performance concrete," in *Proceedings of the 6th NCB International Seminar on Cement and Bulding Materials*, New Delhi, India, 1998.

[25] C.-H. Lee, S.-C. Kim, Y.-J. Kim, S.-K. Kim, J.-P. Hwang, and J.-W. Park, "Experimental study on thermal conductivity of concrete using ferronickel slag powder," *KSCE Journal of Civil Engineering*, vol. 24, no. 1, pp. 219–227, 2020.

[26] ASTM C1702-15b, *Standard Test Method for Measurement of Heat of Hydration of Hydraulic Cementitious Materials Using Isothermal Conduction Calorimetry*, American Society for Testing and Materials, West Conshohocken, PA, USA, 2015.

[27] H.-W. Song, S.-W. Pack, C.-H. Lee, and S.-J. Kwon, "Service life prediction of concrete structures under marine environment considering coupled deterioration," *Restoration of Buildings and Monuments*, vol. 12, no. 4, pp. 265–284, 2006.

[28] S. Mindess, J. F. Young, and D. Darwin, *Concrete*, Prentice-Hall, Englewood Cliffs, NJ, USA, 1981.

[29] American Society for Testing and Materials-ASTM and ASTM C1437, *Standard Test Method for Flow of Hydraulic Cement Mortar*, ASTM International, West Conshohocken, PA, USA, 1999.

[30] M. A. Rahman, P. K. Sarker, F. U. A. Shaikh, and A. K. Saha, "Soundness and compressive strength of Portland cement blended with ground granulated ferronickel slag," *Construction and Building Materials*, vol. 140, pp. 194–202, 2017.

[31] EN 196-3, *Methods of Testing Cement-Determination of Setting Time and Soundness*, British Standards Institution, London, UK, 1995.

[32] AS/NZS 2350.4, *Methods of Testing Portland and Blended Cements—Setting Time of Portland and Blended Cements*, Standards Australia, Sydney, Australia, 1999.

[33] American Society for Testing and Materials, *ASTM C 403: Standard Test Method for Time of Setting of Concrete Mixture by Penetration Resistance*, American Society for Testing and Materials, West Conshohocken, PA, USA, 1999.

[34] I. Odler, "Hydration, setting and hardening of portland cement," *Lea's Chemistry of Cement and Concrete*, Elsevier, Amsterdam, Netherlands, 1998.

[35] ASTM, *Standard Test Method for Electrical Indication of Concrete's Ability to Resist Chloride Ion Penetration*, ASTM, West Conshohocken, PA, USA, 2012.

[36] W. J. Cho, H. S. Kim, and K. Y. Ann, "A study on the hydration characteristics and fundamental properties of ternary blended cement using ferronickel slag," *Journal of the Korean Recycled Construction Resources Institute*, vol. 8, no. 1, pp. 39–48, 2020.

[37] J. M. Paris, J. G. Roessler, C. C. Ferraro, H. D. DeFord, and T. G. Townsend, "A review of waste products utilized as supplements to Portland cement in concrete," *Journal of Cleaner Production*, vol. 121, pp. 1–18, 2016.

Research Article

Mechanical Properties and Durability of High-Performance Concretes Blended with Circulating Fluidized Bed Combustion Ash and Slag as Replacement for Ordinary Portland Cement

Zhi Cheng [ID], Lei He [ID], Lan Liu [ID], Zhijun Cheng [ID], Xiaobo Pei, and Zhe Ma

School of Science, North University of China, Taiyuan 030051, China

Correspondence should be addressed to Lan Liu; yunvlan@163.com

This study investigates the mechanical properties and durability of three families of high-performance concrete (HPC), in which the first was blended with fly ash, the second with circulating fluidized bed combustion (CFBC) ash, and the third with CFBC slag. In addition to each of the three mineral additives, silica fume and a superplasticizer were also incorporated into the HPC. Hence, three families of HPC, containing 10%, 20%, and 30% mineral admixtures and 9% silica fume of the binder mass, respectively, were produced. The microstructure and hydration products of the HPC families were examined by scanning electron microscopy (SEM) and X-ray diffraction (XRD) to explore the influence of fly ash, CFBC ash, and CFBC slag on the compressive strength and frost resistance of HPC. The experimental results show that the compressive strength of HPC could reach 60 MPa at 28 d age. When the fly ash content was 30%, the compressive strength of HPC was 70.2 MPa at 28 d age; after the freeze-thaw cycle, the mass loss and strength loss of HPC were 0.63% and 8.9%, respectively. When the CFBC ash content was 20%, the compressive strength of HPC was 75 MPa at 28 d age. After the freeze-thaw cycle, the mass loss and strength loss of HPC were 0.17% and 0.81%, respectively.

1. Introduction

Coal-fired power generation in traditional thermal power plants results in the emission of a large amount of sulfur dioxide (SO_2), causing serious environmental pollution [1]. By using the circulating fluidized bed combustion (CFBC) technology, which has a higher combustion and desulfurization efficiency, SO_2 emission can be greatly reduced. Therefore, this technology has been vigorously promoted in China [2–4]. In this technique, limestone is added as a desulfurizer to the CFBC boiler, so that the boiler discharges a greater amount of ash and slag compared with the pulverized coal boiler [5–7]. Currently, more than 50 million tons of CFBC ash and slag are discharged annually in China [8–10]. As studies on the CFBC ash and CFBC slag are few, CFBC ash and CFBC slag are still not used on a large scale [11–14]. Ash and slag pollute the environment while occupying the land; therefore, governments and power plants

have sought effective methods to dispose them [15–18], especially since the environmental protection tax law was enacted on January 1, 2018.

With the development in the concrete industry, high-performance concrete (HPC), a material with very low porosity, has received great attention due to its excellent mechanical properties and durability [19–21]. To improve the properties of HPC, mineral admixtures with high pozzolanic reactivity, such as silica fume and ground granulated slags, are usually added [22–24]. Mineral admixtures have gradually become a research focus, and fly ash has become one of the main mineral admixtures [25–27].

Fly ash, which is discharged from pulverized coal boilers, has been intensively and widely researched. With the same as fly ash, CFBC ash and CFBC slag also contain some amount of SiO_2 and AlO_3. So, the CFBC ash and CFBC slag have pozzolanic activity too [28]. Abed and Nemes [29] investigated the influence of fly ash on self-compacting HPC and found that the

concrete containing 15% fly ash had better durability performance. Xu et al. [30] researched the effect of fineness and the CFBC ash composition on compressive strength, setting time, and consistency of basic magnesium sulfate cement and observed that with an increase in the fineness of CFBC ash, the consistency of the cement paste increased, the setting time shortened, and the compressive strength slightly improved; this indicates that fine CFBC ash is a good raw material for preparing basic magnesium sulfate cement. Nguyen et al. [31] studied the engineering performance and durability of concrete modified with CFBC ash so that it contained a high volume of low-calcium fly ash. The experiment results showed that the CFBC ash addition did not influence the stability and passing and filling abilities of concrete. However, CFBC ash could significantly improve the compressive strength, bonding property, and durability of concrete.

The CFBC ash and CFBC slag contain some amount of f-CaO and II-CaSO$_4$. Excessive f-CaO and II-CaSO4 will cause concrete damage due to volume expansion in the later stage [32–34]. To eliminate this adverse effect, CFBC ash and CFBC slag should be modified by physical or chemical methods. Studies have shown that physical grinding can decrease the volume expansion of the concrete while increasing the activity of the admixtures [35]. In this study, to prepare HPC, fly ash, CFBC ash, and ground CFBC slag were used as admixtures to replace cement. The influences of different admixtures on the mechanical properties and durability of HPC were also explored. The research results can provide a new basis and reference for the utilization of CFBC ash and slag and the preparation of HPC.

2. Materials and Methods

2.1. Materials. Grade PO 42.5 Portland cement (PC) from the Zhihai Cement Plant was used in this experiment. Its density was 3.100 g/cm^3, and its specific surface area was 357 m^2/kg. Its physical properties are presented in Table 1.

Fly ash (II), which was raw ash from the Taiyuan second thermal power plant, was used in this work. Moreover, CFBC ash and CFBC slag were also used and were obtained from the Pingshuo Coal Gangue Power Plant of Shanxi Province, China. Ground CFBC slag was prepared by grinding the raw CFBC slag for 39 min. The chemical compositions of cement, fly ash, CFBC ash, and CFBC slag are presented in Table 2. Silica fume was also used and was obtained from the Langtian Silica Fume Factory in Sichuan Province, China. The main parameters of the silica fume are listed in Table 3.

Figures 1 and 2 show the scanning electron microscopic (SEM) micrographs and X-ray diffraction (XRD) patterns of fly ash, CFBC ash, and ground CFBC slag, respectively. As can be seen from the SEM micrographs, the CFBC ash particles were irregular, the surface was coarse and porous, and agglomeration was obvious. The ground CFBC slag also featured irregular and coarse and porous lumps, but fly ash particles were regularly spherical, smooth, and dense. The XRD patterns show the presence of quartz, anhydrite, f-CaO, hematite, and calcite in the fly ash, CFBC ash, and CFBC slag. However, fly ash also contained mullite.

The fine aggregate was natural river sand (S) with a fineness modulus of 2.8 and apparent density of 2.65 g/cm^3. The coarse aggregate was crushed limestone with a particle size of 5–20 mm and an apparent density of 2.79 g/cm^3.

Polycarboxylate superplasticizer, produced by the Taiyuan concrete superplasticizer factory, was used as the water-reducing admixture. The water reduction rate was 34%.

2.2. Methods. In this study, a total of 9 groups of experiments were designed. Three concrete specimens were fabricated to test the compressive strength and frost resistance of each age. The values in Figures 3 and 4 are the average value of three concrete specimens. The mixture proportions are presented in Table 4. The water-to-binder ratio (W/B) was 0.3. Fly ash, CFBC ash, and ground CFBC slag were used to replace cement, at each of the three dosages of 10%, 20%, and 30%. The amount of silica fume was 9% of the total binder materials. A water-reducing admixture was used to adjust the slump flow. The slump flow values of all the HPCs were controlled within 550–655 mm, which belong to grade SF1.

In this study, the density was tested in accordance with GB/7208-2014 Cement Density Method. The chemical composition was referred to the chemical titration method in GB/T 176 Chemical Analysis Methods of Cement. The calculation method of activity index is carried out in accordance with GB/T 18046 Granulated Blast Furnace Slag Powder Used in Cement and Concrete. The specific surface area shall be determined in accordance with the GB/T 8074 Method for determination of the specific surface area of the cement Blaine method. The adsorption property of silica fume was characterized by the BET nitrogen adsorption method, and its specific surface area was obtained.

The working performance is carried out in accordance with JGJ/T283-2012 Technical Specification for Application of Self-compacting Concrete. According to the filling requirements of the self-compacting index performance, high-performance concrete is carried out with the performance level of SF$_1$; that is, it meets the requirement of no reinforcement from the top or a concrete structure with less reinforcement. This test strictly controls the slump expansion range from 550 to 655 mm.

In this study, the specimens were placed in a standard curing box with a temperature of $20 \pm 2^\circ$C and a relative humidity of more than 95% for curing. After 24 hours, the molds were taken out and demolded. After demoulding, the specimens were placed in $20 \pm 3^\circ$C water for curing and taken out after the specified age for relevant tests.

The compressive strength tests were performed using a 3000 kN universal compression machine in accordance with the GB/T 50081-2002 Standard Test Method for Mechanical Properties of Ordinary Concrete. In this study, $100 \times 100 \times 100$ mm cubes were tested. The compressive strength of concrete was tested at 3 d, 7 d, and 28 d ages, respectively.

The frost resistance property tests were formed using KDR-V9 concrete rapid freeze-thaw testing machine in

TABLE 1: Physical properties of the portland cement.

Specific surface area (m²/kg)	Setting time (min)		Flexural strength (MPa)			Compressive strength (MPa)		
	Initial setting time	Final setting time	3 d	7 d	28 d	3 d	7 d	28 d
357	21	241	5.5	7	8.7	26.1	29.6	50.3

TABLE 2: Chemical compositions of cement, fly ash, CFBC ash, and CFBC slag (wt. %).

Sample	SiO_2	Al_2O_3	Fe_2O_3	CaO	SO_3	MgO	K_2O	LOI (%)
Cement	20.84	4.14	3.35	65.88	2.80	1.89	0.60	—
Fly ash	47.50	30.37	3.97	5.83	0.93	0.48	0.69	3.43
CFBC ash	37.78	32.76	5.42	10.19	4.35	1.93	0.98	6.09
CFBC slag	40.29	32.11	3.77	10.27	3.89	1.43	1.05	6.52

TABLE 3: Main parameters of silica fume (wt. %).

SiO_2	Cl^-	Water demand ratio	Specific surface (m²/kg)	Activity index	Total alkalinity
95.00	0.012	113	23700	122	0.23

(a)

(b)

(c)
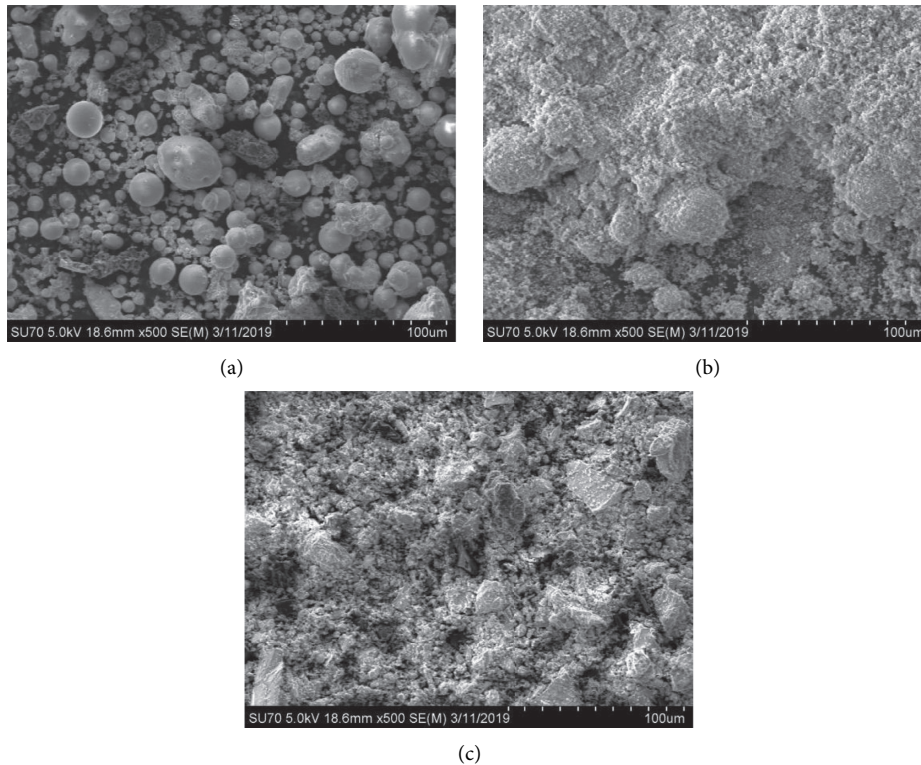
FIGURE 1: SEM micrographs of (a) fly ash, (b) CFBC ash, and (c) CFBC slag.

accordance with GB/T 50082-2009 Standard Test Methods for Long-Term Performance and Durability of Ordinary Concrete. In this study, $100 \times 100 \times 100$ mm cubes were tested. In this test, 25 freeze-thaw cycles are used as a group. After each cycle is taken out of the instrument, its mass is weighed. Stop the test when the mass loss rate exceeds 5%, the compressive strength loss rate exceeds 25%, or 50 freeze-thaw cycles are reached.

The XRD patterns were detected using the D/max-RB XRD system (Japan Rigaku Corporation, Tokyo, Japan). The

microstructures were detected using SEM (Hitachi S 4800 and SU-70; Hitachi, Ltd., Tokyo, Japan).

3. Results and Discussion

3.1. Mechanical Properties of HPC. The compressive strength of HPC specimens is illustrated in Figure 3. For all of the specimens, the compressive strength at 3 d ages reached 40 MPa, indicating early strength characteristics. The compressive strength of S4–S8 reached 80 MPa at 90 d ages.
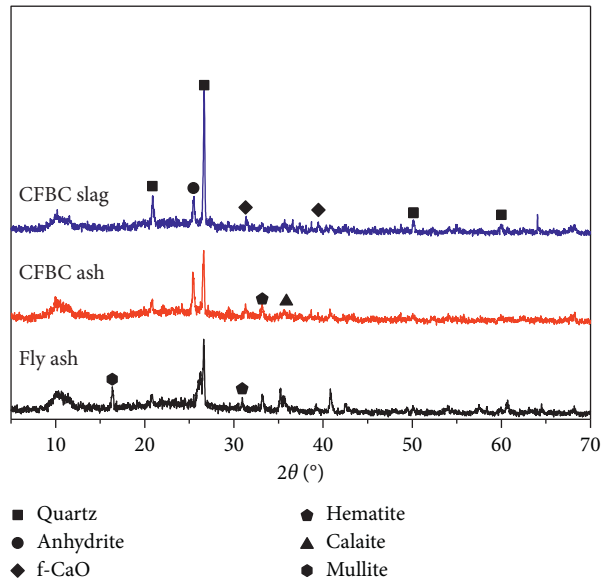
FIGURE 2: XRD patterns of fly ash, CFBC ash, and CFBC slag.

(a)

(b)

FIGURE 3: Continued.
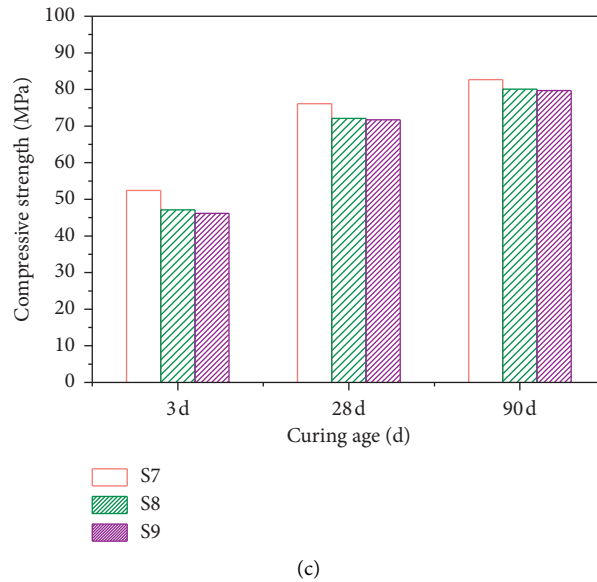
(c)

FIGURE 3: Compressive strength of HPC with different mineral admixtures. (a) Fly ash; (b) CFBC ash; (c) CFBC slag.

For ordinary concrete (without adding fly ash, CFBC ash, and CFBC slag), W/B is 0.3, silica fume content is 9%, and its 28 d ages compressive strength exceeds 70 MPa [36]. When the W/B is 0.3 and the silica fume content is 10%, the compressive strength at 28 d ages exceeds 80 MPa [37, 38]. Compared with ordinary concrete, the 28 d ages compressive strength of concrete mixed with fly ash, CFBC ash and CFBC slag is slightly lower. But the compressive strength of S1–S9 specimens at 28 d ages could reach 60 MPa, which belongs to high-strength concrete. As shown in Figure 3(a), with the increase in the amount of fly ash, the compressive strength of HPC decreased continuously. It can be seen from Figure 3(b) that with the increase of the CFBC ash amount, the compressive strength of HPC first increased and then decreased. According to Figure 3(c), with the increase of the amount of CFBC slag, the compressive strength of HPC decreased continuously. From Figure 3, the effect of mineral admixtures on the compressive strength of concrete is more obvious. The D-value between the maximum and minimum of the 3 d ages compressive strength of fly ash, CFBC ash, and CFBC slag is greater than 10%. But in the later curing age, the effect on strength is not obvious.

It can be seen from Figure 4(a) that when the admixture amount was 10%, the compressive strength of HPC with CFBC slag was higher than that of the other HPCs at 3 d and 90 d ages. Figure 4(b) shows that when the admixture amount was 20%, the compressive strength of the HPC with CFBC ash was higher than that of the other HPC at all ages. According to Figure 4(c), when the amount was 30%, the compressive strength of the HPC with CFBC ash was the highest at the 3 d and 90 d ages. And when the amount was 30%, the compressive strength of the HPC with CFBC slag was the highest at the 28 d ages. These indicate that the medium-term strength developed slowly when the amount of CFBC ash was 30%.

The XRD patterns of HPCs with different mineral admixtures are shown in Figure 5. As can be seen from the figure, the hydration products of HPC mainly included hydrated calcium silicate gel, gypsum, calcium hydroxide, and ettringite. Calcite appears in Figure 5 for two reasons: on the one hand, it comes from the coarse aggregate. On the other hand, it comes from the unreacted limestone residue in the CFBC ash and CFBC slag; that is, the limestone that is not completely thermally decomposed during the CFBC. It can be seen that as the age increases, the XRD peak intensity of $Ca(OH)_2$ decreases, whereas the XRD peak intensity of gypsum increases. The main reaction of calcium hydroxide was to produce a C-S-H gel and react with gypsum to form ettringite, whereby C-S-H gel and ettringite are the main materials to form the strength of the cementitious system [39, 40]. In addition, the ground CFBC slag is conducive to maximize the activities of various substances [41, 42]. As shown in Figure 6, large amounts of gypsum and C-S-H gel were found.

3.2. Frost Resistance of HPC. Figure 7 illustrates that as the amount of admixture increases, the compressive strength and mass loss rate of HPC first decreased and then increased. When the amount was 20%, the strength and mass loss rate of HPC were the minimum, and the frost resistance was the highest. For the HPC with fly ash, fly ash particles can evenly fill internal pores at the early age to block water channels, and hydration products generated by the secondary hydration reaction in the later age can improve the pore structure while filling pores, thereby improving the frost resistance of HPC. However, when the fly ash amount is too high, the proportion of cement decreases, resulting in a large reduction in gel, ettringite, and so on, and therefore, the internal pores

(a)

(b)

(c)
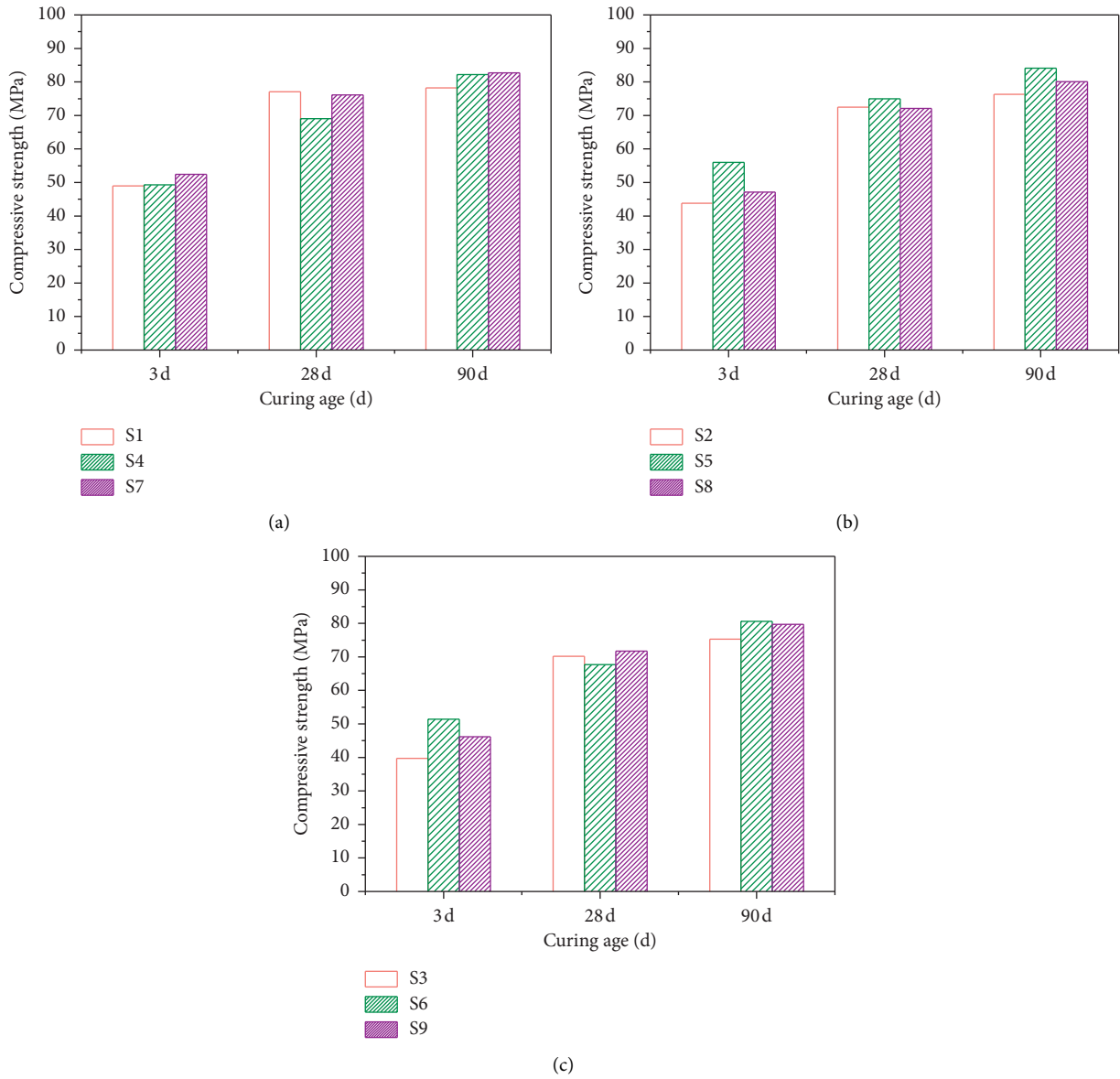
Figure 4: Compressive strength of HPC with different amounts of mineral admixtures. (a) 10%; (b) 20%; (c) 30%.

Table 4: Mixture proportions of HPC (kg/m^3).

Mixture	W/B	Fine aggregate	Coarse aggregate	Fly ash	CFBC ash	CFBC slag	Silica fume	Cement	Water-reducing admixture
S1	0.3	790	890	56	—	—	50.4	453.6	6.16
S2	0.3	790	890	112	—	—	50.4	397.6	6.72
S3	0.3	790	890	168	—	—	50.4	341.6	7.84
S4	0.3	790	890	—	56	—	50.4	453.6	5.6
S5	0.3	790	890	—	112	—	50.4	397.6	7.28
S6	0.3	790	890	—	168	—	50.4	341.6	8.4
S7	0.3	790	890	—	—	56	50.4	453.6	5.6
S8	0.3	790	890	—	—	112	50.4	397.6	6.72
S9	0.3	790	890	—	—	168	50.4	341.6	10.08

(a)

(b)

(c)

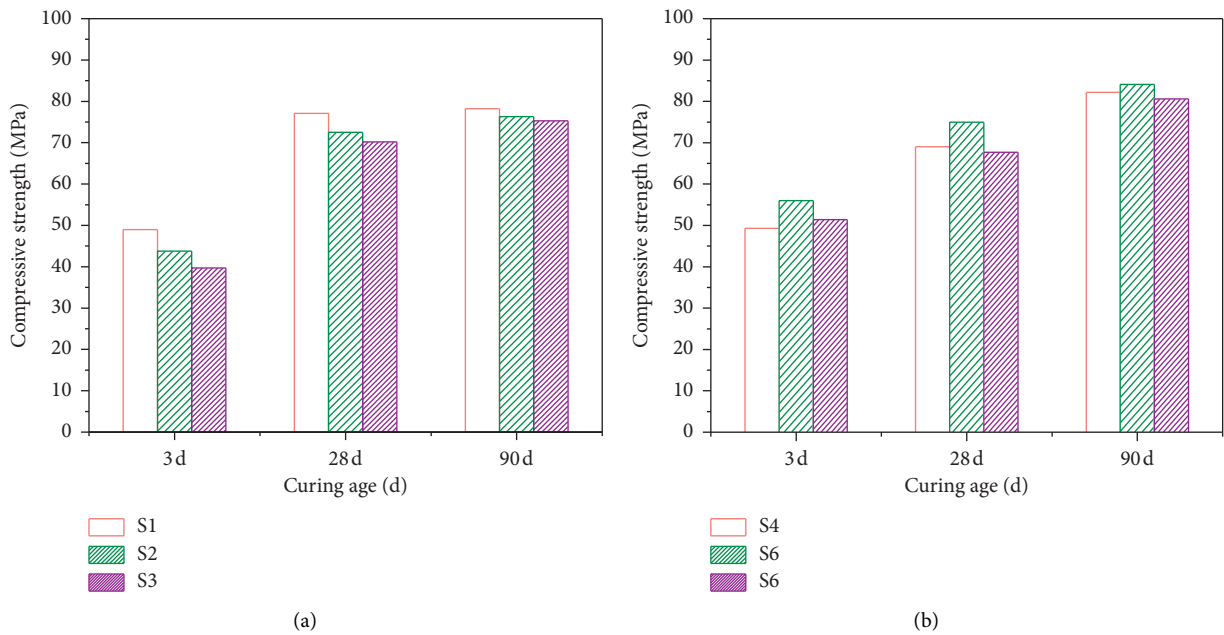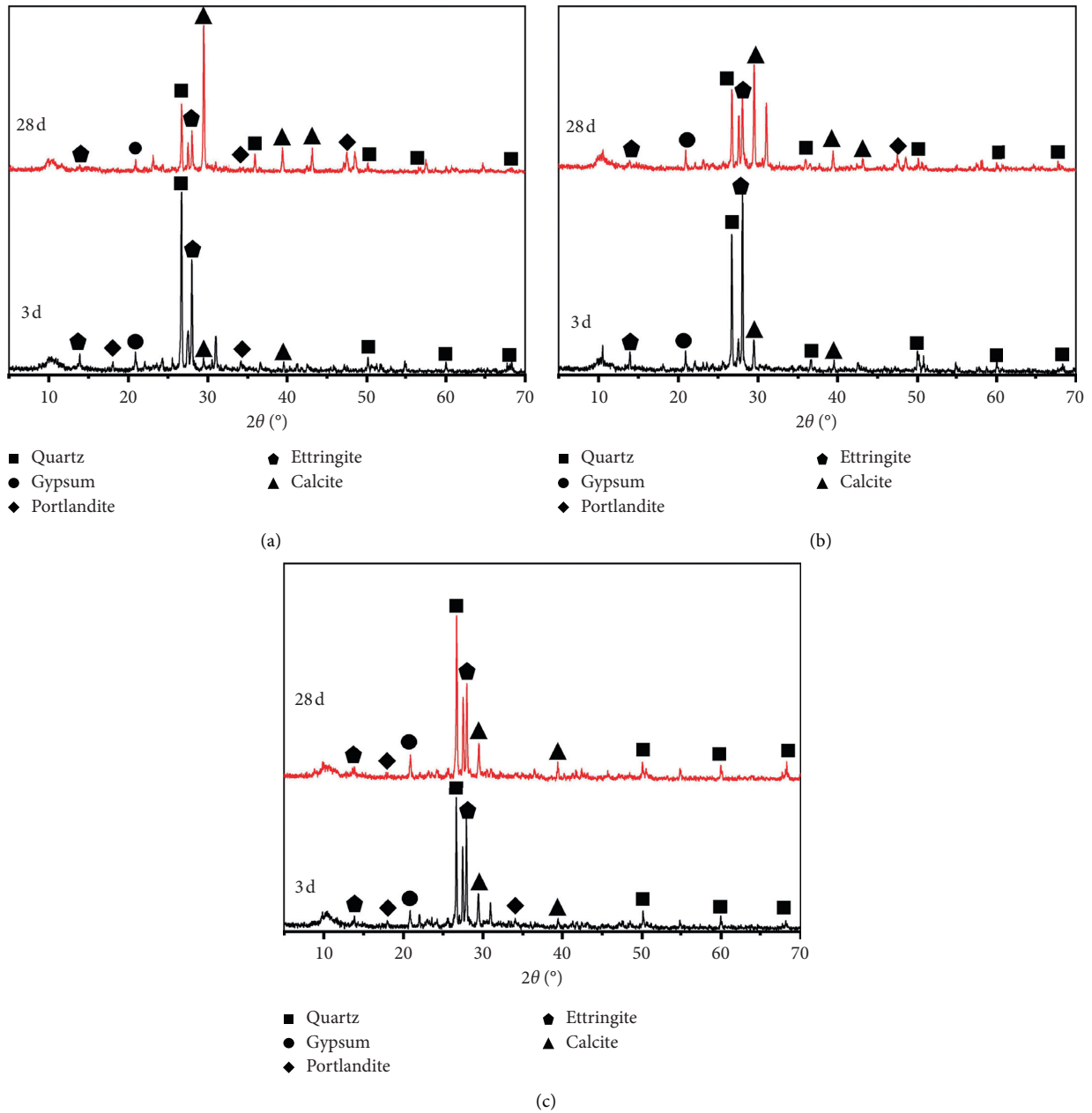Figure 5: XRD pattern of HPC with different mineral admixtures. (a) Fly ash; (b) CFBC ash; (c) CFBC slag.

(a)

(b)
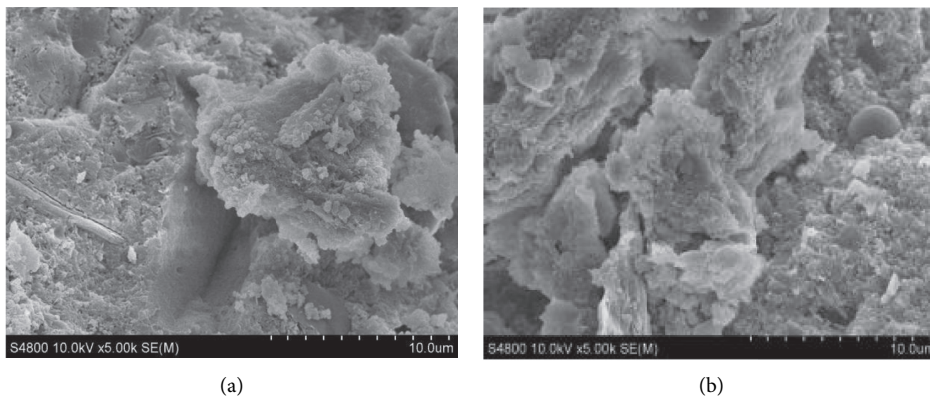
Figure 6: Continued.
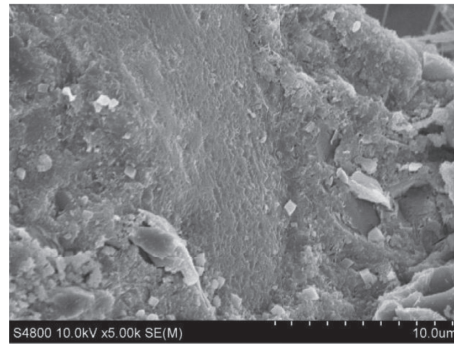
(c)

FIGURE 6: SEM of HPC with different mineral admixtures. (a) Fly ash; (b) CFBC ash; (c) CFBC slag.

(a)

(b)

(c)
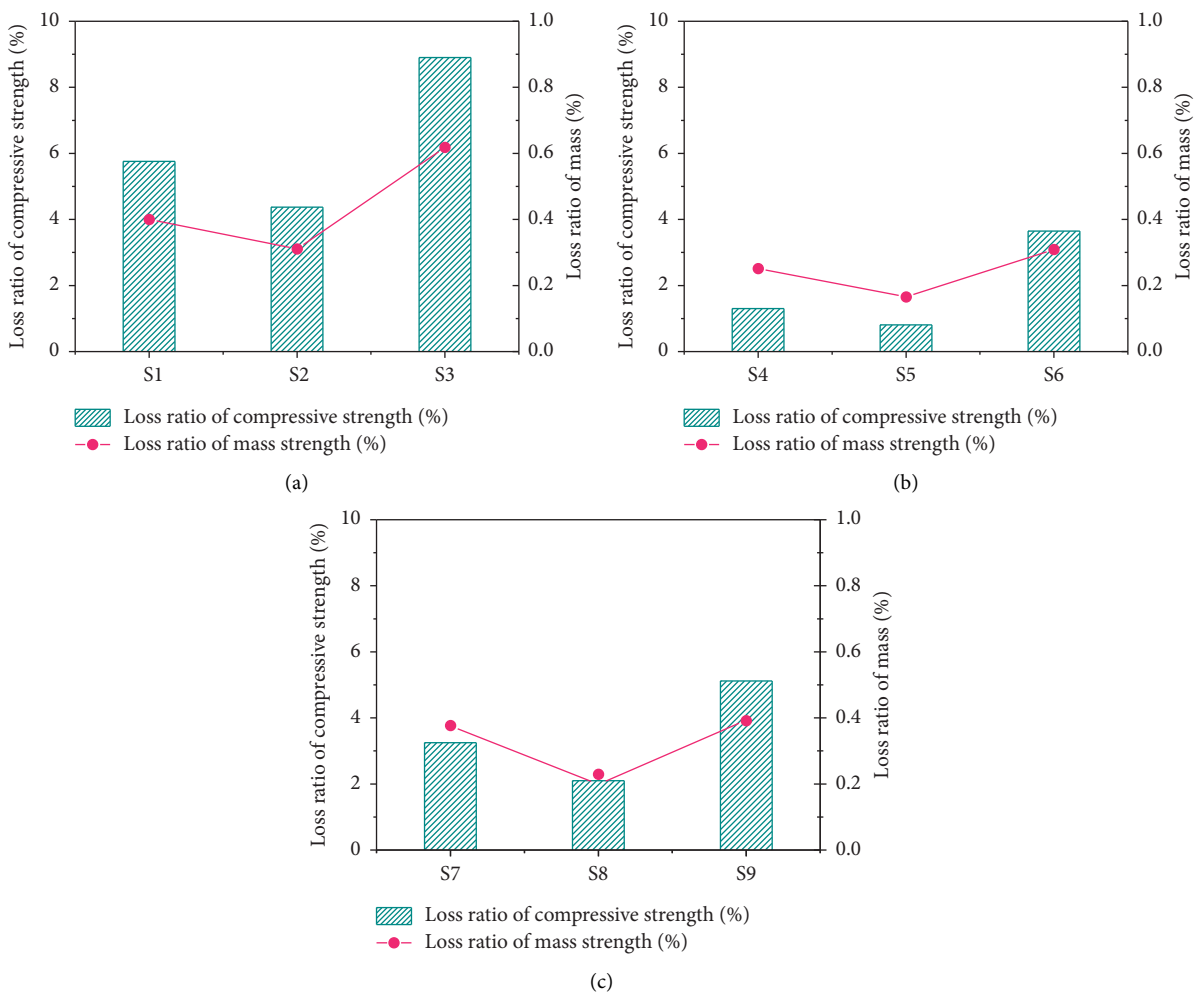
FIGURE 7: Compressive strength and mass loss rate of HPC with different mineral admixtures. (a) Fly ash; (b) CFBC ash; (c) CFBC slag.

cannot be filled. The amount of $Ca(OH)_2$ produced is not enough to support the secondary hydration reaction of fly ash, resulting in a reduction in the strength and frost resistance of HPC [43].

The CFBC ash and CFBC slag all contain f-CaO and II-$CaSO_4$, which can react to form hydration products and

chemically react with other mineral components to form C-S-H gel and ettringite. And this will cause the strength of the concrete to increase rapidly and the expansion will develop inward [35], thus greatly improving the compactness of the HPC by blocking the interior water passages. Therefore, the frost resistance of the HPC improved.

(a)

(b)

(c)
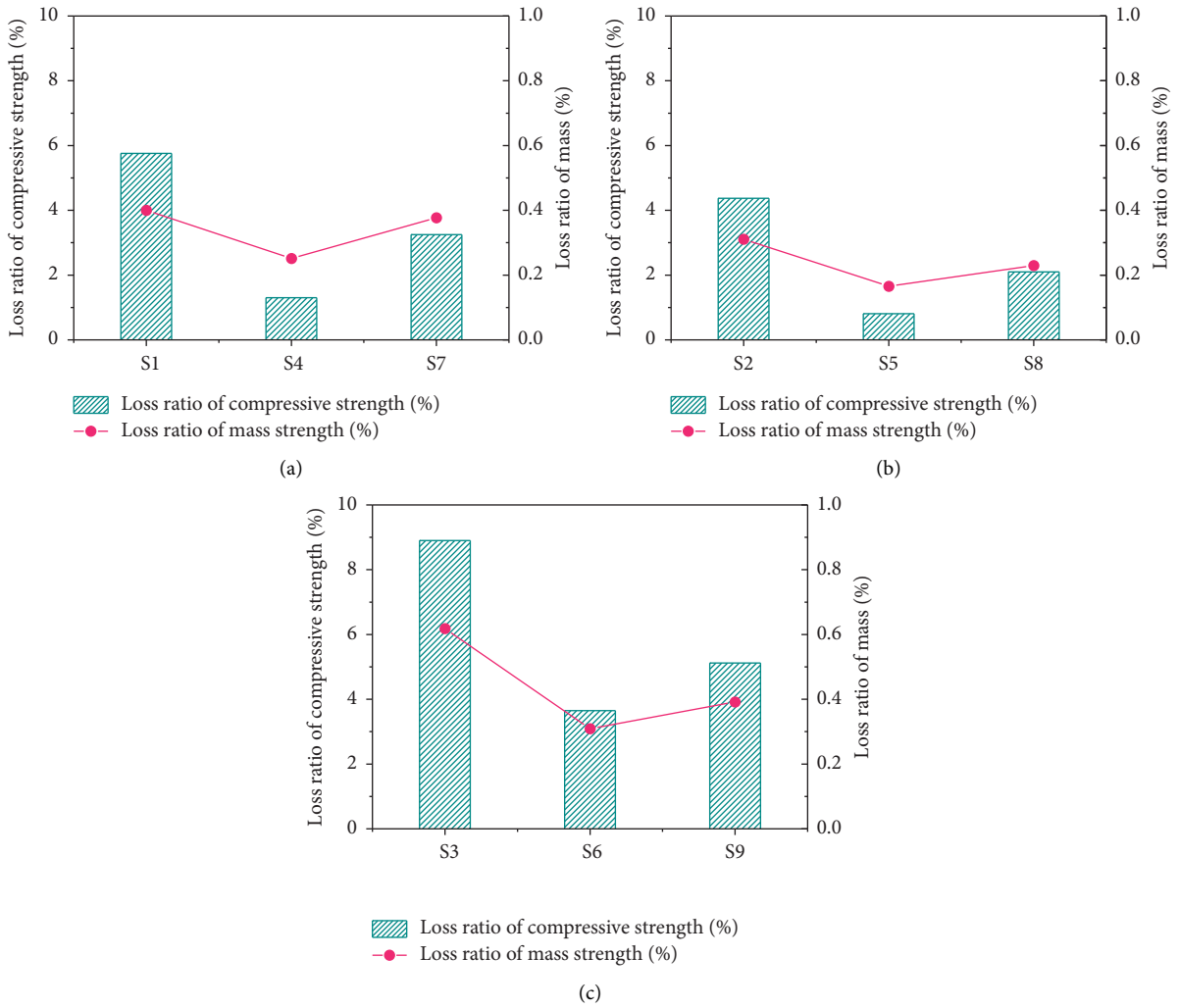
FIGURE 8: Compressive strength and mass loss rate of HPC different amounts of mineral admixtures. (a) 10%, (b) 20%, (c) 30%.

(a)

(b)
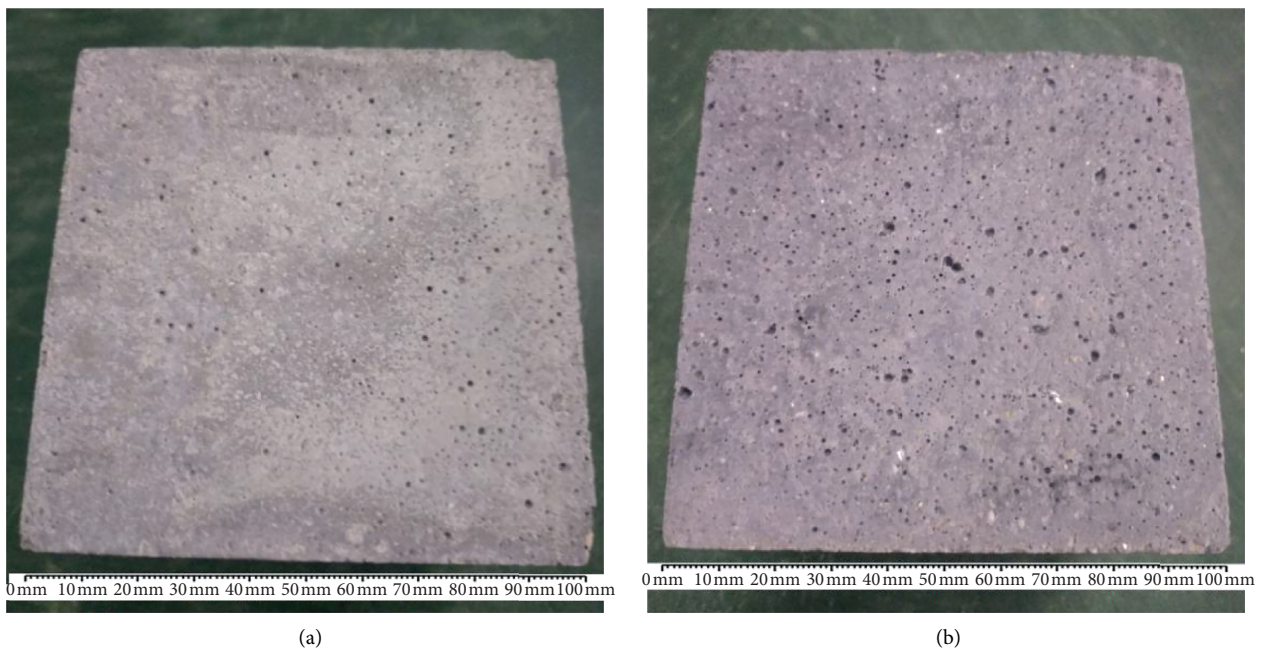
FIGURE 9: HPC surface after 50 times freeze-thaw cycles. (a) Before; (b) after.

Further, due to the relatively coarse and porous structure of CFBC ash and CFBC slag and the large number of internal pores, both played the role of air-entraining agents; thus, the frost resistance of the HPC was improved. However, when the CFBC ash and CFBC slag amount are too high, the proportion of cement decreases. Moreover, the amount of gel produced is reduced, the working performance of the HPC declines, and the internal compactness is insufficient. In the case of insufficient alkalinity in the later age, the internal components are easy to decompose; as a result, the pore structure changes and the frost resistance decreases.

Uysal et al. research shows that concrete mixed with fly ash can effectively improve the frost resistance of concrete [44, 45]. As shown in Figure 8, the strength and mass loss rate of the HPC with fly ash were much higher than those of the other HPCs. It can be seen that, for all additive amounts, the HPC with CFBC ash had the best frost resistance compared with the other HPCs. Compared with the CFBC ash and CFBC slag, the early activity of fly ash was inadequate, and the expansion performances of CFBC ash and CFBC slag were mainly concentrated at the early age. A large number of expansion materials are formed, and they fill the internal pores of HPC, improving the pore structure and making the interior of HPC more compact and frost resistant. The physical appearances of HPC after 50 times freeze-thaw cycles are shown in Figure 9. After 50 times the freeze-thaw cycle, many pores appeared on the HPC surface, and the previously existing pores became larger, which was the main reason for the decrease in mass and strength.

4. Conclusions

(1) It is feasible to prepare high-performance concrete using fly ash, CFBC ash, and CFBC slag as mineral admixtures. The high-performance concretes can be prepared by mixing fly ash, CFBC ash, CFBC slag, and 9% silica fume with the amount of 10%, 20%, and 30%. The compressive strength can reach more than 60 MPa at 28 d ages. After 50 times freeze-thaw cycles, the mass loss and strength loss are low, no more than 0.7% and 0.9%.

(2) The varieties and amounts of mineral admixtures have obvious effects on the early compressive strength of high-performance concrete but have little effect in the later period of curing. The law of the fly ash and CFBC slag's amount on the HPCs' compressive strength is the same. While the amounts of the fly ash and CFBC slag increase, the HPCs' compressive strength decreases at each age. When the content of fly ash and CFBC slag is 10%, the compressive strength reaches the maximum at each age. While the amount of CFBC ash increases, the compressive strength of the HPC first increases and then decreases at each age. When the amount is 20% of CFBC ash, the compressive strength reaches the maximum at each age.

(3) There are same laws for the frost resistance of HPCs with fly ash, CFBC ash, and CFBC slag. When the amount is 20%, the frost resistance is the best. Among all three admixtures, HPC with CFBC ash has the best frost resistance.

Data Availability

The data used to support the findings of this study are included within the article and the supplementary information file.

Conflicts of Interest

The authors declare that they have no conflicts of interest.

Supplementary Materials

Figure S1: the images of CFBC ash, CFBC slag, and fly ash. Figure S2: the photos of freeze-thaw cycle test. Tables S1–S4: the data of the compressive strength of HPC. Tables S5–S7: the data of the compressive strength and mass loss of HPC after the freezing-thawing cycle in 28 d ages. (*Supplementary Materials*)

References

[1] X.-G. Li, Q.-B. Chen, K.-Z. Huang, B.-G. Ma, and B. Wu, "Cementitious properties and hydration mechanism of circulating fluidized bed combustion (CFBC) desulfurization ashes," *Construction and Building Materials*, vol. 36, pp. 182–187, 2012.

[2] N. Menad, J. N. Ayala, F. Garcia-Carcedo, E. Ruiz-Ayúcar, and A. Hernández, "Study of the presence of fluorine in the recycled fractions during carbothermal treatment of EAF dust," *Waste Management*, vol. 23, no. 6, pp. 483–491, 2003.

[3] E. J. Anthony, D. L. Granatstein, and C. Science, "Sulfation phenomena in fluidized bed combustion systems," *Progress in Energy and Combustion Science*, vol. 27, no. 2, pp. 215–236, 2001.

[4] J. Zhao, D. Wang, and S. Liao, "Effect of mechanical grinding on physical and chemical characteristics of circulating fluidized bed fly ash from coal gangue power plant," *Construction and Building Materials*, vol. 101, pp. 851–860, 2015.

[5] P. Grammelis, G. Skodras, E. Kakaras et al., "Effects of biomass co-firing with coal on ash properties part 2: leaching, toxicity and radiological behaviour," *Fuel*, vol. 85, no. 16, pp. 2316–2322, 2006.

[6] Y. Xia, Y. Yan, and Z. Hu, "Utilization of circulating fluidized bed fly ash in preparing non-autoclaved aerated concrete production," *Construction and Building Materials*, vol. 47, pp. 1461–1467, 2013.

[7] S. Duan, H. Liao, Z. Ma et al., "The relevance of ultrafine fly ash properties and mechanical properties in its fly ash-cement gelation blocks via static pressure forming," *Construction and Building Materials*, vol. 186, pp. 1064–1071, 2018.

[8] Y. Shen, J. Qian, and Z. Zhang, "Investigations of anhydrite in cfbc fly ash as cement retarders," *Construction and Building Materials*, vol. 40, pp. 672–678, 2013.

[9] M. Chi and R. Huang, "Effect of circulating fluidized bed combustion ash on the properties of roller compacted concrete," *Cement and Concrete Composites*, vol. 45, pp. 148–156, 2014.

[10] J. Ding, S. Ma, S. Shen, Z. Xie, S. Zheng, and Y. Zhang, "Research and industrialization progress of recovering alumina from fly ash: a concise review," *Waste Management*, vol. 60, pp. 375–387, 2017.

[11] Z. Zhang, J. Qian, C. You, and C. Hu, "Use of circulating fluidized bed combustion fly ash and slag in autoclaved brick," *Construction and Building Materials*, vol. 35, pp. 109–116, 2012.

[12] L. Haibin and L. Zhenling, "Recycling utilization patterns of coal mining waste in China," *Resources, Conservation and Recycling*, vol. 54, no. 12, pp. 1331–1340, 2010.

[13] O. Font, P. Córdoba, C. Leiva et al., "Fate and abatement of mercury and other trace elements in a coal fluidised bed oxy combustion pilot plant," *Fuel*, vol. 95, pp. 272–281, 2012.

[14] N. Selçuk, Y. Gogebakan, and Z. Gogebakan, "Partitioning behavior of trace elements during pilot-scale fluidized bed combustion of high ash content lignite," *Journal of Hazardous Materials*, vol. 137, no. 3, pp. 1698–1703, 2006.

[15] H. Xu, Q. Li, L. Shen et al., "Synthesis of thermostable geopolymer from circulating fluidized bed combustion (CFBC) bottom ashes," *Journal of Hazardous Materials*, vol. 175, no. 1–3, pp. 198–204, 2010.

[16] H. Xu, Q. Li, L. Shen, M. Zhang, and J. Zhai, "Low-reactive circulating fluidized bed combustion (cfbc) fly ashes as source material for geopolymer synthesis," *Waste Management*, vol. 30, no. 1, pp. 57–62, 2010.

[17] G. Skodras, P. Grammelis, M. Prokopidou, E. Kakaras, and G. Sakellaropoulos, "Chemical, leaching and toxicity characteristics of cfb combustion residues," *Fuel*, vol. 88, no. 7, pp. 1201–1209, 2009.

[18] J. Yuan, "The future of coal in China," *Resources, Conservation and Recycling*, vol. 129, pp. 290–292, 2018.

[19] I. Yurtdas, N. Burlion, J.-F. Shao, and A. Li, "Evolution of the mechanical behaviour of a high performance self-compacting concrete under drying," *Cement and Concrete Composites*, vol. 33, no. 3, pp. 380–388, 2011.

[20] A. H. Akca, N. Özyurt Zihnioğlu, and B. Materials, "High performance concrete under elevated temperatures," *Construction and Building Materials*, vol. 44, pp. 317–328, 2013.

[21] D. Harbec, A. Zidol, A. Tagnit-Hamou, and F. Gitzhofer, "Mechanical and durability properties of high performance glass fume concrete and mortars," *Construction and Building Materials*, vol. 134, pp. 142–156, 2017.

[22] B. Rabehi, Y. Ghernouti, K. Boumchedda, A. Li, and A. Drir, "Durability and thermal stability of ultra high-performance fibre-reinforced concrete (UHPFRC) incorporating calcined clay," *European Journal of Environmental and Civil Engineering*, vol. 21, no. 5, pp. 594–611, 2017.

[23] R. Siddique, "Utilization of silica fume in concrete: review of hardened properties," *Resources, Conservation and Recycling*, vol. 55, no. 11, pp. 923–932, 2011.

[24] E. Vejmelková, M. Pavlíková, M. Keppert et al., "High performance concrete with Czech metakaolin: experimental analysis of strength, toughness and durability characteristics," *Construction and Building Materials*, vol. 24, no. 8, pp. 1404–1411, 2010.

[25] R. B. Ardalan, A. Joshaghani, and R. D. Hooton, "Workability retention and compressive strength of self-compacting concrete incorporating pumice powder and silica fume," *Construction and Building Materials*, vol. 134, pp. 116–122, 2017.

[26] S. E. Chidiac, D. K. Panesar, and C. Composites, "Evolution of mechanical properties of concrete containing ground granulated blast furnace slag and effects on the scaling resistance test at 28 days," *Cement and Concrete Composites*, vol. 30, no. 2, pp. 63–71, 2008.

[27] S. Teng, V. Afroughsabet, and C. P. Ostertag, "Flexural behavior and durability properties of high performance hybrid-fiber-reinforced concrete," *Construction and Building Materials*, vol. 182, pp. 504–515, 2018.

[28] S. Rajaram, "Next generation CFBC," *Chemical Engineering Science*, vol. 54, no. 22, pp. 5565–5571, 1999.

[29] M. Abed and R. Nemes, "Long-term durability of self-compacting high-performance concrete produced with waste materials," *Construction and Building Materials*, vol. 212, pp. 350–361, 2019.

[30] X. Xu, Y. Xu, and L. Duan, "Effect of fineness and components of CFBC ash on performance of basic magnesium sulfate cement," *Construction and Building Materials*, vol. 170, pp. 801–811, 2018.

[31] H.-A. Nguyen, T.-P. Chang, and J.-Y. Shih, "Effects of sulfate rich solid waste activator on engineering properties and durability of modified high volume fly ash cement based SCC," *Journal of Building Engineering*, vol. 20, pp. 123–129, 2018.

[32] G. Sheng, Q. Li, and J. Zhai, "Investigation on the hydration of CFBC fly ash," *Fuel*, vol. 98, pp. 61–66, 2012.

[33] G. Sheng, Q. Li, J. Zhai, and F. Li, "Self-cementitious properties of fly ashes from CFBC boilers co-firing coal and high-sulphur petroleum coke," *Cement and Concrete Research*, vol. 37, no. 6, pp. 871–876, 2007.

[34] W.-T. Kuo, H.-Y. Wang, and C.-Y. Shu, "Engineering properties of cementless concrete produced from GGBFS and recycled desulfurization slag," *Construction and Building Materials*, vol. 63, pp. 189–196, 2014.

[35] Z. Cheng, Z. Cheng, H. Hou, T. Han, and L. Liu, "Research on the expansion characteristics and compressive strength of mortars containing circulating fluidized bed combustion desulfurization slag," *Advances in Materials Science and Engineering*, vol. 2018, Article ID 4150145, 11 pages, 2018.

[36] S. Bhanja, B. Sengupta, and C. Research, "Modified water-cement ratio law for silica fume concretes," *Cement and Concrete Research*, vol. 33, no. 3, pp. 447–450, 2003.

[37] A. Behnood and H. Ziari, "Effects of silica fume addition and water to cement ratio on the properties of high-strength concrete after exposure to high temperatures," *Cement and Concrete Composites*, vol. 30, no. 2, pp. 106–112, 2008.

[38] R. Duval, E. H. Kadri, and C. Research, "Influence of silica fume on the workability and the compressive strength of high-performance concretes," *Cement and Concrete Research*, vol. 28, no. 4, pp. 533–547, 1998.

[39] S. K. Das, Y. J. Yudhbir, and C. Research, "A simplified model for prediction of pozzolanic characteristics of fly ash, based on chemical composition," *Cement and Concrete Research*, vol. 36, no. 10, pp. 1827–1832, 2006.

[40] R. Reis, R. Malheiro, A. Camões, and M. Ribeiro, "Carbonation resistance of high volume fly ash concrete," *Key Engineering Materials*, vol. 634, pp. 288–299, 2014.

[41] X. Fu, Q. Li, J. Zhai, G. Sheng, and F. Li, "The physical-chemical characterization of mechanically-treated CFBC fly

ash," *Cement and Concrete Composites*, vol. 30, no. 3, pp. 220–226, 2008.

[42] X.-G. Li, Q.-B. Chen, B.-G. Ma, J. Huang, S.-W. Jian, and B. Wu, "Utilization of modified CFBC desulfurization ash as an admixture in blended cements: physico-mechanical and hydration characteristics," *Fuel*, vol. 102, pp. 674–680, 2012.

[43] W. Gu, F. Xu, S. Wang, W. Li, and Y. Tan, "Effect of fly ash content on the carbonization resistance of cement paste," *IOP Conference Series: Earth and Environmental Science*, vol. 153, 2018.

[44] M. Uysal, V. Akyuncu, and B. Materials, "Durability performance of concrete incorporating class F and class C fly ashes," *Construction and Building Materials*, vol. 34, pp. 170–178, 2012.

[45] C. Karakurt and Y. Bayazıt, "Freeze-thaw resistance of normal and high strength concretes produced with fly ash and silica fume," *Advances in Materials Science and Engineering*, vol. 2015, Article ID 830984, 2015.

Research Article

Influence of Plantain Pseudostem Fibres and Lime on the Properties of Cement Mortar

Humphrey Danso

Department of Construction & Wood Technology, University of Education Winneba, P.O. Box 1277, Kumasi, Ghana

Correspondence should be addressed to Humphrey Danso; dansohumphrey@yahoo.co.uk

This study investigated the properties of cement mortar with lime reinforced with plantain pseudostem fibres. Experimental specimens with 0, 0.25, 0.5, 0.75, and 1% fibre contents by weight of sand and 10% lime content by weight of cement were prepared and tested on 7, 14, 21, and 28 days of curing for density, tensile strength, compressive strength, SEM, and EDS. The 0.25% plantain pseudostem fibre reinforced mortar achieved 23.4% compressive strength improvement over unreinforced mortar specimens. There was between 6.89 and 13.80% increase in tensile strength of the plantain pseudostem fibre reinforced mortar over the unreinforced mortar specimens. A positive linear correlation was found between the compressive strength and tensile strength of cement mortar reinforced with plantain pseudostem fibres and lime with coefficient of determinant (R^2) values between 0.909 and 0.869. It was also observed that the plantain pseudostem fibre reinforced mortar specimen had some microcracks and voids from the SEM analysis. Furthermore, EDS analysis showed the presence of calcium silicate hydrate with a Ca/Si ratio of between 1.02 and 2.49, and Al/Si ratio of between 0.76 and 0.81 as the main oxide. It therefore concluded that the incorporation of plantain pseudostem fibre and lime positively influenced the properties of the cement mortar with the 0.25% fibre content being recommended for construction application.

1. Introduction

The demand for alternative building materials that are affordable, environmentally friendly, and abundantly available is on the rise. Studies have responded to this demand with research studies being carried out to investigate the suitability of some plant residue for use in concrete and mortar [1]. More attention should be paid to the application of natural fibres as building materials for the purpose of conserving energy [2]. The application of natural fibre in mortar and concrete as admixture can contribute to the reduction of environmental challenges caused by waste disposal [3]. Today, the advancement of cement-based composites has seen innovations and techniques in designs that are economically and environmentally responsive and seek to utilize raw materials that are abundantly available. The use of plant residue by construction industry helps in achieving sustainable intake of building materials [4]. The utilization of local building materials is one of the potential ways of supporting sustainable development in emerging economies [5, 6].

An important plant residue for utilization in construction materials is pseudostem which is usually obtained from banana and plantain plants. Pseudostem is the trunk of banana or plantain plant which forms tightly wrapped overlapping sheaths. The trunk (pseudostem) contains hard fibrous overlapping layers which are spirally arranged to fold around the centre pith [1]. The pseudostem is made up of bonded filaments with cellulosic forms, hemicelluloses, and lignin [7]. The pseudostem contains woody fibre-based lignocellulose material that possesses good properties for construction application.

Studies have shown that banana pseudostem fibres can be used to reinforce the properties of cement composites. Malarvizhi et al. [8] investigated the properties of concrete slabs reinforced with banana fibres, which yielded a positive effect with significant improvement in the compressive and tensile strengths. Kumaat et al. [3] studied the characteristics

of concrete reinforced with banana stem fibre, which obtained improvement in flexural and tensile strengths of concrete. Zhu et al. [2] studied the properties of reinforced cement composites with banana fibres and found improvement in flexural and fracture toughness which are adequate for use as building material. Mostafa and Uddin [5] investigated the properties of reinforced compressed earth blocks with banana fibres and recorded improvement in the flexural and compressive strengths of the blocks. Tirkey and Ramesh [9] used banana fibres to reinforced concrete and obtained increased compressive strength. Mukhopadhyay and Bhattacharjee [10] investigated the influence of concrete reinforced with banana fibres and achieved an improved compressive strength and a low volume fraction of the concrete.

From the aforementioned, it can be seen that within the pseudostem plants, extensive research has been carried out with the use of banana fibres. There has not been enough research in the application of plantain pseudostem fibres which have similar properties to the banana pseudostem fibres in concrete and mortar. It is therefore important to advance the discourse of pseudostem fibre application in concrete and mortar by the introduction of plantain pseudostem fibres in cement-base matrix. This study, therefore, investigates the properties of cement mortar reinforced with plantain pseudostem fibres with addition of lime, to determine the influence the fibres have on the cement mortar. The study contributes to knowledge in the application of pseudostem plant fibres in sustainable construction materials. Plantain (*Musa paradisiaca*) is a common plant that grows well in sub-Sahara African, Asia, and other parts of the world. The plantain pseudostem residue is abundantly available, affordable, and possesses mechanical properties which can contribute to sustainable construction materials applicable in building construction.

2. Experimental Materials and Procedure

2.1. Experimental Materials. Sand, plantain pseudostem fibres, cement, lime, jute sack, and water are the main materials used for preparing the mortar for making specimens for the study. Pit sand that conforms to BS EN 12620 [11] requirements was used for preparing the mortar. Plantain pseudostem fibres were prepared from plantain pseudostem residue at a farm in Kumasi, Ghana. The residue was soaked in water for 24 hours, and the fibres were mechanically extracted, washed, and dried in the sun. Photographs of the sample plantain pseudostem fibres and the scanning electron microscope (SEM) image of a single fibre are shown in Figure 1. A critical observation of the SEM image of the single fibre shows continuous microstrip patterns with slight indents on the surface of the fibre. This feature of the fibre is good to ensure a good bond between the fibre and the matrix. The average diameter of the fibres measured is 0.65 ± 0.26 mm, specific weight is 0.35 g/cm^3, and water absorption of about 245%. The fibres were cut to length of aspect ratio of 100 (65 mm). Type I Portland cement of grade 32.5R produced by Ghana Cement (GHACEM) in accordance with BS-12 [12] was purchased in the market for

preparing the mortar. Locally available lime, calcium hydroxide (Ca(OH)$_2$) with 95% CaO, was also purchased in the market for preparing the mortar. Tap water was used for preparing the mortar and curing of the specimens together with jute sack.

2.2. Experimental Procedure

2.2.1. Preparation of Mortar and Specimens. Weight batching was used for measuring the materials for preparing the mortar. A mix ratio of 1 : 3 (cement: sand) was used. The quantity of lime used was 10% by weight of cement, as a replacement of cement. Plantain pseudostem fibre quantities used as reinforcement in the mortar are 0.25, 0.5, 0.75, and 1% weight of sand, as replacement of sand with 0% fibres as control. Water-cement ratios of 0.6 and 0.7 were used for the control and treatments, respectively. The control mix used less water-cement ratio (0.6) because it did not contain lime and fibre. The various mix designs and their corresponding quantities of materials used for preparing the mortars are shown in Table 1. Mechanical mixing was adopted for preparing the mortar to ensure homogenous mix. For each mix design, the materials were weighed and the plantain pseudostem fibres were immersed in water overnight. The immersion of the fibres in water was to prevent the fibres from quick absorption of water in the fresh mortar as it has very high water absorption rate. One-third quantity of water was first poured in the mixing drum and the quantity of cement was added while the drum was rotating slowly. The quantity of lime was added, followed by the fibres and then the quantity of sand added. The remaining two-third of water was added and the speed of the rotating drum increased till a uniform mixture was obtained. The mortars were used to prepare specimens (cubes and cylinders), as shown in Figure 2(a). $100 \times 100 \times 100$ mm cube specimens and cylinder specimens of length 200 mm and diameter 100 mm were moulded in accordance with BS EN 12390-2 [13]. The quantity specimens prepared was 190 (120 cubes and 70 cylinders), as shown in Table 2. After the specimens were set, they were demoulded and covered with wet jute sacks for curing (Figure 2(b)). The jute sack was kept damp throughout the curing period.

2.2.2. Testing of Specimens. The specimens were tested for density, compressive strength, and tensile strength after curing for 7, 14, 21, and 28 days. BS EN 12390-7 [14] procedure was followed to determine the dry density of the cube specimens after drying to obtain a uniform mass. Three replicates were selected, weighed, and the densities calculated for each variable and their averages used for plotting a graph, and the densities lower and upper ranges were used as the error bars on the graph. The study used BS EN 12390-3 [15] as a guide in determining the compressive strength of the cube specimens. The specimens were centrally placed in the Servo Hydraulic Universal Testing Machine and 0.05 kN/mm^2 load speed applied till the fracture of the specimens, as shown in Figure 2(c). The average of three replicate test values was recorded and used for plotting a line graph using
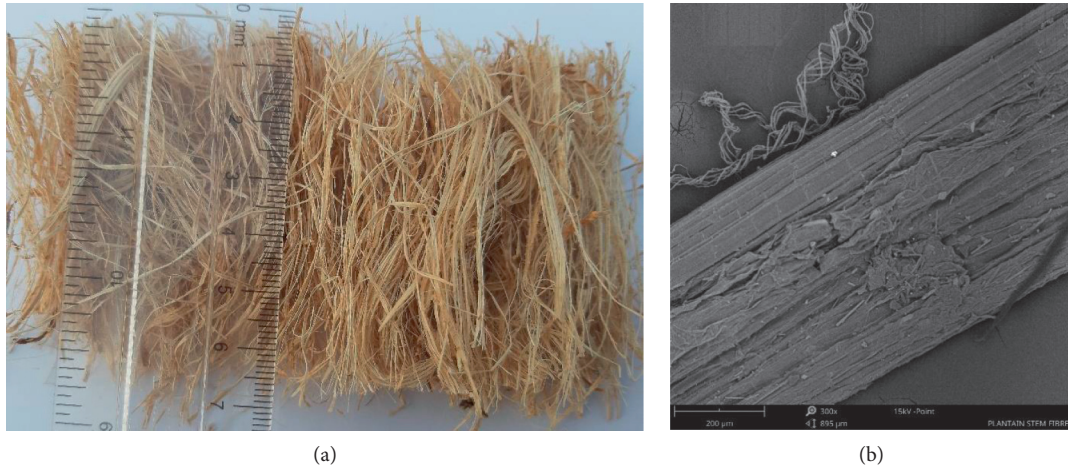
Figure 1: Photograph of plantain pseudostem fibres and SEM image (300x) of a single fibre. (a) Cut fibre photograph. (b) Single fibre SEM image.

Table 1: Mix design and quantities of materials.

Mix design	% fibre Content	Materials content (kg)				
		Sand	Fibre	Cement	Lime	Water
M-0	0.00	48.900	—	16.30	—	8.15
M-0.25	0.25	48.737	0.163	14.67	1.63	9.78
M-0.5	0.50	48.574	0.326	14.67	1.63	9.78
M-0.75	0.75	48.411	0.489	14.67	1.63	9.78
M-1	1.00	48.248	0.652	14.67	1.63	9.78

Figure 2: Preparation and testing of specimens. (a) Moulding of specimen. (b) Curing of specimen. (c) Compressive strength test setup.

Table 2: Quantity of specimens prepared.

Mix design	Types of test					Total
	Dry density	Compressive strength	Tensile strength	SEM	EDS	
M-0	12	12	12	1	1	38
M-0.25	12	12	12	1	1	38
M-0.5	12	12	12	1	1	38
M-0.75	12	12	12	1	1	38
M-1	12	12	12	1	1	38
Total	60	60	60	5	5	190
	120 cubes		70 cylinders			

SEM: scanning electron microscope; EDS: energy dispersive spectrometer.

Microsoft Office Professional Plus Excel (V 16). Stress-strain graph was also plotted out of the compressive stress and strain values obtained. BS EN 12390-6 [16] procedure was used to guide the tensile strength test conducted with cylinder specimens. The specimens were longitudinally placed in ADR 1500/2000 Testing Machine and $0.05\,kN/mm^2$ load speed applied till the fracture of the specimens. The average of three replicates' test values was recorded and used for plotting a line graph using Microsoft Office Professional Plus Excel. The correlation between the compressive strength and the tensile strength of the specimens was determined using Microsoft Office Professional Plus Excel. One-Way ANOVA tests were conducted to determine the significant differences between the control and the experimental variables using All Pairwise Multiple Comparison procedure. Microscopic and oxides composition tests were also conducted with SEM and energy dispersive spectrometer (EDS) analysis on the specimens.

3. Results

3.1. Density. The average dry densities of the 0% (control) specimens ($2167–2190\,kg/m^3$) were higher than the fibre replacement of sand by 0.25, 0.5, 0.75, and 1%, as shown in Figure 3. The 0.25 and 0.5% fibre replacement of sand recorded slightly better average densities ($2051–2063\,kg/m^3$) and ($2044–2066\,kg/m^3$), respectively. The trend of the result is consistent with the results found in some studies [2, 17, 18]. Danso et al. [19] ascribe the reduced densities in the fibre reinforced specimens to low specific weight of fibres as compare to the matrix. Therefore, as the fibre content increases, the density of the specimen is likely to reduce. Irrespective of the differences in densities, all the specimens recorded values that were more than $2000\,kg/m^3$, which are acceptable density values for cement mortar for structural works.

3.2. Compressive Strength. The compressive strength of all the mix designs increased by age from 7 days to 28 days of curing, as shown in Figure 4. This shows a normal strength development of cement and lime due to hydration caused by water mixed with the binders. The fibre replacement of sand by 0.25, 0.5, and 0.75% obtained better compressive strength of 14.33, 13.89, and 12.85 MPa, respectively, over the control specimens of 11.61 MPa on the 28-day curing, as shown in Table 3. In quantitative terms, this translates into 23.4, 19.7, and 10.7% improvement, respectively, for 0.25, 0.5, and 0.75% fibre reinforced cement mortar specimens over unreinforced mortar specimens. The result clearly indicates that the 0.25% plantain pseudostem fibre-reinforced lime cement mortar obtained an optimum compressive strength. The result is consistent with the study by Ozerkan et al. [20] which obtained similar result for mortar reinforced with palm fibres, and another study [18] which investigated the properties of mortar reinforced with hemp fibres. Çomak et al. [18] attributed the increased compressive strength to the fibres orientation and long length distribution in the cement mortar which provides better performance specimens with less microcracks. Conversely, there was reduction
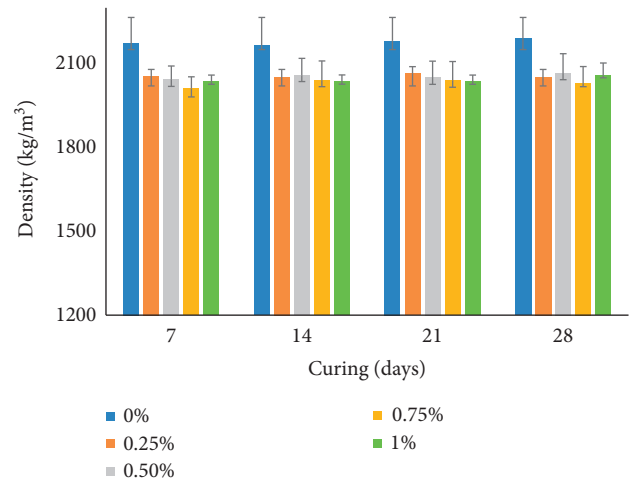
Figure 3: Dry density of the specimens.
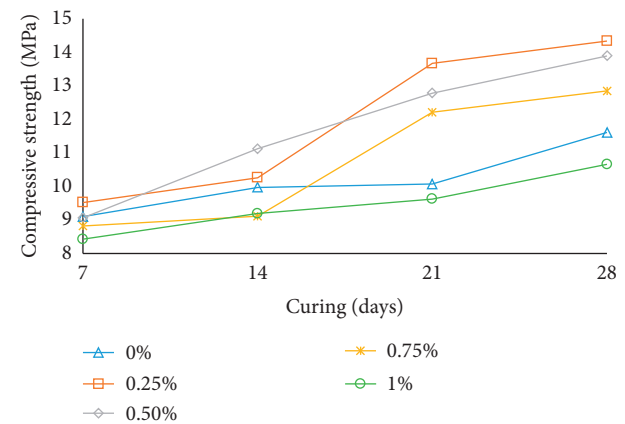
Figure 4: Compressive strength of specimens.

Table 3: Descriptive and One-Way RM ANOVA of compressive strength.

Specimen, mixture (%)	N	Mean (MPa)	Std Dev	SEM
0	3	11.610	0.356	0.206
0.25	3	14.327	0.258	0.149
0.5	3	13.893	0.260	0.150
0.75	3	12.850	0.100	0.057
1	3	10.660	0.200	0.115
Multiple comparisons versus control (Holm–Sidak method)				
Comparison	Diff of means	T	p	$p < 0.050$
0% vs. 0.25%	2.717	17.881	<0.001	Yes
0% vs. 0.5%	2.283	15.545	<0.001	Yes
0% vs. 0.75%	1.240	9.327	<0.001	Yes
0% vs. 1%	0.950	3.360	0.010	Yes

SEM: standard error of the mean; Std Dev: standard deviation.

of 8.2% compressive strength at 1% fibre inclusion in mortar as compared to the control specimens. Pederneiras et al. [21] associated the reduced compressive strength to the large

quantity of fibres in the mortar which produces voids and creates nonuniform distribution of fibres in the mortar. One-Way ANOVA test result shows a significant difference between the mix designs at $p < 0.001$, as shown in Table 3. Furthermore, the multiple comparison test results indicated that there is significant difference between the control and each of the fibre replacement content at $p \leq 0.001$. This means that the plantain pseudostem fibres (0.25 to 0.75%) and lime significantly and positively influenced the compressive strength of the cement mortar, while the plantain pseudostem fibres at 1% and lime significantly and negatively influenced the compressive strength of the cement mortar.

3.3. Compressive Strength and Strain Relationship. A parabolic curve of compressive stress and strain was obtained from the 28-day curing test of specimens, as shown in Figure 5. The highest stress was achieved from the 0.25% fibre specimens, followed by 0.5, 0.75, and 0% fibre specimens with the 1% fibre specimens recording the least stress. The result is in agreement with previous studies [5, 17, 22, 23] which obtained similar results. Inversely, the 1% plantain pseudostem fibre specimens obtained the highest strain, while the least was the control specimens. This implies that all the treatment group specimens performed better in strain than the control specimens. This is attributed to the inclusion of plantain pseudostem fibres and lime in the mortar which makes the specimens behave like an elastic material and improves the toughness of the specimens.

3.4. Tensile Strength. The tensile strength of the specimens recorded a continuous increase from curing days 7 to 28, as shown in Figure 6. This is a normal trend of any cement-based material due to hydration. The highest tensile strength (1.65 MPa) on the 28-day of testing was achieved by the 1% plantain pseudostem fibre specimens, followed by the 0.5% (1.6 MPa) and 0.25% (1.58 MPa), with the control specimens recording the least tensile strength (1.45 MPa), as shown in Table 4. There were 8.28, 10.35, 6.89, and 13.80% increases in tensile strength, respectively, for 0.25, 0.5, 0.75, and 1% plantain pseudostem fibre specimens over the control specimens. This result collaborates the findings in earlier studies [20, 23]. To ascertain if the differences between the tensile strength of the specimens were significant or not, an ANOVA test performed obtained a p value of 0.841, suggesting that there is no statistically significant difference between the tensile strengths of the mix designs. It was further observed from the tensile strength test that the split fibre reinforced specimens were held together by the fibres after failure as compared to the control specimens which were completely separated apart. This implies that the addition of fibres in mortar has the ability to bridge cracks that are likely to develop in structures. Similar observations were made in earlier studies [19, 24]. According to Danso et al. [24] the addition of fibres in matrix prevents cracks propagation as the fibres bridge across the cracks which also contributes to strength improvement. Conversely, the unreinforced specimens separated into two parts after the
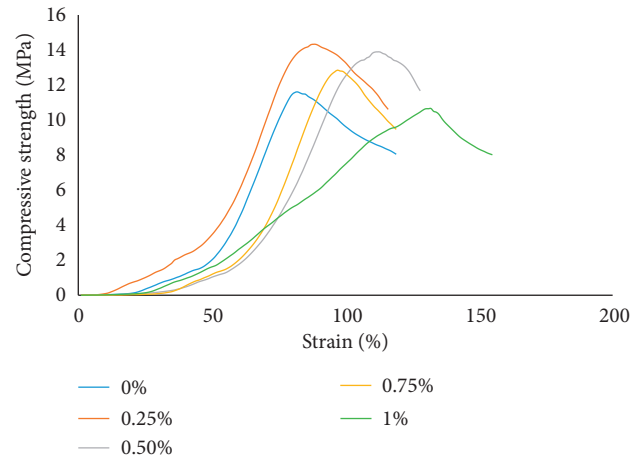

FIGURE 5: Compressive stress and strain relationship.
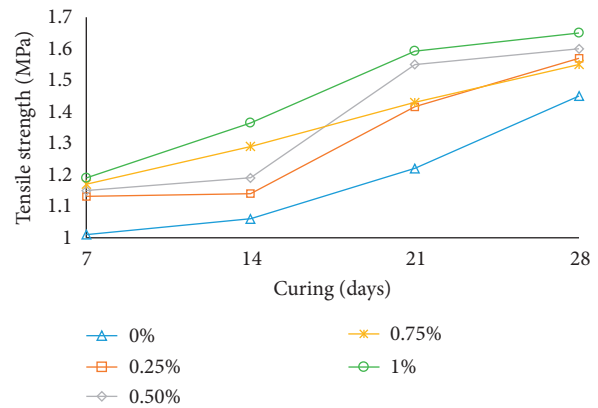
FIGURE 6: Tensile strength of specimens.

TABLE 4: Descriptive and One-Way RM ANOVA of tensile strength.

Specimen, mixture (%)	N	Mean	Std Dev	SEM
0	3	1.450	0.304	0.176
0.25	3	1.579	0.154	0.088
0.5	3	1.600	0.200	0.115
0.75	3	1.550	0.180	0.104
1	3	1.650	0.180	0.104
Source of variation	DF	SS	F	p
B/t subjects	2	0.0455		
B/t treatments	4	0.0684	0.345	0.841
Residual	8	0.397		
Total	14	0.511		

SEM: standard error of the mean; Std Dev: standard deviation.

tensile strength test. The unreinforced specimens were also found to have lower tensile strength as was also in the case of compressive strength as compared with the fibre reinforced specimens, which can be attributed to inadequate elastic behavior, low toughness, and lack of friction between the constituent materials of the unreinforced specimens.
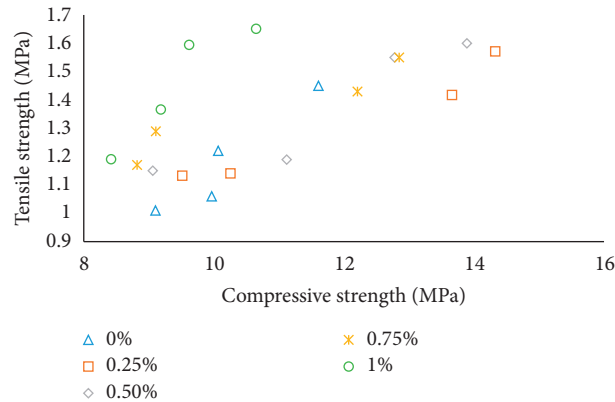
Figure 7: Relationship between compressive strength and tensile strength.

3.5. Relationship between Compressive Strength and Tensile Strength. A positive linear correlation was obtained between the compressive strength and tensile strength of cement mortar reinforced with plantain pseudostem fibres and lime, as shown in Figure 7. The highest coefficient of determinant (R^2) was 0.956 for 0.25% plantain pseudostem fibre specimens, implying a corresponding increase in both tensile and compressive strengths of the specimens. This was followed by 0.909, 0.906, 0.874, and 0.869 R^2 values, respectively, for 0.75, 0, 1, and 0.5% plantain pseudostem fibre specimens. This result collaborates the findings of previous studies [17] on mortars reinforced with different natural fibres. This means the compressive strength is a good predictor of tensile strength of plantain pseudostem fibres and lime in cement mortar. The factors given by the compressive and tensile strengths of the specimens are 8.00, 9.07, 8.68, 8.29, and 6.46 for 0, 0.25, 0.5, 0.75, and 1%, respectively, for plantain pseudostem fibre specimens. These factors are within the factors obtained by an earlier study [19] which recorded the factors between 6.6 and 14.9, while it was about double (2.46 to 3.58) of the factors obtained from another study [24] on soil-based matrix reinforced with natural fibres.

3.6. Microstructural and Oxide Composition Examination. Scanning electron microscope (SEM) analysis was conducted to examine the microstructural properties of the specimens. The images obtained are shown in Figure 8. The control (unreinforced mortar) specimen image (Figure 8(a)) shows the cement mortar with virtually no observed cracks. Conversely, the plantain pseudostem fibre reinforced lime mortar specimen (Figure 8(b)) shows some microcracks and voids. Development of voids in the cement matrix is not unusual as the material has the propensity of absorbing moisture. The microcracks usually occur due to manufacturing or handling deficiencies. The cracks are such that they cannot be seen by the naked eyes. The plantain pseudostem fibres are also clearly seen in the lime cement mortar, as shown in Figure 8(b). Studies have observed that the presence of random fibres in matrix generates bond, increases toughness, and reduces shrinkage in composite materials [25–27]. It is due to this that the incorporation of the plantain pseudostem fibre in the mortar resulted in the

improved compressive and tensile strengths of the specimens. However, studies have also identified that increased quantity of fibres in the matrix causes the fibres to knock and overlap each other leading to lost cohesion with the matrix, and eventually weakening the composite material [19, 24]. These factors contributed to the declined strength of the plantain pseudostem fibre specimens.

Energy dispersive spectrometer (EDS) analysis was also conducted to examine the oxides composition in the plantain pseudostem fibre-lime-cement mortar specimens, as shown in Figure 9. The EDS analysis was conducted on a spot where there was a mix of the lime cement mortar deposited on the plantain pseudostem fibre, as shown in Figure 9(a), and another spot on the lime cement mortar without the fibre, as illustrated in Figure 9(c). These spots were selected because they provided the opportunity to identify the chemical composition present in the combined fibre-lime-cement mortar (FLCM) and lime-cement mortar (LCM) for comparison. The elements shown in the result are oxygen (48.09% FLCM and 52.39% LCM), carbon (22.03% FLCM and 21.92% LCM), calcium (8.54% FLCM and 9.84% LCM), silicon (8.40% FLCM and 8.81% LCM), aluminium (6.80% FLCM and 6.68% LCM), nitrogen (4.83% FLCM and 0.00% LCM), potassium (0.88% FLCM and 0.37% LCM), and sodium (0.42% FLCM and 0.00% LCM) in weight concentration, as shown in Figures 9(b) and 9(d). It can be observed that the weight concentration of the elements such as oxygen, calcium, silicon, and aluminium were higher in the LCM than the FLCM. It can further be observed that the LCM specimens contain no amount of nitrogen and sodium.

The oxides identified in the FLCM and the LCM specimens are carbon (C), calcium (Ca), silicon (Si), aluminium (Al), nitrogen (N), potassium (K), and sodium (Na), respectively, with their stoichiometric weight concentration of (42.44% FLCM and 20.67% LCM), (16.45% and 46.03% LCM), (16.19% and 18.50% LCM), (13.10% and 14.02% LCM), (9.31% and 0.00% LCM), (1.70% and 0.78% LCM), and (0.82% and 0.00% LCM). It can again be observed that the LCM specimens contain no amount of nitrogen and sodium. The analysis indicates the presence of calcium silicate hydrate with a Ca/Si ratio of 1.02 and 2.49, respectively, for FLCM and LCM, which is within the maximum limit of
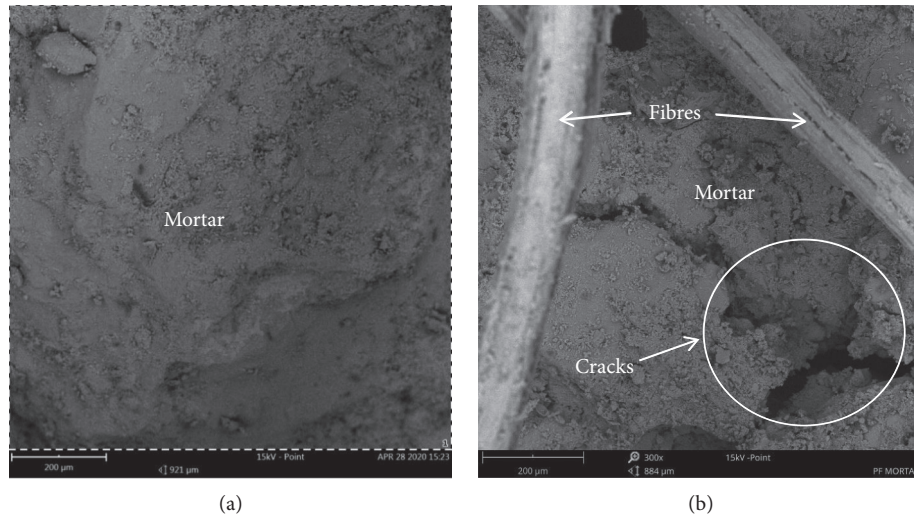
FIGURE 8: SEM images (300x) of unreinforced mortar and plantain pseudostem fibre reinforced mortar. (a) Image of unreinforced mortar. (b) Image of fibre reinforced mortar.

	Element		Oxide	
Symbol	Atomic conc. (%)	Wt. conc. (%)	Symbol	Stoichiometric wt. conc. (%)
O	50.17	48.09		
C	30.62	22.03	C	42.44
Ca	3.56	8.54	Ca	16.45
Si	4.99	8.40	Si	16.19
Al	4.21	6.80	Al	13.10
N	5.76	4.83	N	9.31
K	0.38	0.88	K	1.70
Na	0.31	0.42	Na	0.82

	Element		Oxide	
Symbol	Atomic conc. (%)	Wt. conc. (%)	Symbol	Stoichiometric wt. conc. (%)
O	62.83	52.39		
Ca	10.49	21.92	Ca	46.03
C	15.72	9.84	C	20.67
Si	6.02	8.81	Si	18.50
Al	4.75	6.68	Al	14.02
K	0.18	0.37	K	0.78
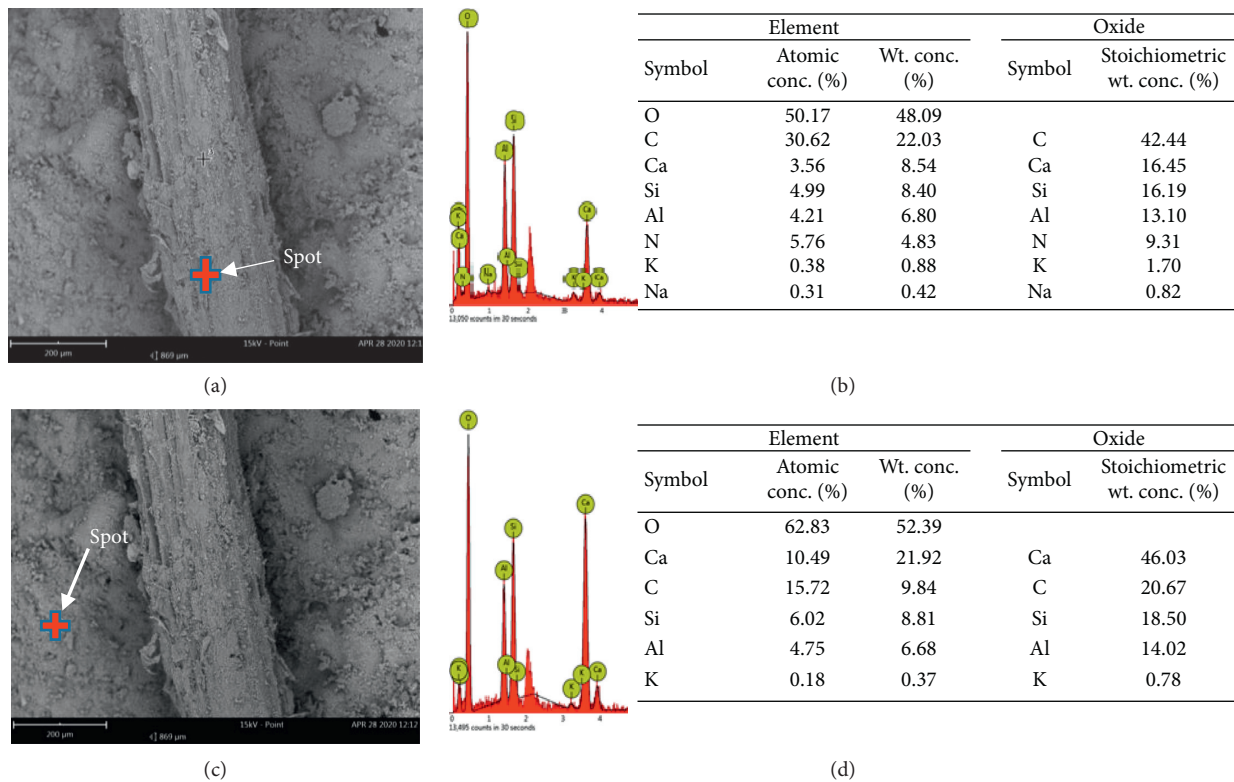
FIGURE 9: EDS analysis on specimen. (a) Selected spot image on fibre. (b) Chemical composition of matrix expressed as percentage of the elements and oxides for spot on fibre. (c) Selected spot image on mortar. (d) Chemical composition of matrix expressed as percentage of the elements and oxides for spot on mortar.

2.50 for mortar samples made with Portland cement as indicated by Kunther et al. [28]. The Al/Si ratio of 0.81 and 0.76, respectively, for FCLM and CLM, and Ca/Si ratio of 1.02 and 2.49, respectively, for FCLM and CLM as obtained in the specimen have impact on the mechanical properties of the material [29, 30]. The high presence of elements such as C, Ca, Si, and Al and their compositions helps in improving the bond characteristics of the mortar.

4. Summary and Conclusion

The study investigated the properties of cement mortar reinforced with plantain pseudostem fibres and lime. It was revealed that

(1) Plantain pseudostem fibre-reinforced lime cement mortar obtained dry density values more than $2000 \, \text{kg/m}^3$ which are acceptable for cement mortar for structural works

(2) 0.25% plantain pseudostem fibre-reinforced lime cement mortar recorded 23.4% compressive strength improvement over unreinforced mortar specimens with significant difference ($p < 0.001$)

(3) There was between 6.89 and 13.80% increase in tensile strength of the plantain pseudostem fibre-reinforced lime cement mortar over the unreinforced cement mortar specimens with no significant difference ($p = 0.841$)

(4) There was a positive linear correlation between the compressive strength and tensile strength of cement mortar reinforced with plantain pseudostem fibres and lime with coefficient of determinant (R^2) values between 0.909 and 0.869

(5) Plantain pseudostem fibre reinforced lime mortar specimen showed some microcracks and voids from the SEM analysis

(6) The EDS analysis showed the presence of calcium silicate hydrate with a Ca/Si ratio of between 1.02 and 2.49, and Al/Si ratio of between 0.76 and 0.81 as the main oxide composition

The study, therefore, concludes that the incorporation of plantain pseudostem fibre and lime positively influenced the properties (such as compressive and tensile strengths) of the cement mortar with the 0.25% fibre content being recommended for construction application.

Data Availability

The data used to support the findings of this study are available from the corresponding author upon request.

Conflicts of Interest

The authors declare that they have no conflicts of interest.

References

[1] A. A. Umoh and S. P. A Nnana, "Study of *Musa Paradisiaca* pseudo-stem pith fluid as set-retarding admixture in cement paste and mortar," *Emirates Journal for Engineering Research*, vol. 19, no. 3, pp. 11–18, 2014.

[2] W. H. Zhu, B. C. Tobias, R. S. P. Coutts, and G. Langfors, "Air-cured banana-fibre-reinforce cement composite," *Cement & Concrete Composite*, vol. 16, pp. 1–6, 1994.

[3] E. J. Kumaat, M. R. I. A. J. Mondoringin, and H. Manalip, "Basic behaviour of natural banana stem fiber reinforced concrete under uniaxial and biaxial tensile stress," *International Journal of GEOMATE*, vol. 14, no. 44, pp. 166–175, 2018.

[4] F. Pacheco-Torgal and S. Jalali, "Cementitious building materials reinforced with vegetable fibres: a review," *Construction and Building Materials*, vol. 25, no. 2, pp. 575–581, 2010.

[5] M. Mostafa and N. Uddin, "Effect of banana fibers on the compressive and flexural strength of compressed earth blocks," *Buildings*, vol. 5, no. 1, pp. 282–296, 2015.

[6] H. Danso, "Identification of key indicators for sustainable construction materials," *Advances in Materials Science and Engineering*, vol. 2018, pp. 1–7, 2018.

[7] U. D. Akpabio, D. S. Udiong, and A. E. Akpakpan, "The physicochemical characteristics of plantain (*Musa Paradisiaca*) and banana (*Musa Sapientum*) pseudo-stem wastes," *Advances in Natural and Applied Sciences*, vol. 6, no. 2, pp. 167–172, 2012.

[8] V. Malarvizhi, V. Mahisha Vardhini, R. Aksayaa, S. Abinaya, and U. Arthi, "Experimental investigation of low cost slab using banana stem fibre," *International Research Journal of Engineering and Technology*, vol. 6, no. 3, pp. 286–289, 2019.

[9] N. Tirkey and G. B. Ramesh, "Experimental study on the banana fiber reinforced concrete," *International Journal of Pure and Applied Mathematics*, vol. 119, no. 18, pp. 2053–2056, 2018.

[10] S. Mukhopadhyay and B. Bhattacharjee, "Influence of fibre dispersion on compression strength of banana fibres reinforced concrete," *Journal of Industrial Textiles*, vol. 45, no. 5, pp. 957–964, 2016.

[11] BS EN 12620:2002+A1:2008, *Aggregates for Concrete*, British Standards Institution, London, UK, 2002.

[12] BS-12: 1996, *Specification for Portland Cement*, British Standards Institution, London, UK, 1996.

[13] BS EN 12390-2: 2009, *Testing Hardened Concrete. Making and Curing Specimens for Strength Tests*, British Standards Institution, London, UK, 2019.

[14] BS EN 12390-7:2009, *Testing Hardened Concrete-Density of Hardened Concrete*, British Standards Institution, London, UK, 2019.

[15] BS EN 12390-3:2009, *Testing Hardened Concrete-Compressive Strength of Test Specimens*, British Standards Institution, London, UK, 2019.

[16] BS EN 12390-6:2009, *Testing Hardened Concrete-Tensile Splitting Strength of Test Specimens*, British Standards Institution, London, UK, 2010.

[17] H. Danso and D. Manu, "Influence of coconut fibres and lime on the properties of soil-cement mortar," *Case Studies in Construction Materials*, vol. 12, pp. 1–12, 2020.

[18] B. Çomak, A. Bideci, and Ö. Salli Bideci, "Effects of hemp fibers on characteristics of cement based mortar," *Construction and Building Materials*, vol. 169, pp. 794–799, 2018.

[19] H. Danso, D. B. Martinson, M. Ali, and J. B. Williams, "Physical, mechanical and durability properties of soil building blocks reinforced with natural fibres," *Construction and Building Materials*, vol. 101, pp. 797–809, 2015.

[20] N. G. Ozerkan, B. Ahsan, S. Mansour, and S. R. Iyengar, "Mechanical performance and durability of treated palm fiber reinforced mortars," *International Journal of Sustainable Built Environment*, vol. 2, no. 2, pp. 131–142, 2013.

[21] C. M. Pederneiras, M. do Rosário Veiga, and J. de Brito, "Effects of the incorporation of waste fibres on the cracking resistance of mortars: a review," *International Journal of Green Technology*, vol. 4, pp. 38–46, 2018.

[22] M. O. Bouffoue, C. H. Kouakou, K. C. Kouadio, A. A. Assande, S. Ouattara, and E. Emeruwa, "Experimental

method to measure the mechanic behavior of compressed earth blocks in continuous compression," *Journal of Asian Scientific Research*, vol. 5, no. 1, pp. 31–37, 2015.

[23] K. N. Indira, J. Parameswaranpillai, and S. Thomas, "Mechanical properties and failure topography of banana fiber PF macrocomposites fabricated by RTM and CM techniques," *ISRN Polymer Science*, vol. 2013, Article ID 936048, 8 pages, 2013.

[24] H. Danso, D. B. Martinson, M. Ali, and J. Williams, "Effect of fibre aspect ratio on mechanical properties of soil building blocks," *Construction and Building Materials*, vol. 83, pp. 314–319, 2015.

[25] M. Maalej, V. C. Li, and T. Hashida, "Effect of fiber rupture on tensile properties of short fiber composites," *Journal of Engineering Mechanics*, vol. 121, no. 8, pp. 903–913, 1995.

[26] A. Slosarczyk, "The influence of nonetallic and metallicfibres on the mechanical properties of cement mortars," *in International Symposium on Brittle Matrix Composite 10,* J. Olek, A. M. Brandt, M. A. Glinicki et al., Eds., Woodhead Publishing, Warsaw, Poland, 2012.

[27] H. Danso, D. B. Martinson, M. Ali, and J. B. Williams, "Mechanisms by which the inclusion of natural fibres enhance the properties of soil blocks for construction," *Journal of Composite Materials*, vol. 51, no. 27, pp. 3835–3845, 2017.

[28] W. Kunther, B. Lothenbach, and J. Skibsted, "Influence of the Ca/Si ratio of the C-S-H phase on the interaction with sulfate ions and its impact on the ettringite crystallization pressure," *Cement and Concrete Research*, vol. 69, pp. 37–49, 2015.

[29] C. A. Botero, E. Jimenez-Piqué, R. Martín, T. Kulkarni, V. K. Sarin, and L. Llanes, "Nanoindentation and nanoscratch properties of mullite-based environmental barrier coatings: influence of chemical composition - Al/Si ratio," *Surface and Coatings Technology*, vol. 239, pp. 49–57, 2014.

[30] H. Danso, "Effect of rice husk on the mechanical properties of cement-based mortar," *Journal of The Institution of Engineers (India): Series D*, 2020.

Research Article

Investigation on Calcined Magnesium-Based Mineral Powder and Its Behavior as Alternative Binder

G. Sugila Devi [1] and K. Sudalaimani [2]

[1]*Department of Civil Engineering, Nadar Saraswathi College of Engineering and Technology, Theni 625531, Tamil Nadu, India*
[2]*Department of Civil Engineering, Thiagarajar College of Engineering, Madurai 625015, Tamil Nadu, India*

Correspondence should be addressed to K. Sudalaimani; ksudalaimani.civil@gmail.com

This paper investigates the behavior of calcined powder made of natural magnesite and natural steatite. The magnesite and steatite are made into a powder of ratio 3 : 1 by weight proportion, and the combination is thermally decomposed at a temperature of 1200° Celsius. The calcined powder along with and without Sodium Tripolyphosphate (STPP) salt is tested for its microscopic structural development, consistency, initial setting time, final setting time, and heat of hydration. The powder is made into paste with water/powder ratio as 0.25 and the hardened samples are tested for its compressive strength, drying shrinkage, pH value, SEM analysis, and XRD analysis. The results show that adding phosphate salt increases the hydration process, setting time, and strength aspects. The test samples are found with hydration products such as magnesium hydroxide and struvite. Thus, the present work shows that natural metamorphic magnesite and natural metamorphic steatite can be the potential alternative resource for the production of magnesium-based binder.

1. Introduction

There is an increasing concern over environmental impact of existing binders, such as ordinary portland cement. There are a lot of studies made to find the effective alternative binders. Alternative binders are a type of manmade mineral material which can react with water and/or CO_2 and get hardened and can be later used to concrete or mortar as binder. The magnesium-based binders are considered to be the carbon negative as the water usage is reduced in comparison to Portland cement and the energy spent on preparing the magnesium-based cement will be lesser than calcium-based cement. This is due to lesser calcination temperature of magnesium-based cement with 650°C to 1200°C [1], when compared to calcium-based cement which has reacting temperature above 1300°C [2]. The magnesium from reject desalination brine is studied and found that it can react with CO_2 in atmosphere at 25°C to 65°C which is a breakthrough in carbon capture and utilization [3]. With this observation,

it is understood that even with little higher emission of carbon dioxide during calcination, this reactive magnesium can capture the CO_2 in atmosphere, ensuring eco-friendliness. The raw materials are varied in production of cement to reduce the stress on single raw material which can cause stress to the resource and resource depletion. Magnesium-based minerals are good alternative to calcium-based minerals which influence the strength development, microstructure, and pH of binders [4, 5]. The magnesium oxychloride cement has higher strength due to the formation of magnesium hydroxide [6], and the mechanical behavior of magnesium oxysulfate cement is based on the relative contribution of porosity, pore size, and higher interparticle bonds [7]. The magnesium phosphate cement (MPC) has rapid setting, light weight properties, and also higher strength gain, and the MPC has a potential future of replacing the conventional cement [8]. The early studies show that the calcined magnesite has hydration reaction and this calcined magnesite can even replace 50% of ordinary portland cement [9]. The

formation of the hydrate phase in the MgO-based cement is attributed to the hydromagnesite which also influences the formation of brucite [10]. Cement manufacturing is one of the major sources of greenhouse gas emissions. Global warming is one of the concerning problems, where finding a solution is imminent [11]. Steatite also known as soapstone is a schist which is rich in magnesium [12]. It is used in applications such as ceramics manufacturing [13] and preparation of panels for switchboards [14]. Limited works are only found on its application in cement industry.

Lot of research works were carried out previously to replace cement in concrete production by industry waste materials such as fly ash and rice husk ash. However, researchers were unable to find a way to completely replace cement in conventional concrete [15].

Magnesium has the property of reducing pH of mixture in which it is mixed [5]. It is also observed that addition of magnesium leads to early strength gain in concrete [16], and this could lead to utilizing steatite in concrete which will protect from adverse climatic conditions.

Steatite in its raw form is unable to deliver sufficient strength, so processing of raw material is obligatory. Furthermore, it is fine grinded for better results. A new kind of binder material, i.e., Magnesium Silicate Hydrate (MSH) gel is found when cement is partially replaced by steatite [17]. MSH gel is found to be much denser than CSH gel. However, synergy is not observed when steatite was used along with cement. One of the reasons could be its incompatibility in shapes, i.e., globules shape of MSH gel and sheet structure of CSH gel [4]. Researchers found that replacement up to 15% to the weight of cement in concrete was beneficial in strength gain [14].

In the previous works, researchers tried to use steatite as a raw feed for alkali-activated type binder [18]. As the process of alkali activation is a bit costly compared to conventional cement concrete, this research tries to find an economical as well as sustainable alternative.

Very limited works are carried out to assess the performance of calcined magnesite and steatite as binding material in the construction sector. This work proposes a novel binding substance, magnesium carbonate- and magnesium silicate-based calcined material with and without sodium tripolyphosphate (STPP) salt, which could replace the conventional mechanism in concrete. Furthermore, present work tries to achieve serviceable strength of binder by using magnesite- and steatite-based binder.

2. Materials and Testing Procedures

2.1. Materials Used in This Study. Naturally available metamorphic magnesium carbonate (magnesite) and naturally available metamorphic magnesium silicate are obtained and grinded to powder in ultrafine grinding ball mills. The properties of magnesite and steatite are given in Table 1. The ratio of magnesite to steatite is maintained as 3 : 1 by weight of powder. The mixed powder of magnesite and steatite is placed in crucible and kept in muffle furnace for a temperature of 1200°Celcius for a period of 3 hours. The temperature is fixed as the calcination process in magnesite starts above 850°C, and at 1500°C, it becomes dead burnt and agglomerated [19]; hence, the temperature is fixed at 1200°C. Then, the powder is again grinded using ultradine ball mill. This sample is named as MB. A part of MB is then added with 5% of sodium tripolyphosphate and this sample is named as MPB. The properties of calcined magnesite and steatite (MB) are given in Table 2. The samples used for strength and pH measurement have hardened for 28 days in ambient condition.

2.2. Sample Preparation and Testing Methodology. The consistency of powder and its Initial Setting Time (IST) and Final Setting Time (FST) are tested with Vicat's apparatus confirming to IS:4031-1988. The MB and MPB are made into paste with water. The water consistency is measured through Vicat's apparatus with a plunger where the trial pastes with water from 10% to 20% are prepared with different water percentages, and the sample which has Vicat's reading of 5 mm to 7 mm is taken as an appropriate sample through which the water requirement for the respective binder is identified. For preparation of hardened paste, the ratio of water to powder is taken as 0.25 and casted as cylinders with dimension of 10 mm diameter and 20 mm height. The samples are ambient cured in normal atmospheric temperature until testing days. The compressive strength is measured using Shimadzu compressive testing machine with the maximum capacity of 2000 kN. The shrinkage is measured using digital Vernier caliper on the standard samples, and the samples are unchanged and kept undisturbed for the testing period. The pH is measured by crushing the sample to powder and mixing it with 10 parts of neutral water for a period of 24 hours in flocculation set up, then the water is filtered, and pH is measured with pH meter. The heat of hydration is measured with digital thermal sensors with accuracy of −50° Celsius to +50° Celsius, and the sensor is immersed in the paste immediately after its preparation in the mold. The digital probe microscope scope is used to capture image of the paste in fresh state up to 500x magnification and the scanning electron microscope is used to capture and analyze the hardened samples up to 5000x magnification. The XRD analysis is carried out with a Siemens D-5000 X-ray diffractometer with Cu K-beta radiation and 2 scanning with a step size of 0.02° and a measuring time of 10.00 Deg/minute. A voltage of 40 kV and current of 15 mA are used. Samples are collected from the cubes after 28 days of water curing and powdered in ball mills to pass through the sieve size of 90 μ.

3. Results and Discussion

The MB and MPB samples are tested for its various behavior and performances through standard procedures.

Table 1: Magnesite and steatite properties.

	Magnesite	Steatite
Physical properties		
Specific gravity	3.2	2.7
Loss of ignition (%)	45.99	3.33
Chemical properties		
SiO_2 (%)	8.97	62.67
Al_2O_3 (%)	0.30	0.24
MgO (%)	43.54	33.26
Fe_2O_3 (%)	0.64	0.30
CaO (%)	0.56	0.20

Table 2: Properties of calcined powder (magnesite and steatite).

Properties	Values
Blaine surface area (m^2/kg)	600
Particle mean dia (μm)	<15
Specific gravity	3.3

To perform as a binder study on consistency, setting time and compressive strength are the important parameters. Table 3 shows the results of water consistency, setting time, and compressive strength of the samples. The results show that the requirement of water to initiate the paste phase of the MB powder is 15% and MPB powder is 16% by weight of powder. It is observed that the requirement of water is reduced by 40% to 50% compared to Ordinary Portland Cement. It is clear that the water usage can be reduced in this type of binding materials. The magnesium-based calcined powder with soluble phosphates increases the water resistance due to its lower concentration of Mg^{2+} ions possible [20]. The STPP has also brought early hydration and this tends to increase the water requirement by 1% than the MB sample. Even though the particle size is smaller in both powders, it does not affect the water consistency. Consequently, it reduces the burden of water usage compared to Ordinary Portland Cement. The results on setting time show that the MB sample sets faster than the MPB sample. The IST and FST of MB are 28% and 25%, respectively, which are comparatively lesser than MPB samples. It can be understood that setting process of MB is faster when compared to MPB. The setting time is faster in the MB sample due to insufficient H+ ions and this is altered in the MPB samples due to presence of soluble phosphates [21]. Table 3 and Figure 1 show the result on compressive strength of MB and MPB samples. The compressive strength results show that MPB performs well than the MB samples. The MPB has 50%, 38%, 39%, and 42% higher strength gain on 3 days, 7 days, 14 days, and 28 days, respectively, in comparison with MB samples. The strength gain is attributed to the presence of phosphate in the MPB samples due to condensed microstructure in the MPB samples [22]. The drying shrinkage represented in Figure 2 shows that on initial days there are no shrinkage and as the days increase the shrinkage also increases for both MB and MPB samples. The MPB has 2.3%, 9.9%, 5.8%, 6.1%, 5.4%, and 3.9% lesser

shrinkage on 7 days, 14 days, 28 days, 42 days, 56 days, and 70 days, respectively, in comparison to MB samples. The shrinkage is lesser in comparison to the conventional OPC samples and behaves similar to that of earlier studies [23]. The strength development is due to the formation of magnesium hydroxide in MPB samples [24]. The pH value shown in Table 3 represents the hydrogen concentration, and this shows that the MB has a pH of 12.80 and MPB has 13.80, which is more alkaline than the standard OPC binder-based paste with a pH value between 11 and 13.

The heat of hydration curve represented in Figure 3 shows that MPB starts with higher heat in comparison with MB and then slowly decreases and gets normalized within 1-hour duration. There still has heat development even in 3 days, but it is observed that heat normalizes and the heat generation is constant even after 72 hours. This shows that there is sudden heat generation due to the setting of paste of MB and MPB samples due to the presence of reactive magnesia which also reflects in the setting time [25], and the heat produced is constant from day 0 to even after day 3, which is notable.

Figure 4 shows the microscopic image of MB and MPB on 0 hours to 48 hours. From the microscopic image, it can be identified that MB, from 0 hour to 1 hour, has much structural change, and after which no much change is observed. However, when compared to the 12 hours image both 24-hour and 48-hour images have a little broadened crack, apart from this no notable changes are observed. In MPB images, from 0-hour to 1-hour image, the structural difference is not as large as MB.

Figure 5 shows the scanning electron microscopic images, from which it can be seen that MPB samples have more amorphous products in comparison to MB sample, and the MPB sample is closely packed and there are very less microstructural pores. The MB sample shows the hydration product $Mg(OH)_2$ in a needle-/floral-shaped structure. The calcination process induces reactive magnesium oxides. When the same reacts with water, the magnesium hydroxide products are formed. In addition, a small amount of $Mg(OH)_2$ is inhibited through stabilization of 5 $Mg(OH)_2$ $MgCl_2$ $8H_2O$ (HP) [26]. The MPB sample witnesses the presence of struvite in the irregular shape structure [27]. These struvite crystals are the important hydration products in magnesium phosphate cement [28] and the same is achieved here, which contributes to the strength of MPB samples [27, 28]. The HP is formed in very small intensity as observed in Figure 6, and this is due to the presence of chloride impurities in magnesite and steatite before calcination. Furthermore, the MPB sample has traces of struvite crystal (SC) [29]. Both HP and SC in MB and MPB samples act as hydration products which influence the hydration, setting time, and strength of the powder matrix.

Figure 6 shows the XRD analysis of MB and MPB. The MB samples show the presence of HP which is already confirmed through Figure 5. The presence of quartz is also identified due to the reaction of silicate in steatite. Next, the presence of Mg $(OH)_2$ is evident in both MB and

TABLE 3: Test results on consistency, setting time, and strength development.

Sample ID	Water consistency in percentage	Setting time in minutes		Compressive strength in MPa				pH value
		Initial	Final	3 days	7 days	14 days	28 days	
MB	15.00	25.00	300.00	10.00	13.00	14.00	14.20	12.80
MPB	16.00	35.00	400.00	15.00	18.00	19.50	20.20	13.80
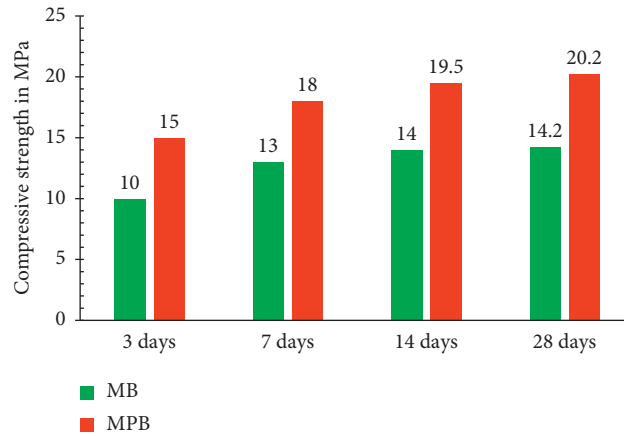
FIGURE 1: Compressive strength of MB and MPB samples.
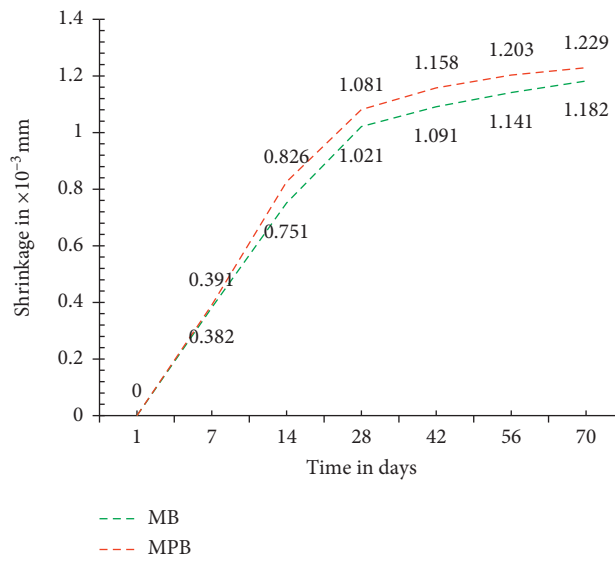
FIGURE 2: Drying shrinkage of MB and MPB samples.

MPB samples. The hydration is linked to HP in MB sample and struvite in the MPB sample. Both have considerable intensity of brucite, and it is observed that there is stable HP available which resists to form into Mg (OH)$_2$. Furthermore, it suggests the improved stability of HP against water requirement. The softening strength results in comparison to MPB samples are attributed to above discussed process [26]. The incorporation of STPP has brought increase in compressive strength and decrease in pore volumes as observed in the SEM images.

The MPB specimens show dense microstructure and struvite crystals fill the pores. These morphologies are due to the influence of STPP [30]. The struvite in presence of water is in more stable phase as studied in the earlier studies [31]. And also this availability of struvite has influence on compressive strength due to dissolutions [25]. Thus, the calcined magnesite and steatite have the properties which are similar to that of binders and few properties are similar to that of Ordinary Portland cement.
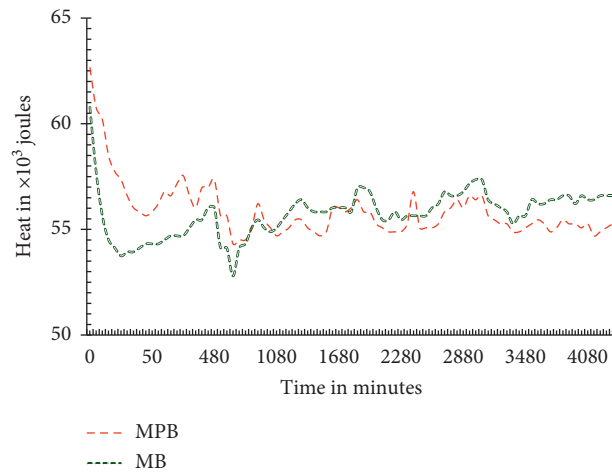
FIGURE 3: Heat measurement.
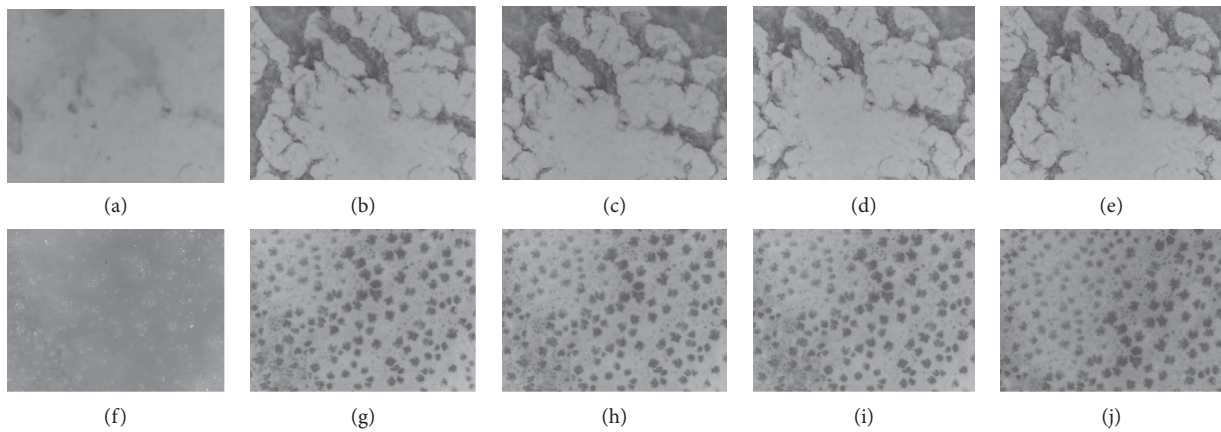
FIGURE 4: Microscopic images of MB and MPB. (a) MB: 0 hour. (b) MB: 1 hour. (c) MB: 12 hours. (d) MB:24 hours. (e) MB: 48 hours. (f) MPB: 0 hour. (g) MPB: 1 hour. (h) MPB: 12 hours. (i) MPB: 24 hours. (j) MPB: 48 hours.
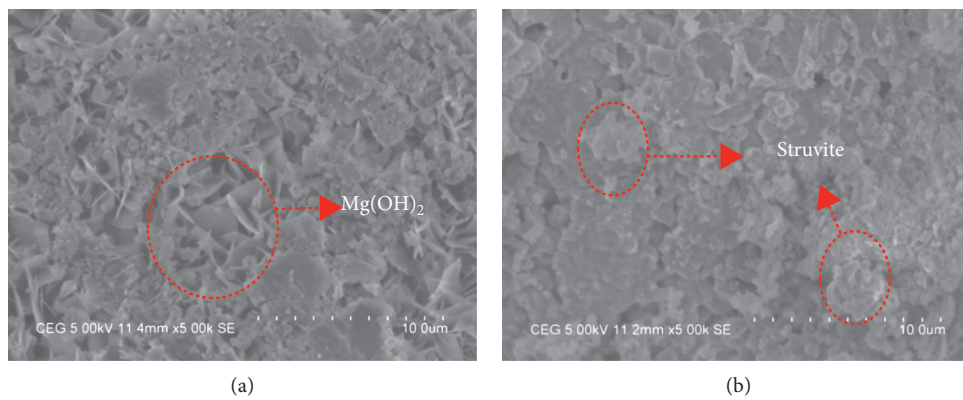
FIGURE 5: Scanning electron microscopic image of: (a) MB sample and (b) MPB sample.

(a)

(b)
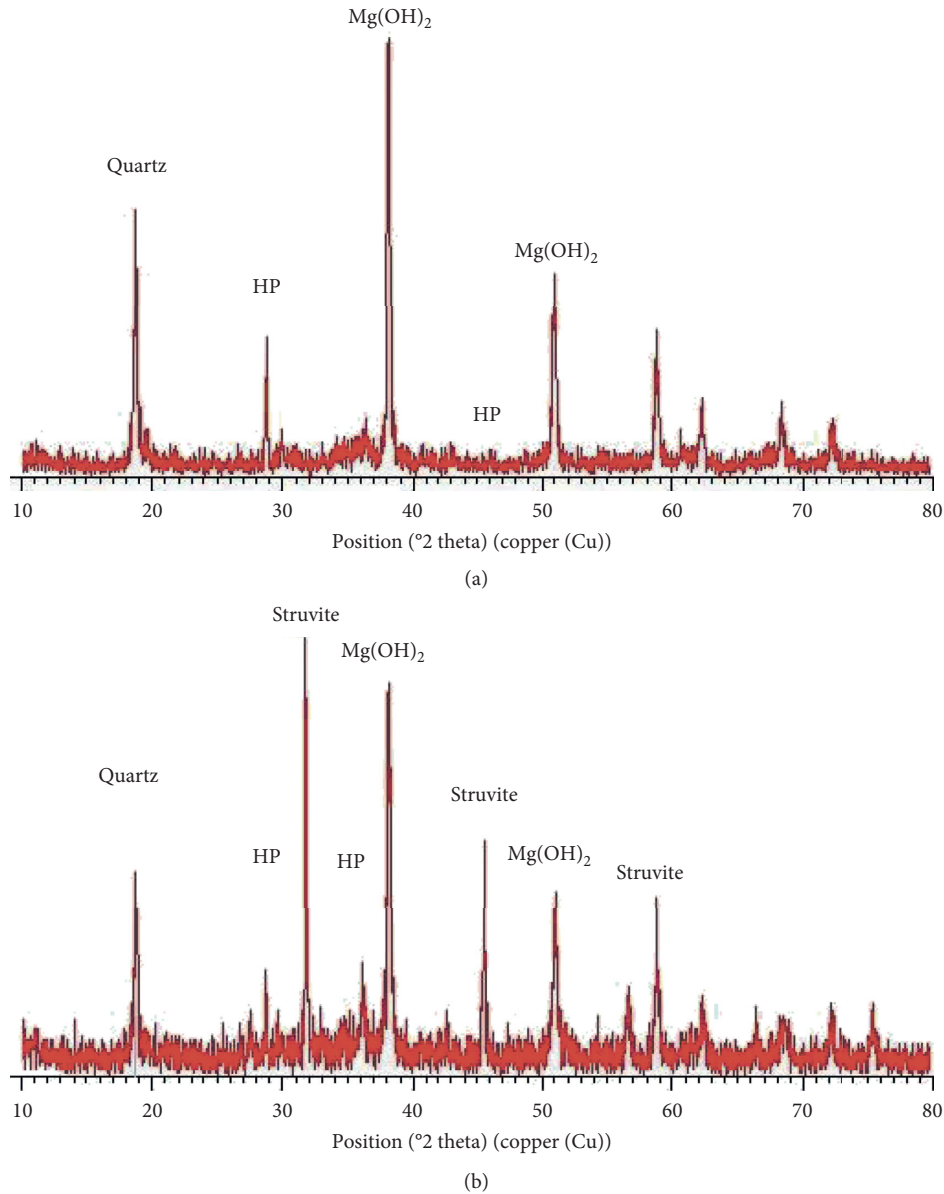
Figure 6: XRD analysis of (a) MB and (b) MPB sample.

4. Conclusion

The results of this study show that, unlike the mixture without phosphate, the mixture with the addition of phosphate represents the combination of 2 magnesium-based cements, MSH and phosphate ones. The water requirement is decreased due to the lower concentration of magnesium ions in the calcined powder; consequently, it reduces the water requirement than Ordinary Portland cement. The setting and consistency are attributed to insufficient hydrogen ions in the MB sample which is rectified through addition of phosphates, and this process leads to better results in MPB samples. The addition of phosphate also increases the agglomeration of microstructure which attributes to the strength increment, and the strength is influenced through magnesium hydroxide which is evident in XRD analysis. The calcination process has induced reactive magnesia which influences the heat of hydration and strength attainment over a period. The presence of $Mg(OH)_2$ and struvite influences the hydration and strength attainment. Thus, the study confirms that the calcined magnesite and steatite can be developed into a binder, and to improve the performance, the same phosphate has to be added which will give higher hydration and strength gain.

Data Availability

The data supporting this work are available in this article itself in Tables and Figures. Further clarification on the data will be available from the corresponding author upon request.

Conflicts of Interest

The authors declare no conflicts of interest.

References

[1] A. Hasanbeigi, L. Price, and E. Lin, "Emerging energy-efficiency and CO_2 emission-reduction technologies for cement and concrete production: a technical review," 2012.

[2] L. Mo, Y. Hao, Y. Liu, F. Wang, and M. Deng, "Preparation of calcium carbonate binders via CO_2 activation of magnesium slag," *Cement and Concrete Research*, vol. 121, p. 81, 2019.

[3] J. Morrison, G. Jauffret, J. L. Galvez-Martos, and F. P. Glasser, "Magnesium-based cements for CO_2 capture and utilisation," *Cement and Concrete Research*, vol. 85, p. 183, 2016.

[4] D. R. M. Brew and F. P. Glasser, "Synthesis and characterisation of magnesium silicate hydrate gels," *Cement and Concrete Research*, vol. 35, no. 1, p. 85, 2005.

[5] T. Zhang, C. R. Cheeseman, and L. J. Vandeperre, "Development of low pH cement systems forming magnesium silicate hydrate (M-S-H)," *Cement and Concrete Research*, vol. 41, no. 4, p. 439, 2011.

[6] J. J. Beaudoin and V. S. Ramachandran, "Strength development in magnesium oxychloride and other cements," *Cement and Concrete Research*, vol. 5, no. 6, p. 617, 1975.

[7] J. J. Beaudoin and V. S. Ramachandran, "Strength development in magnesium oxysulfate cement," *Cement and Concrete Research*, vol. 8, no. 1, p. 103, 1978.

[8] M. A. Haque and B. Chen, "Research progresses on magnesium phosphate cement: a review," 2019.

[9] J. Formosa, J. M. Chimenos, A. M. Lacasta, L. Haurie, and J. R. Rosell, "Novel fire-protecting mortars formulated with magnesium by-products," *Cement and Concrete Research*, vol. 41, no. 2, p. 191, 2011.

[10] F. Winnefeld, E. Epifania, F. Montagnaro, and E. M. Gartner, "Further studies of the hydration of MgO-hydromagnesite blends," *Cement and Concrete Research*, vol. 126, p. 105912, 2019.

[11] M. S. Shaikh, P. H. Shaikh, K. Qureshi, and I. Bhatti, "Green house effect and carbon foot print," 2018.

[12] A. Huhta and A. Kärki, "A proposal for the definition, nomenclature, and classification of soapstones," *GFF*, vol. 140, no. 1, pp. 38–43, 2018.

[13] H. Gökçe, D. Ağaoğulları, M. L. Öveçoğlu, İ. Duman, and T. Boyraz, "Characterization of microstructural and thermal properties of steatite/cordierite ceramics prepared by using natural raw materials," *Journal of the European Ceramic Society*, vol. 31, no. 14, pp. 2741–2747, 2011.

[14] R. Abinaya, K. G. Arunya, M. Gowsalya, and M. Malathy, "A new cement free binding material based on steatite powder activated through alkaline solution," *Master Build*, vol. 22, pp. 60–64, 2016.

[15] P. C. Hewlett, H. Justnes, and R. M. Edmeades, *Cement and Concrete Admixtures*, Elsevier, Berlin, Germany, 2019.

[16] K. Sudalaimani and M. Shanmugasundaram, "Influence of ultrafine natural steatite powder on setting time and strength development of cement," *Advances in Materials Science and Engineering*, vol. 2014, p. 1, 2014.

[17] P. Kumar, K. Sudalaimani, and M. Shanmugasundaram, "An investigation on self-compacting concrete using ultrafine natural steatite powder as replacement to cement," *Advances in Materials Science and Engineering*, vol. 2017, pp. 1–8, 2017.

[18] T. Luukkonen, Z. Abdollahnejad, J. Yliniemi, M. Mastali, P. Kinnunen, and M. Illikainen, "Alkali-activated soapstone waste - mechanical properties, durability, and economic prospects," *Sustainable Materials and Technologies*, vol. 22, 8 pages, 2019.

[19] C. Sadik, O. Moudden, A. El Bouari, and I. E. El Amrani, "Review on the elaboration and characterization of ceramics refractories based on magnesite and dolomite," 2016.

[20] D. Deng, "The mechanism for soluble phosphates to improve the water resistance of magnesium oxychloride cement," *Cement and Concrete Research*, vol. 235, 2003.

[21] X. Xu, X. Lin, X. Pan, T. Ji, Y. Liang, and H. Zhang, "Influence of silica fume on the setting time and mechanical properties of a new magnesium phosphate cement," *Construction and Building Materials*, vol. 235, 2020.

[22] B. Xu, B. Lothenbach, and F. Winnefeld, "Influence of wollastonite on hydration and properties of magnesium potassium phosphate cements," *Cement and Concrete Research*, vol. 131, 2020.

[23] J. Li, W. Zhang, and Y. Cao, "Laboratory evaluation of magnesium phosphate cement paste and mortar for rapid repair of cement concrete pavement," *Construction and Building Materials*, vol. 58, p. 122, 2014.

[24] Y. Liu and B. Chen, "Research on the preparation and properties of a novel grouting material based on magnesium phosphate cement," *Construction and Building Materials*, vol. 214, p. 516, 2019.

[25] B. Xu, B. Lothenbach, and H. Ma, "Properties of fly ash blended magnesium potassium phosphate mortars: effect of the ratio between fly ash and magnesia," *Cement and Concrete Composites*, vol. 90, p. 169, 2018.

[26] X. Luo, W. Fan, C. Li et al., "Effect of hydroxyacetic acid on the water resistance of magnesium oxychloride cement," *Construction and Building Materials*, vol. 246, 2020.

[27] Y. Liu, B. Chen, Z. Qin, D. Pen, and M. Aminul Haque, "Experimental research on properties and microstructures of magnesium-iron phosphate cement," *Construction and Building Materials*, vol. 257, 2020.

[28] Y. Liu, Z. Qin, and B. Chen, "Influence of low-grade bauxite on the properties of magnesium phosphate cement," *Construction and Building Materials*, vol. 242, 2020.

[29] Z. Qin, C. Ma, Z. Zheng, G. Long, and B. Chen, "Effects of metakaolin on properties and microstructure of magnesium phosphate cement," *Construction and Building Materials*, vol. 234, 2020.

[30] C. K. Chau, F. Qiao, and Z. Li, "Microstructure of magnesium potassium phosphate cement," *Construction and Building Materials*, vol. 25, no. 6, 2011.

[31] Z. Ding, Z. J. Li, and F. Xing, "Chemical durability investigation of magnesium phosphosilicate cement," 2006.

Research Article

Efficiency of Different Electrolytes on Electrochemical Chloride Extraction to Recover Concrete Structures under Chloride-Induced Corrosion

Thamara Tofeti Lima ⬤ **and Ki Yong Ann** ⬤

Department of Civil and Environmental System Engineering, Hanyang University, Ansan 15888, Republic of Korea

Correspondence should be addressed to Ki Yong Ann; kann@hanyang.ac.kr

Chloride-induced corrosion is one of the main causes of concrete deterioration and imposes a challenge to sustainability. Traditional techniques to repair corroded structures consisted of basically removing the damaged area, which was either economical or sustainable. Therefore, electrochemical chloride extraction (ECE) gained popularity for being an efficient non-destructive treatment applied temporarily to structures. On this line, this manuscript aims to raise the efficiency of ECE by an optimal decision of the treatment setup concerning the electrolyte choice. Three different electrolytes were tested, namely, tap water, calcium hydroxide, and lithium borate. Experimental results pointed to lithium borate as the most efficient electrolyte for extracting chlorides while calcium hydroxide was a better choice to repassivate the structure and even heal cracks, due to a possible electrodeposition of the electrolyte ions on the cement matrix. Thus, depending on the main goal of the treatment, different electrolytes achieve a better performance, which highlights the importance of pretreatment evaluation to see in which stage of corrosion damage is the structure.

1. Introduction

Corrosion of reinforcing steel due to exposure to chloride leads to degradation of reinforced concrete structures. Dating from the early 60's, electrochemical treatments raised as plausible options being nondestructive methods to prevent or/and recover corrosion of steel in concrete, by extracting aggressive agents such as chlorides or restoring alkalinity of concrete. Electrochemical chloride extraction (ECE) is one example, which is based on the mechanism of a direct current that flows through an anode fixed to the concrete surface, an alkaline electrolyte, and the reinforcing steel acting as the cathode, aiming the removal of chloride ions [1–4]. Figure 1 shows a schematic representation of the mechanisms and chemical reactions involved on ECE. The degree of chloride extraction is frequently measured by grinding the concrete cover, and it is mostly known to vary from 30 to 60% of removed chlorides depending on

innumerous variables [5–18]. The setup to perform ECE has many particularities that can significantly affect its efficiency [7, 15–17]. Three major variables play an important role during the chloride removal process: the direct current, the electrolyte solution, and the external anode; therefore, the choice over them is of great importance and guidelines suggest some options, different from each other [19–21].

The chloride extraction rate is mostly measured considering the total concentration of ions in the bulk concrete, rather than chloride profiles at different depths of the cover concrete, although profiles may provide more direct and clear information on modified concentrations under electric charge, considering the penetration depths [20, 22–25]. Various externalities can easily influence the treatment, such as the environmental temperature during treatment [26], a high concrete resistance on site which decreases the efficiency of current passed, insufficient coverage of the anode, and arrangement of stirrups and steel rebars [19, 27, 28]. Due
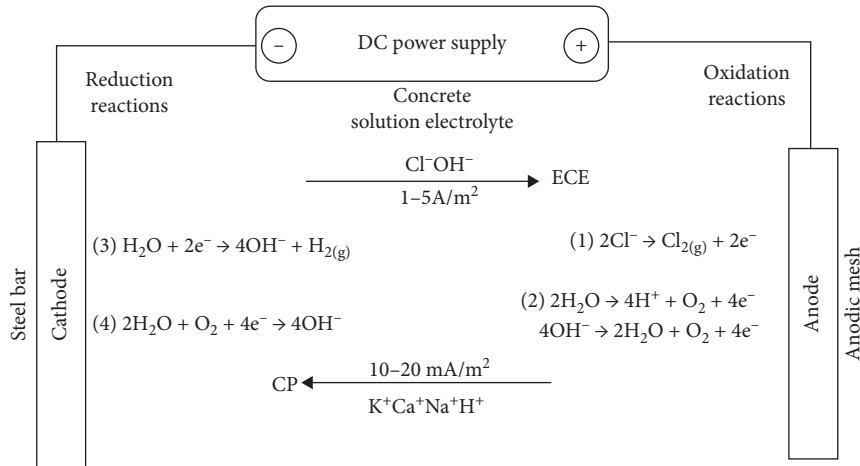
FIGURE 1: Mechanism of main electrochemical treatments and chemical reactions involved in the processes [6].

to that, different removal rates may occur at the same structural component, and results based only on the chloride extraction rate of the bulk concrete can be inconclusive.

Moreover, a change in the chloride mobility after ECE has been rarely taken into account. Chlorides are usually present in the cement matrix in the form of free and bound ones. Bound chlorides are divided into physically and chemically bound; the chemically bound is related to the reaction between chloride ions and C_4AF or C_3A, forming Friedel's salt, while physical binding is related to the adsorption of chloride ions to the C-S-H hydration products. For a certain time, it has been taken as a statement that only free chlorides impose the mobility in concrete, which would be the only type possibly removed by electric charge. However, the removal of bound chlorides in concrete under electric charge is being proposed by few authors up to date [15]. According to Sun [29], the majority of the physically bound chlorides can be easily extracted from C-S-H gel, by physical adsorption. An increased temperature can already accelerate the thermal vibration of absorbents releasing more free chlorides. In addition, some of chlorides adsorbed on the surface of hydrations are physically trapped in the unstable state and thus may be often mobilized by a strong driving such as the electromigration forces in ECE [30]. Chemically bound chlorides could achieve the mobility in concrete as well by acidification of the pore solution [31] and other modified environments of concrete.

On which concerns the setup of ECE, up to date, standards are still being elaborated around the world. For example, concerning electrolytes, SHRP-S-347 [32], the most common American guideline, indicates the usage of a borate-buffered electrolyte to avoid alkali silica reaction (ASR) during the process, while the European Standard [33] does not specify any solution, just mention that it should be alkaline, and the Norcure [34] patent suggests fresh water. Therefore, considering the lack of unified standards or guidelines pointing out the most efficient setup for ECE, in the present study, the chloride profile and chloride types for untreated and treated specimens were taken considering three different electrolytes, namely, tap water, calcium

hydroxide, and lithium borate. Sodium chloride was added to the mixing water (3% Cl^- by mass of cement) to promote the corrosion onset from the beginning before applying the repair treatment. ECE was then applied at $2 \, A/m^2$ for 4 weeks. The pH of electrolyte solution and voltage of the circuit were constantly monitored. The corrosion state was checked in terms of electrical potential, corrosion rate, and mass loss. The chloride profile was taken immediately after the completion of the treatment, differentiating acid soluble and water soluble chlorides to reflect the influence of chloride mobility under electrochemical treatment. Substantially, the change of chloride profiles after the treatment was interpreted paired with corrosion rate and corrosion potential measurements during treatment.

2. Experimental Program

The specimen preparation to investigate the chloride removal consists of casting the specimens, curing, and applying a DC. To reduce the possible influence of coarse aggregate on chloride distribution, mortar was used instead of concrete. The mixture proportions used in manufacturing the specimens for Ordinary Portland Cement : water : sand (Grade M) was 1.00 : 0.45 : 2.15. Table 1 shows the oxide composition of the binder. Sodium chloride was added to the mixing water (3% Cl^- by mass of cement) to promote the corrosion onset from the beginning before applying the repair treatment. Specimens were cast in a 150 mm cubic mold with a centrally located 10 mm diameter mild plain steel bar, containing 3 replications each to guarantee accuracy of results. The ends of the steel bars were masked off using a cementitious coating and then covered with heat-shrink insulation to avoid corrosion under the masking material. The specimens were then cured for 28 days at $21 \pm 2°C$. After curing, the corrosion state of the rebar was evaluated by electrochemical techniques before treatment. Both the corrosion potential (E_{corr}) and polarization resistance (Rp) were periodically obtained. The Rp was obtained by linear scan sweep from $-20 \, mV$ to $+20 \, mV$ versus E_{corr} at $10 \, mV/min$. Applying the equation of Stern and Geary [35, 36],

TABLE 1: Oxide composition of ordinary Portland cement used for the experimental work.

Binder	Oxide composition (%)						Ignition loss (%)	Fineness (cm^2/g)
	CaO	SiO_2	Al_2O_3	FeO	MgO	SO_3		
OPC	60.0	23.0	5.0	2.0	1.0	2.0	2.1	3120

the corrosion current density (i_{corr}) was obtained. Mean values are given for each sample.

The chloride extraction treatment was performed using an impressed current density of $2 A/m^2$ of mortar surface for 4 weeks. Three types of electrolyte, namely, saturated $Ca(OH)_2$, tap water, and lithium borate at 0.1 molar concentration were used. Mortars were treated after approximately only 28 days of curing, which is standard for most experiments, as an alternative to optimize the experimental schedule, considering that the main focus of the manuscript is given to the influence of electrolytes less than that to the microstructural changes. During the application of the electric charge, the specimens were immersed in an acrylic box filled with the different electrolytes, one at each time. A $15 \times 15 cm^2$ titanium mesh plate with a thickness of 2 mm was used as the external electrode (anode) and placed inside the acrylic box as well close to the concrete surface in all directions. A direct electric potential was applied from the regulator between the reinforcement bars and the external electrode. Voltage was accordingly increased up to $20 \pm 1 V$ in the beginning of the treatment to maintain the current density for 4 weeks. The total charge passed substantially accounted for $1344 Ah/m^2$. Figure 2 shows the experimental setup for applying the electrochemical chloride extraction to one specimen. The pH of the electrolyte solution and voltage of the circuit were constantly monitored to guarantee safety and efficiency of treatment as in Figure 3. After treatment was completed, specimens were removed from the acrylic box and kept in constant relatively humidity and temperature. To perform the corrosion measurements, the response of the rebars was periodically measured after 10 days (depolarization time) to evaluate the effectiveness of the treatment and the ability of repassivation of rebars according to different electrolytes.

To measure the chloride ion concentration, mortar powder was drilled from the specimens at the core obtaining dust samples. Specimens were ground by a diamond-grit plate from the surface in the direction of steel rebar at 1.0 mm first, next 5.0 mm, and then at consecutives increments of 5.0 mm up to 2 mm of the cover depth. Samples were diluted in solvents to extract chloride ions. The chloride concentration in solution was obtained before and after treatment, determining the concentration of free, bound, and total chlorides at every depth. To avoid biased results on chloride concentration, dust samples were obtained at all 3 replications and their average value was taken. The chloride concentration was then determined for both water soluble and acid soluble chlorides. In fact, the water soluble chloride measured by the following method was regarded as free, whilst acid soluble as total. Simultaneously, the concentration of bound chlorides was determined by subtracting free from total values. On what concerns the measurement of water soluble chlorides, dust samples were diluted in 50°C distilled water and stirred for 3 minutes. After 30 minutes,

the suspension was filtered using a paper filter. Then, the concentration of chloride ions was measured by the potentiometric titration against silver nitrate, and the values obtained are referred as free chlorides. Simultaneously, the sample was also used to determine the concentration of acid soluble chlorides by using on this turn distilled water and nitric acid. The obtained suspension was boiled for 1-2 minutes and filtered by the same paper filter, followed by cooling down to the ambient temperature and the titration against silver nitrate to determine the acid soluble chloride concentration, which are referred as total chlorides. Untreated specimens were used to measure the chloride profile immediately after curing, therefore making results for pretreatment.

3. Results

3.1. Chloride Removal Rates. Figures 4–6 illustrate the chloride concentration profiles before and after ECE process for the three different electrolytes which were determined in terms of total, free, and bound. As all specimens were mixed in same conditions, the initial levels of chlorides before treatment are similar for all cases and for free chlorides always above the chloride threshold at all levels, implying a high risk of corrosion. The concentration of chlorides at shallower depths is higher as it is expected, considering that the concentration near the core of the specimen hydration of cement is expected to be at a higher degree. From a first look at the figures, it is evident that the treatment was effective in extracting chloride ions for all cases at different extents. However, in all cases considering the total chlorides, the concentration at shallow depths (i.e. <5.0 mm) was less reduced as it is expected and may be attributed to a delayed dissolution of chlorides into the electrolytic solution after being transported to the surface of concrete during treatment. Due to the imbalance in ionic media between concrete substrate and liquid electrolyte, chloride ions could be intermittently present in the nearer surface. Moreover, the greater chloride content near the surface may be also attributed to the accumulation of chloride ions under the effect of migration, because chloride profiling was performed in the dry condition of concrete.

Figure 4 represents the results for tap water as an electrolyte, highlighting that three replications were used and the mean values are presented. Figure 4(a) shows that total chlorides before treatment ranged from 2.10–4.19% (by weight of cement) decreasing with the increase in depth. After treatment, the total chloride concentration was reduced to 1.35–3.20% at all depths, resulting on a percentage removal efficiency of 23.6–42.2% depending on the cover depth. Figure 4(b) represents the profiles for free chlorides before and after treatment. The concentration of free
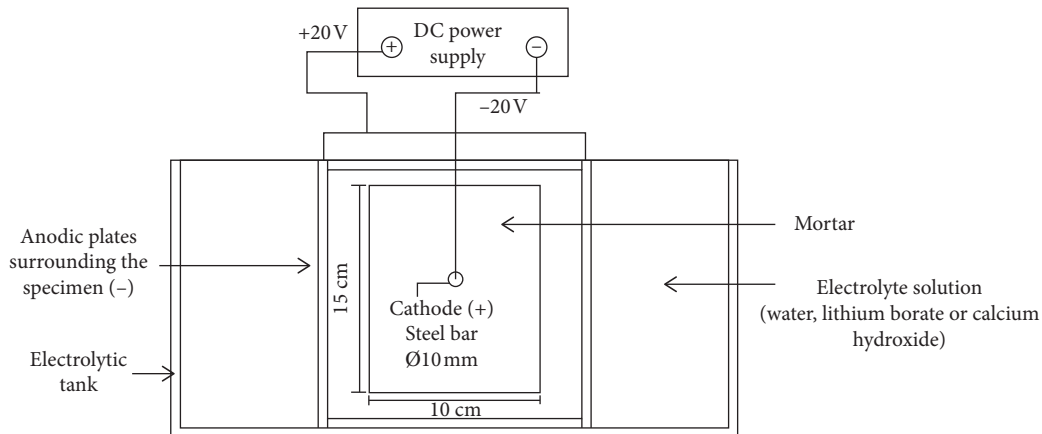
FIGURE 2: Schematic representation of the experimental setup for ECE using different electrolytes in aerial perspective. Each electrolytic tank contained 3 replications of each sample for better confidence of results.
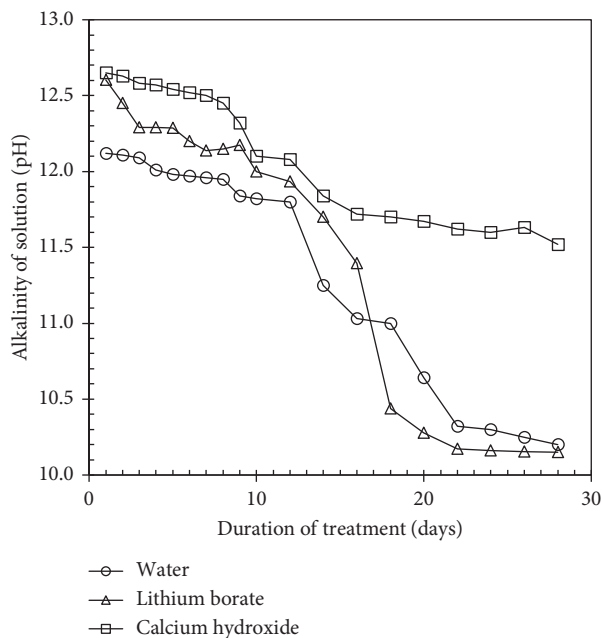

FIGURE 3: Electrolyte pH and voltage of circuit during treatment.

chlorides before treatment ranged from 0.75–1.89% by weight of cement, increasing for shallower depths. After treatment, the free chloride concentration was decreased at all depths accounting for 0.32–1.13% by weight of cement. It means that the treatment was efficient in this point as expected to remove free chlorides at levels lower than the chloride threshold to initiate corrosion. Figure 4(c) presents the results obtained for bound chlorides. The quantity of bound chlorides ranged from 1.35 to 2.30% by weight of cement in untreated specimens, while after treatment, a considerable reduction is perceived and the range of bound chlorides was limited distributed to about 0.96–1.87%. It implies that bound chlorides were partially removed under electric field, and for that, they must have achieved some mobility. Moreover, for depths greater than 5.0 mm, the residual bound chlorides converged to a continuous range of 1.37–1.87%.

In turn, Figure 5 represents results calcium hydroxide as the electrolyte. Figure 5(a) shows that total chlorides before treatment ranged from 1.97–4.10% (by weight of cement) decreasing with the increase in depth. After treatment, the total chloride concentration was reduced from 1.20 to 3.00% at all depths, resulting on greater removal efficiency than it was found for tap water as the electrolyte. Figure 5(b) represents profiles for free chlorides before and after treatment. The concentration of free chlorides before treatment ranged from 0.72 to 1.77% by weight of cement, increasing for shallower depths, being above the chloride threshold at all levels as it was previously mentioned. After treatment, the free chloride concentration was decreased at all depths accounting for 0.23–0.97% by weight of cement, being more efficient than water in this case as well, removing free chlorides at levels lower than the chloride threshold to initiate corrosion. Figure 5(c) represents the results obtained for bound chlorides. The quantity of bound chlorides ranged from 1.26 to 2.33% by weight of cement in untreated specimens, while after treatment as it was seen for water, a considerable reduction is perceived and the range of bound chlorides was limited to about 0.83–1.78%. Moreover, at increasing depths, the concentration of bound chlorides also converged to a specific range between 1.38 and 1.78%.

Figure 6 represents the results obtained using lithium borate as electrolyte. Figure 6(a) shows that the concentration of total chlorides in the specimens initially ranged from 2.05–3.88% (by weight of cement) at all depths. After treatment, these values were reduced to 0.88–2.86% depending on the cover depth. In particular, for this electrolyte, the sharpest reduction on total chloride level was obtained around 5.0 mm of the depth, where the residual chloride concentration accounted for only 1.15%, whilst untreated specimen contained 2.95%. For depths exceeding 5.0 mm, the total chloride content was reduced into a similar range of values being around 0.88–1.00%, being the most efficient removal among the three electrolytes. Figure 6(b) presents the profiles for free chlorides before and after treatment. The concentration of free chlorides was found to be in the range of 0.86–1.95% by weight of cement immediately after mixing, increasing for the shallower depths,
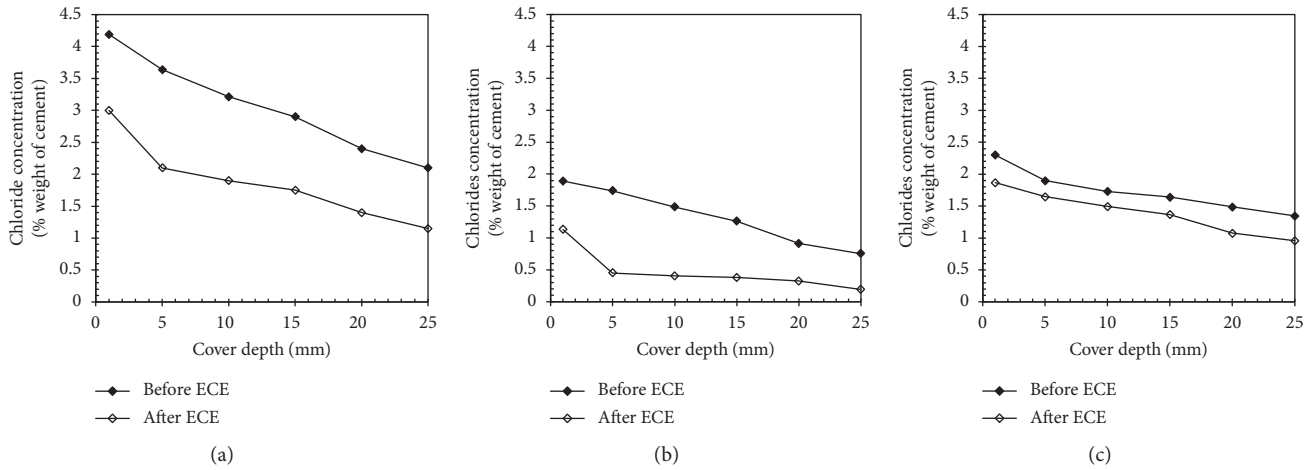
FIGURE 4: Chloride profiles before and after treatment using water as electrolyte for at 2 A/m^2 constantly for 4 weeks, in terms of (a) total*, (b) free**, and (c) bound *** chlorides. *(a) Total: acid soluble titration against silver nitrate at the ambient temperature. **(b) Free: water soluble chlorides dissolved in 50°C distilled water. ***(c) Bound: values obtained by subtracting the free chloride concentration from the total at each depth.
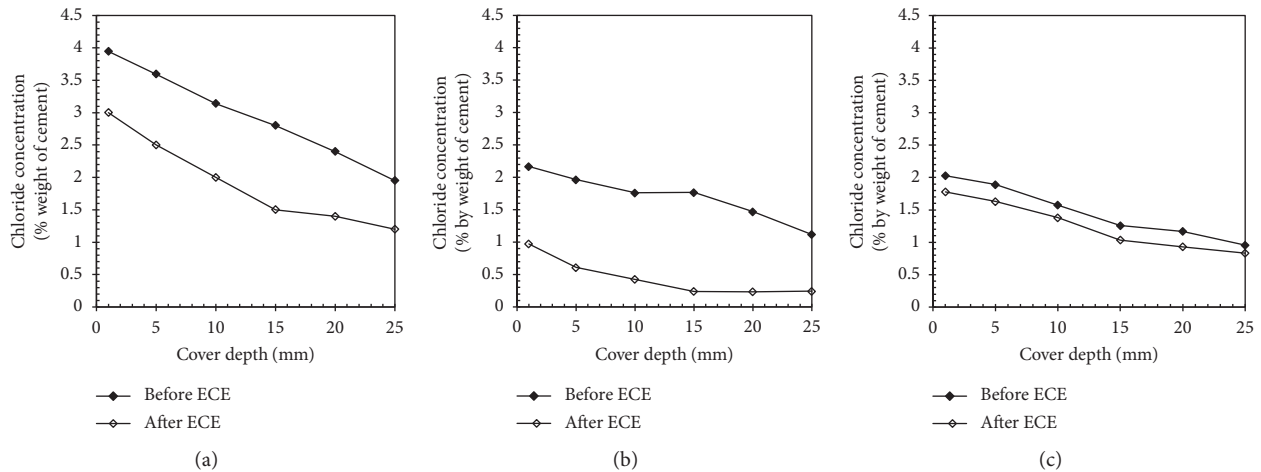
FIGURE 5: Chloride profiles before and after treatment using calcium hydroxide as electrolyte for at 2 A/m^2 constantly for 4 weeks, in terms of (a) total*, (b) free**, and (c) bound*** chlorides. *(a) Total: acid soluble titration against silver nitrate at the ambient temperature **(b) Free: water soluble chlorides dissolved in 50°C distilled water ***(c) Bound: values obtained by subtracting the free chloride concentration from the total at each depth.

above the chloride threshold. After treatment, the free chlorides concentration was sharply decreased almost to an insignificant level for all depths exceeding 5.0 mm, accounting for less than 0.21% by weight of cement and less than 0.06% for depths exceeding 10.0 mm. It means that treatment was the most efficient in this case and mostly free chlorides were in turn removed from concrete. At the surface of concrete (<5.0 mm), the concentration of free chloride was higher than that before treatment, ranging from 1.26 to 1.93%, which is mainly due to the delayed dissolution of chloride ions in the electrolytic solution in the tank. However, the free chlorides at the nearer surface concrete could be easily removed by subsequently washing when the anodic system is removed, therefore imposing no risk of further corrosion process. Figure 6(c) presents the results obtained for bound chlorides. The quantity of bound

chlorides ranged from 1.21 to 1.93% by weight of cement in untreated specimens, while after treatment, again the reduction is perceived and the range of bound chlorides was distributed to about 0.87–1.81% depending on the depth. For depths greater than 10.0 mm, the residual bound chloride also converged to a limited range of 1.14–1.81%. The removal of bound chlorides for all electrolytes contradicts the idea that only free chlorides may be mobile on the concrete pore solution. In addition, seeing that ECE is able to reduce the concentration of all chloride types, the risk of further corrosion is surely reduced, although the residual concentration for water and calcium hydroxide was still above the chloride threshold level for some depths.

Figure 7 summarizes the results for the chloride removal rates in percentage, making a direct comparison among all three electrolytes for each depth interval. In general, for
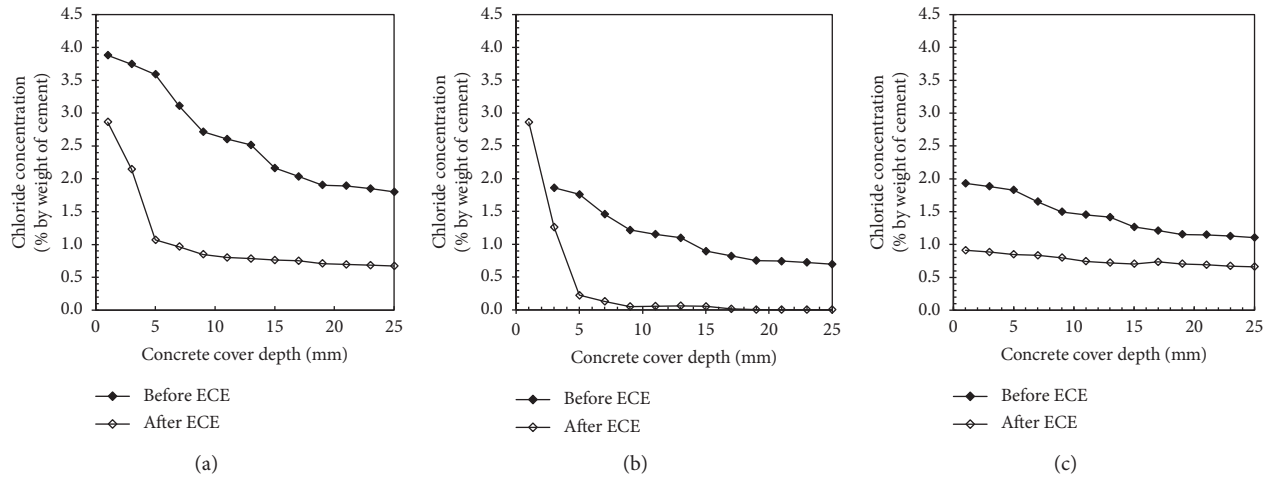
FIGURE 6: Chloride profiles before and after treatment using lithium borate as electrolyte for at 2 A/m^2 constantly for 4 weeks, in terms of (a) total* , (b) free** , and (c) bound*** chlorides. *(a) Total: acid soluble titration against silver nitrate at the ambient temperature. **(b) Free: water soluble chlorides dissolved in 50°C distilled water. ***(c) Bound: value obtained by subtracting the free chlorides concentration from the total at each depth.
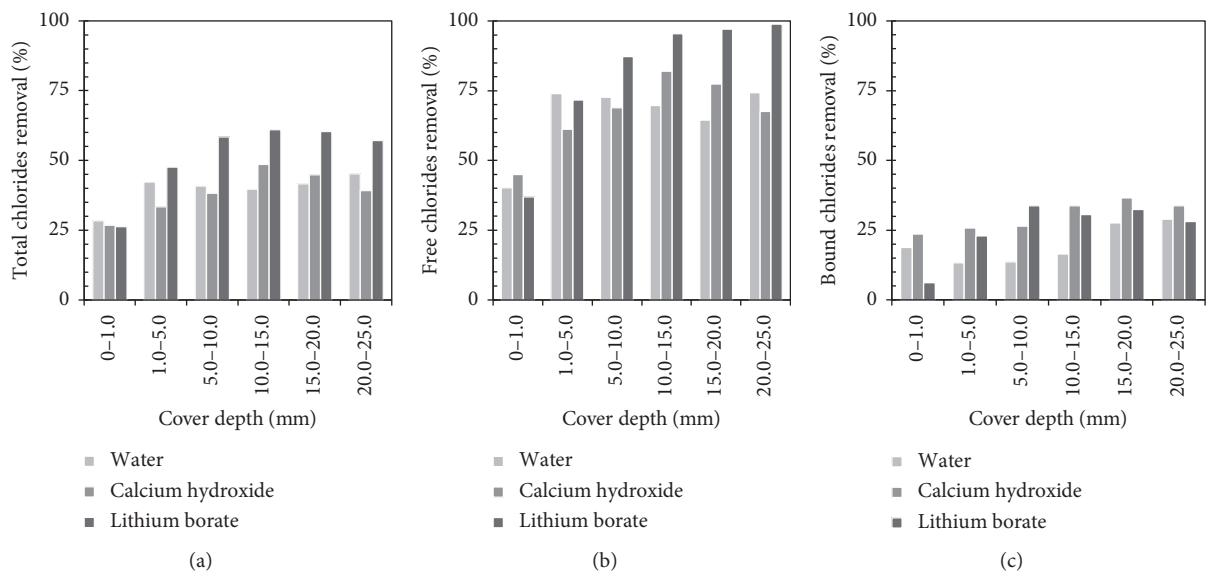

FIGURE 7: Direct comparison on the efficiency on chloride removal for each designated cover depth in terms of (a) total, (b) free, and (c) bound chlorides.

lithium borate, a more expressive chloride removal is perceived for all chloride types. As it is shown in Figure 7(a), the removal efficiency of total chlorides ranged from 26.3–61.0% depending on the cover depth, while for water and Ca(OH)$_2$, the removal occurred at more similar values, resulting in percentage removal efficiencies of 23.6–42.2% and 26.7–48.6%, respectively, showing only a slightly better performance of Ca(OH)$_2$ but still not better than the first one. The chloride removal was always greater at increasing depths for reasons already mentioned. In Figure 7(b), taking into consideration only free chlorides, lithium borate again had a considerable better performance, accounting to a percentage removal efficiency of 36.9–98.8%. For Ca(OH)$_2$,

the reduction occurred at significant amounts as well but not as efficiently, showing a percentage removal efficiency of 45%–82% depending on the cover depth. For tap water as the electrolyte, the free chloride removal was less significant, being the least efficient one. The concentration of free chlorides after treatment was reduced at a percentage removal efficiency of 40%–74% depending on the cover depth. On the same line, Figure 7(c) represents the direct comparison of results obtained for bound chlorides. A considerable removal could be perceived for all cases. In fact, different percentage removal was found for different electrolytes being the maximum of 28% for tap water as electrolyte, 36% for calcium hydroxide, and 33% for lithium

borate. The removal was slightly more significant at greater depths. The fact that, independent of the electrolyte, the efficiency in removing the bound chlorides is always similar may implicate that part of bound chlorides cannot be removed under any circumstance but cannot be turn into mobile neither, being stable and not participating on corrosion initiation.

3.2. Corrosion Potential and Corrosion Rate.

Concerning the repassivation of the steel bar during treatment, the results are shown in Figure 8. Corrosion potential values at the beginning of treatment were nearly −700 to −600 mV vs. SCE for all cases as it can be seen in Figure 8(b), which implies that the steel bar was much corroded and had lost the passivity. The values were constantly monitored during treatment for all 3 different electrolytes and increased slowly during treatment, being the biggest increment between 1 and 3 weeks. At the end of treatment, values raised to −293, −315, and −350 mV vs. SCE for $Ca(OH)_2$, water, and lithium borate, respectively, pointing to calcium hydroxide as a better option when considering repassivation after treatment and consequently protecting against further corrosion. Corrosion potential values are not yet on the passive condition (>−275 mV vs. SCE). However, as it was mentioned earlier in this paper, it seems inconclusive to analyze repassivation without a visual examination on the steel surface and without quantitative informative data such as corrosion rate or mass loss. Some authors [20, 21, 37] mentioned that it is not correct to rely in a fixed value to define if passivation is achieved by electrochemical treatment because many factors can influence that condition and ECE can induce more negative potentials of rebars because of strong polarization, meaning that readings one or two months after the end of treatment may show even a less negative potential than the one already achieved. In order to minimize the doubts about repassivation, a quantitative technique was used to ensure the corrosion state after ECE and measure the corrosion rate by linear polarization [38]. Results shown in Figure 8(a) pointed that the corrosion rate was significantly reduced by the electrochemical treatment. Before treatment, the values arose to around 500 to 1000 $\mu A/cm^2$ which points to highly corroded state of the steel rebar. By the end of treatment, the values were reduced to around 23, 286, and 107 $\mu A/cm^2$ for $Ca(OH)_2$, water, and lithium borate, respectively.

3.3. Visual Inspection and Mass Loss.

In order to confirm visually and quantitatively the state of rebars after treatment, specimens were broken and the steel bar was removed. Figure 9 shows the rebars after ECE treatment and immersion in hydrochloric acid (HCl, sp. gr. 1.19) at 25°C for 2 hours to clean the rust. Bars were brushed in addition for better results. Results achieved from corrosion potential and corrosion rate could be confirmed visually, considering that rebars from specimens treated with $Ca(OH)_2$ were in a considerable better state than the ones treated with water, where pit cracks can be easily seen. Table 2 summarizes the results. The backscattered mass loss for noncontaminated

and noncorroded specimens accounted for around 0.017 to 0.034%. For specimens treated with water, calcium hydroxide, and lithium borate, the percentual mass loss ranged from 1.37 to 1.63%, 0.39 to 1.19%, and 1.18 to 1.58%, respectively. As it was expected, the specimens treated with water had the biggest percentage of mass loss which suggested a still more corroded state when compared with that of the other cases. Moreover, the visual examination confirmed the hypothesis that the steel bar was in a more alkaline environment for the specimens treated with the other two electrolytes.

4. Discussions

4.1. Removal of Bound Chlorides.

At first, it is important to highlight for discussion that, independent of the electrolyte solution, bound chlorides were extracted at all depths. The presence of chlorides in the cement matrix is proved to be directly affected by some factors such as chemical properties of the pore solution, alkalinity, and hydration products. It is from common knowledge that, in concrete, chloride ions are usually divided into three types according to their stability: free, physically bound, and chemically bound. Chloride ions adsorbed or trapped to hydration products or chemically connected to other molecules such as for Friedel's salt are often regarded as "bound chlorides" and are originally regarded immobile in concrete at normal conditions (no acidification of the pore solution). On the other hand, free chloride ions have total mobility and can react easily to initiate the corrosion process, therefore being considered to be mainly responsible for a high risk of chloride-induced damage. Simultaneously, by having this high mobility, there is no doubt that free chloride ions tend to be mostly removed by electrochemical treatment, as it was proved by the experimental results exposed on this manuscript.

Chemically bound chlorides, which connect C_3A and C_4AF molecules and form a compound referred as Friedel's salt, are unreactive and consequently immobile through the pore solution as long as the cement matrix is kept highly alkaline in the way it is supposed to be. However, the acidification of the pore solution in concrete may often occur at the pit nucleation on the surface of steel, when corrosion is taking place, accompanying a build-up of chloride ions. The acidification is explained, because during the corrosion initiation, H^+ ions might evolve in the vicinity of steel, which simultaneously react with chloride ions and produce hydrochloric acid [39–41]. According to Elsener and Angst [1], there are two main steps: most bound chloride is released at pH values lower than 12.5 and then another part is dissolved around pH 12, suggesting that, at even lower pH values, nearly no bound chloride is left in the concrete. Consequently, part of these bound chlorides would be released and turned into free chlorides by pH fall which would take place in the vicinity of steel rather than in the concrete body.

Withal, according to the results shown by chloride profiles, bound chlorides were removed at all depths after electrochemical treatment and not only nearby the steel bar, which confirms that not only the chemically bound chlorides
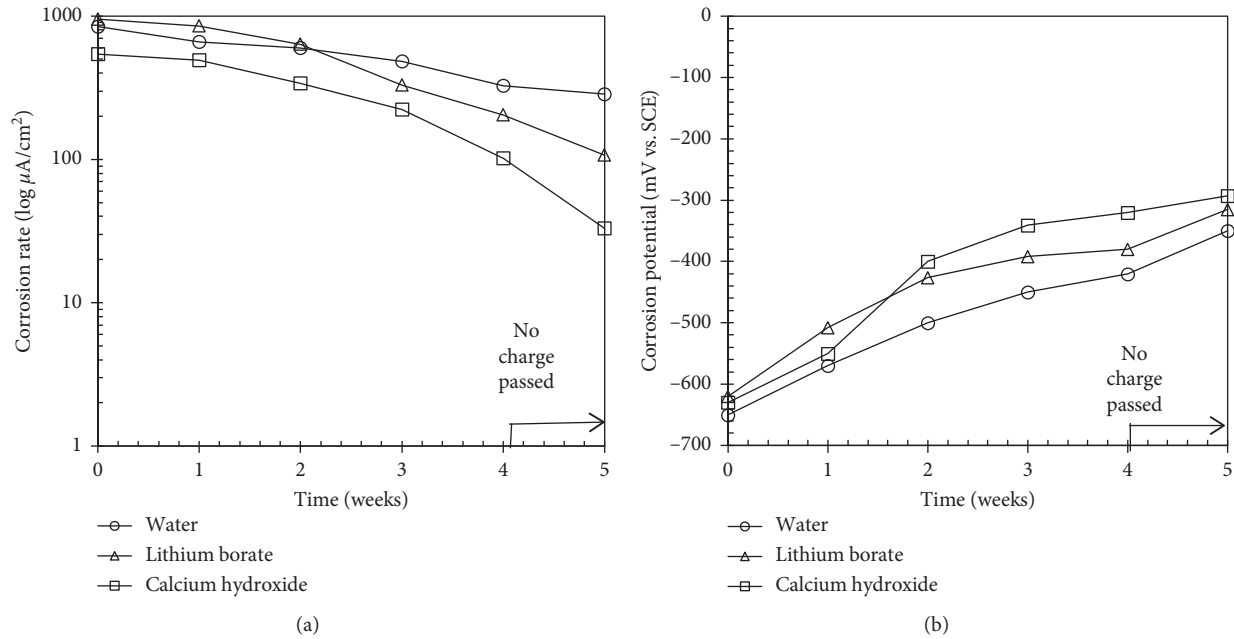
(a)

(b)

FIGURE 8: Corrosion values measured at each given charge passed during and after treatment* in terms of (a) corrosion rate** and (b) corrosion potential ***. *Posttreatment values are depicted in the highlighted area of the graph to show that no current was applied in that interval; measurements were performed at 5 weeks to ensure the quality of results after depolarization time. **(a) Corrosion rate values obtained by linear polarization at scan rate from $-20\,mV$ to $+20\,mV$ versus Ecorr at $10\,mV/min$ and Stern and Geary equation. Mean values are given for each sample. ***(b) Corrosion potential values obtained by half-cell potential and the measurement of corrosion potential of rebar with respect to a saturated calomel electrode (SCE). Mean values are given for each sample.

(a)   (b)
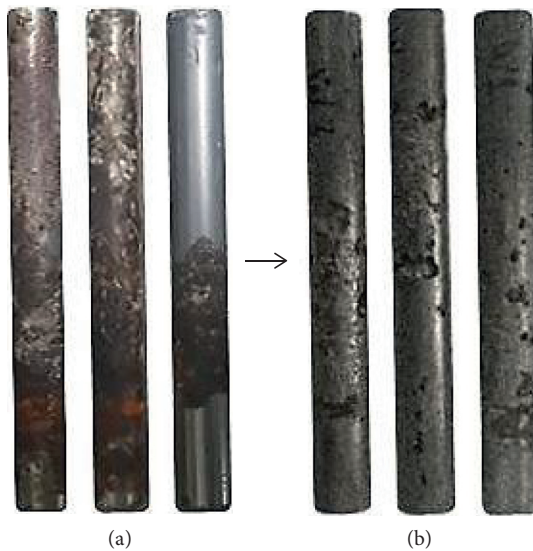
FIGURE 9: Visual aspect of bars after ECE treatment and immersion in hydrochloric acid (HCl, sp gr 1.19) at $25°C$ for 2 hours to clean the rust. Bars were brushed in addition for better results. The following cases depicted are in order from specimens treated with water, lithium borate, and calcium hydroxide, respectively, (a) right after treatment and (b) after rust cleaning.

were being released. Bound chlorides removed at farther depths from the steel bar may be the physically adsorbed ones that are usually adsorbed on the surface on the C-S-H gel or trapped between precipitated $Ca(OH)_2$ molecules.

Physically bound chlorides can be easily released by changes on the environmental conditions, such as high temperature, that can accelerate the desorption process and turn them into free ones [42]. Substantially, the desorption of chloride ions could occur, despite of the acidification that affects the chemically bound chlorides, therefore being possible to occur at shallower depths. Furthermore, the removal of bound chlorides by electrochemical chloride extraction might be strongly dependent on the degree of chloride contamination in concrete [43], together with the applied current density and duration of the treatment, which may determine the driving force for free chloride ions and simultaneously affect the rate of decomposition for the bound ones.

4.2. Differences between Electrolytes for the Efficiency of Treatment.

According to the results presented on the efficiency of the treatment on extracting chlorides, overall, lithium borate had the best performance followed by $Ca(OH)_2$ and water. The smaller efficiency of calcium hydroxide might be explained by a process of electrodeposition of the electrolyte ions on pores of the cement matrix during treatment. The precipitation of certain ions on the concrete pores is proved from the late 80's when the electrodeposition method was developed in Japan as a crack-repair treatment, where a direct current is provided between the reinforcing steel bar and an anode placed on the concrete surface, a system which is pretty similar to the one used for chloride removal [44]. The effectiveness of this method for crack

TABLE 2: Results obtained by weighting the steel bars before and after treatment.

	Replications	Weight before casting (g)	Weight after treatment (g)	Percentual mass loss (%)
Control (backscattered loss)	1	58.05	58.04	0.017
	2	58.02	58.00	0.034
	3	58.03	58.01	0.034
Water	1	58.03	57.08	1.637
	2	58.04	57.24	1.378
	3	58.02	57.09	1.603
Calcium hydroxide	1	58.03	57.41	1.068
	2	58.05	57.52	0.930
	3	58.04	57.35	1.189
Lithium borate	1	58.05	57.28	1.326
	2	58.06	57.14	1.585
	3	58.04	57.35	1.189

repair in marine concrete structures is confirmed by several authors, and in several cases, calcium hydroxide is used. Therefore, during the electrochemical chloride removal process, the current applied probably induces the precipitation of $Ca(OH)_2$ ions on pores of the cement matrix, blocking the network and reducing the mobility of chlorides ions, when compared with other electrolytes. Notwithstanding, tap water still showed a slightly lower efficiency, and that on the other hand may be explained simply by the fast acidification of the electrolyte and a constant need of replacement, which may obviously influence the treatment by reducing electromigration forces.

Moreover, electrodeposition may be also the factor to explain the better performance of calcium hydroxide to repassivate the structure after treatment. By filling up pores and consequently some possible cracks being caused by the corrosion process, a partial recovery on the repassivation of rebars could be achieved. Normally, the authors mention that the decrease of corrosion rate and partial recovery of half-cell potential are only related to the chloride removal, which are not the only reasons. The pH of the electrolyte solutions used during ECE and the voltage of circuit were monitored during the 4 weeks and are shown in Figure 3. After the first 2 weeks of treatment, there was a decrease in the pH of electrolytes. The pH reduction of electrolytes could be explained by the chlorine gas evolution, prevenient of the chlorides removed during treatment, if analyzed individually. However, for calcium hydroxide, the pH decrease was smaller and there was a significant increase in the voltage of the circuit, meaning an increase of concrete resistance. This shows that the pH fall may be additionally attributed to a migration of alkaline ions from the electrolyte solution to the concrete pore structure, being one more supporting factor to prove that electromigration happens during the electrochemical treatment. Thus, calcium hydroxide may not be the most efficient on removing chlorides, but it heals the structure at another level. In summary, depending on the main goal of the treatment, different electrolytes will show better performances, which also make it important to consider the pretreatment evaluation to see in which stage of corrosion damage the structure is.

5. Conclusions

In this study, ECE treatment was applied to mortar specimens containing sodium chloride added to the mixing water (3% Cl^- by mass of cement) to promote the corrosion onset from the beginning. ECE was applied at $2\,A/m^2$ for 4 weeks using three different electrolytes, namely, tap water, calcium hydroxide and lithium borate, while the pH of electrolyte solution and voltage of the circuit were constantly monitored. The chloride profile and chloride types for untreated and treated specimens were taken, and the change of chloride profiles after the treatment was interpreted paired with mass loss, corrosion rate, and corrosion potential measurements before and after treatment. The following conclusions were drawn from the experimental results:

(1) In general, for lithium borate, a more expressive chloride removal is perceived for all chloride types. The removal efficiency of total chlorides ranged from 26.3 to 61.0% depending on the cover depth, while for water and $Ca(OH)_2$, the removal was lower and at similar rates, resulting on percentage removal efficiencies of 23.6–42.2% and 26.7–48.6%, respectively. The chloride removal was always greater at increasing depths, due to the fact that, in the nearer surface, chlorides were quite present still in the process of diluting in the electrolyte media. As expected, free chlorides were removed at considerably high percentages for all cases, and lithium borate showed a considerable better performance, accounting to percentage removal efficiency up to 98.8%. The concentration of bound chlorides was overall reduced by the electrochemical treatment, which challenges the hypothesis that all types of bound chlorides would be immobile under electric charge. The reduction of bound chlorides after the electrochemical treatment was hypothetically attributed to either a release of adsorbed chlorides by changes of physical factors or strong electromigration force or decomposition of Friedel's salt due to acidification of pore solution.

(2) Concerning the mass loss, corrosion potential, and corrosion rate readings, it can be said that ECE

applied temporarily to the corroded concrete structure might be effective in only reducing the corrosion degree as the potential increased from nearly −700 to −600 mV vs. SCE for all cases to −293, −315, and −350 mV vs. SCE for Ca(OH)$_2$, water, and lithium borate, respectively, pointing to calcium hydroxide as a better option when considering repassivation after treatment and consequent protection against further corrosion. In order to minimize the doubts about repassivation, a quantitative technique was also used to ensure the corrosion state after ECE and measure the corrosion rate by linear polarization. Results shown pointed that the corrosion rate was significantly reduced by the electrochemical treatment. Before treatment, values arose to around 500 to 1000 μA/cm^2, and by the end of treatment, values were reduced to 23, 286, and 107 μA/cm^2 for Ca(OH)$_2$, water, and lithium borate, respectively, again pointing to Ca(OH)$_2$ as the most efficient. Mass loss results and visual inspection confirmed the same statements.

(3) The partial repassivation in terms of the corrosion rate and half-cell potential can be explained due to the removal of chlorides and the migration of alkaline ions from the electrolyte to vicinity of the steel bar, on a process of electrodeposition. A supporting clause for this hypothesis is that, by measuring the pH of electrolyte solutions, for calcium hydroxide, the pH decrease was smaller and there was a significant increase on the voltage of the circuit, meaning an increase of concrete resistance. This shows that the pH fall may be additionally attributed to a migration of alkaline ions from the electrolyte solution to the concrete pore structure. By filling up pores and consequently some possible cracks caused by the corrosion process, a partial recovery on the repassivation of rebars could be achieved. Moreover, the same factor can explain a lower performance of calcium hydroxide on chloride removal, because during the electrochemical chloride removal process, the current applied probably induces the precipitation of Ca(OH)$_2$ ions on pores of the cement matrix, blocking the network and reducing the mobility of chlorides ions, when compared with that of other electrolytes.

(4) Considering different electrolytes, lithium borate appeared to be the most efficient to extract chlorides from concrete while calcium hydroxide has better performance on restoring the passive state after corrosion, healing the structure at another level, filling up possible cracks as well. Therefore, in summary, depending on the main goal of the treatment, different electrolytes will show better performances, which also make it important to consider the pretreatment evaluation to see in which stage of corrosion damage is the structure. This also highlights the need of better specifications on standards and guidelines about the treatment setup.

Data Availability

The data used to support the findings of this study are included within the article.

Conflicts of Interest

The authors declare no conflicts of interest.

Acknowledgments

References

[1] B. Elsener and U. Angst, "Mechanism of electrochemical chloride removal," *Corrosion Science*, vol. 49, no. 12, pp. 4504–4522, 2007.

[2] B. Elsener, M. Molina, and H. Böhni, "The electrochemical removal of chlorides from reinforced concrete," *Corrosion Science*, vol. 35, no. 5–8, pp. 1563–1570, 1993.

[3] J. Meitz, *Electrochemical Rehabilitation Methods for Reinforced Concrete Structures: A State of the Art Report*, The Institute of Materials Minerals and Mining, London, UK, 1998.

[4] U. M. Angst, M. R. Geiker, A. Michel et al., "The steel–concrete interface," *Materials and Structures*, vol. 50, no. 2, p. 143, 2017.

[5] N. M. Ihekwaba, B. B. Hope, and C. M. Hansson, "Carbonation and electrochemical chloride extraction from concrete," *Cement and Concrete Research*, vol. 26, no. 7, pp. 1095–1107, 1996.

[6] T. D. Marcotte, C. M. Hansson, and B. B. Hope, "The effect of the electrochemical chloride extraction treatment on steel-reinforced mortar part II: microstructural characterization," *Cement and Concrete Research*, vol. 29, no. 10, pp. 1561–1568, 1999.

[7] C. Arya, Q. Sa'id-Shawqi, and P. R. W. Vassie, "Factors influencing electrochemical removal of chloride from concrete," *Cement and Concrete Research*, vol. 26, no. 6, pp. 851–860, 1996.

[8] N. M. Ihekwaba, B. B. Hope, and C. M. Hansson, "Pull-out and bond degradation of steel rebars in ECE concrete," *Cement and Concrete Research*, vol. 26, no. 2, pp. 267–282, 1996.

[9] N. R. Buenfeld and J. P. Broomfield, "Influence of electrochemical chloride extraction on the bond between steel and concrete," *Magazine of Concrete Research*, vol. 52, no. 2, pp. 79–91, 2000.

[10] E. Otero, J. A. González, A. Cobo, and M. N. González, "Electrochemical chloride removal from reinforced concrete structures and its ability to repassivate prerusted steel surfaces," *Materials and Corrosion*, vol. 52, no. 8, pp. 581–589, 2001.

[11] S. R. Sharp, G. G. Clemena, V. P. Virmani, G. E. Stoner, and R. G. Kelly, "Electrochemical chloride extraction: influence of concrete surface on treatment," Report no. FHWA-RD-02-107, Diane Publishing Company, Darby, PA, USA, 2002.

[12] R. B. Polder, "Laboratory investigation of electrochemical chloride extraction from concrete with penetrated chloride," *Heron*, vol. 47, 2002.

[13] J. C. Orellan, G. Escadeillas, and G. Arliguie, "Electrochemical chloride extraction: efficiency and side effects," *Cement and Concrete Research*, vol. 34, no. 2, pp. 227–234, 2004.

[14] A. Hosseini and A. R. Khalou, "Study of electrochemical chloride extraction as a non-destructive repair method: part I. Discrete test samples," *Asian Journal of Civil Engineering (Building and Housing)*, vol. 6, pp. 167–182, 2005.

[15] M. J. Sanchez, P. Garces, and M. A. Climent, "Electrochemical extraction of chlorides from reinforced concrete: variables affecting treatment efficiency," *Materials de Construccion*, vol. 56, pp. 17–26, 2006.

[16] J. M. Miranda, J. A. González, A. Cobo, and E. Otero, "Several questions about electrochemical rehabilitation methods for reinforced concrete structures," *Corrosion Science*, vol. 48, no. 8, pp. 2172–2188, 2006.

[17] Y. Tissier, V. Bouteiller, E. Marie-Victoire, S. Joiret, T. Chaussadent, and Y. Tong, "Electrochemical chloride extraction to repair combined carbonated and chloride contaminated reinforced concrete," *Electrochimica Acta*, vol. 317, pp. 486–493, 2019.

[18] H. Lin and Y. Li, "A study on the deterioration of interfacial bonding properties of chloride-contaminated reinforced concrete after electrochemical chloride extraction treatment," *Construction and Building Materials*, vol. 197, pp. 228–240, 2019.

[19] C. C. Chang, W. Yeih, J. J. Chang, and R. Huang, "Effects of stirrups on electrochemical chloride removal efficiency," *Construction and Building Materials*, vol. 68, pp. 692–700, 2014.

[20] I. Martinez, F. Rozas, S. Ramos-Cillan, M. González, and M. Castellote, "Chloride Electroremediation in reinforced structures: preliminary electrochemical tests to detect the steel repassivation during the treatment," *Electrochimica Acta*, vol. 181, pp. 288–300, 2015.

[21] I. Martínez, M. González, F. Rozas, and M. Castellote, "New non-destructive passivity indicators for the control of electrochemical chloride extraction in concrete," in *Proceedings of the CORROSION 2014*, San Antonio, TX, USA, March 2014.

[22] M. Sánchez and M. C. Alonso, "Electrochemical chloride removal in reinforced concrete structures: improvement of effectiveness by simultaneous migration of calcium nitrite," *Construction and Building Materials*, vol. 25, no. 2, pp. 873–878, 2011.

[23] A. Pérez, M. A. Climent, and P. Garcés, "Electrochemical extraction of chlorides from reinforced concrete using a conductive cement paste as the anode," *Corrosion Science*, vol. 52, no. 5, pp. 1576–1581, 2010.

[24] A. Cañón, P. Garcés, M. A. Climent, J. Carmona, and E. Zornoza, "Feasibility of electrochemical chloride extraction from structural reinforced concrete using a sprayed conductive graphite powder-cement paste as anode," *Corrosion Science*, vol. 77, pp. 128–134, 2013.

[25] K. B. Kim, J. P. Hwang, and K. Y. Ann, "Influence of cementitious binder on chloride removal under electrochemical treatment in concrete," *Construction and Building Materials*, vol. 104, pp. 191–197, 2016.

[26] J. Xia, Q.-f. Liu, J.-h. Mao et al., "Effect of environmental temperature on efficiency of electrochemical chloride removal from concrete," *Construction and Building Materials*, vol. 193, pp. 189–195, 2018.

[27] J. Xia, X. Cheng, Q.-f. Liu et al., "Effect of the stirrup on the transport of chloride ions during electrochemical chloride removal in concrete structures," *Construction and Building Materials*, vol. 250, Article ID 118898, 2020.

[28] W. Yeih, J. J. Chang, C. C. Chang, K. L. Chen, and M. C. Chi, "Electrochemical chloride removal for reinforced concrete with steel rebar cage using auxiliary electrodes," *Cement and Concrete Composites*, vol. 74, pp. 136–146, 2016.

[29] W. Sun, "Study on the influence of chloride ions content on the sea sand concrete performance," *American Journal of Civil Engineering*, vol. 4, no. 2, pp. 50–54, 2016.

[30] H. W. Song, M. S. Jung, C. H. Lee, S. H. Kim, and K. Y. Ann, "Influence of chemistry of chloride ions in cement matrix on corrosion of steel," *ACI Materials Journal*, vol. 107, pp. 332–339, 2010.

[31] G. K. Glass, A. M. Hassanein, and N. R. Buenfeld, "Cathodic protection afforded by an intermittent current applied to reinforced concrete," *Corrosion Science*, vol. 43, no. 6, pp. 1111–1131, 2001.

[32] J. Bennett and T. J. Schue, *Chloride Removal Implementation Guide, SHRP-S-347*, National Research Council, Washington, DC, USA, 1993.

[33] DD CEN/TS 14038-2, *Electrochemical Realkalisation and Chloride Extraction Treatments for Reinforced Concrete Part2: Chloride Extraction*, AFNOR, Paris, France, 2011.

[34] J. Bennett and T. J. Schue, *Evaluation of Norcure Process for Electrochemical Chloride Removal from Steel-Reinforced Concrete Bridge Components (No. Shrp-C-620)*, 1993.

[35] H. H. Uhlig and C. V. King, "Corrosion and corrosion control," *Journal of the Electrochemical Society*, vol. 119, no. 12, p. 327C, 1972.

[36] J. A. González and C. Andrade, "Effect of carbonation, chlorides and relative ambient humidity on the corrosion of galvanized rebars embedded in concrete," *British Corrosion Journal*, vol. 17, no. 1, pp. 21–28, 1982.

[37] B. Elsener, "Half-cell potential mapping to assess repair work on RC structures," *Construction and Building Materials*, vol. 15, no. 2-3, pp. 133–139, 2001.

[38] T. Y. Hao, "Study on the variation of electric potential in reinforced concrete members during accelerated corrosion and electrochemical chloride extraction process," *IOP Conference Series: Materials Science and Engineering*, IOP Publishing, vol. 479, no. 1, Bristol, UK, 2019.

[39] K. Y. Ann, *Enhancing the chloride threshold level for steel corrosion in concrete*, Ph.D. thesis, University of London, London, UK, 2005.

[40] H. W. Song, C. H. Lee, M. S. Jung, and K. Y. Ann, "Development of chloride binding capacity in cement pastes and influence of the pH of hydration products," *Canadian Journal of Civil Engineering*, vol. 35, no. 12, pp. 1427–1434, 2008.

[41] G. K. Glass, B. Reddy, and N. R. Buenfeld, "The participation of bound chloride in passive film breakdown on steel in concrete," *Corrosion Science*, vol. 42, no. 11, pp. 2013–2021, 2000.

[42] C. Arya, N. R. Buenfeld, and J. B. Newman, "Assessment of simple methods of determining the free chloride ion content of cement paste," *Cement and Concrete Research*, vol. 17, no. 6, pp. 907–918, 1987.

[43] J. S. Ryou and K. Y. Ann, "Variation in the chloride threshold level for steel corrosion in concrete arising from different chloride sources," *Magazine of Concrete Research*, vol. 60, no. 3, pp. 177–187, 2008.

[44] J. S. Ann and P. Monteiro, "Electrodeposition as a rehabilitation method for concrete materials," *Canadian Journal of Civil Engineering*, vol. 31, no. 5, pp. 776–781, 2004.

Research Article

The Mechanism of the First Hydration-Dehydration Cycle of Pure α- and β-CaSO₄·0.5H₂O

E. Abu Zeitoun [ID],[1] C. Pritzel,[1] Y. Sakalli,[2] and R. Trettin[1]

[1]*Institute of Building and Materials Chemistry, University of Siegen, Paul-Bonatz-Str. 9-11, Siegen, Germany*
[2]*Micro- and Nanoanalytics Facility, University of Siegen, Paul-Bonatz-Str. 9-11, Siegen, Germany*

Correspondence should be addressed to E. Abu Zeitoun; abuzeitoun@chemie.uni-siegen.de

The objective of this research was to understand the dehydration mechanism of technical dihydrate and the variation of the physical properties of β-hemihydrate after the first hydration-dehydration process. In this study, the recycling mechanism of different hemihydrate types as raw material was investigated. The influence of the first hydration-dehydration process on the hydration rate, microstructure, and mechanical properties of recycled hemihydrate were characterized by differential calorimetric analysis (DCA), calcium ion-selective electrode (Ca^{2+}-ISE), conductivity, particle size distribution (PSD), scanning electron microscopy (SEM), and X-ray diffraction (XRD). The results showed that the formed hemihydrate after the first hydration-dehydration process differs in its properties than the unrecycled hemihydrate in some characteristics such as the morphological structure, number of surface, and side defects due to the grinding process after the first hydration step. In addition to the grinding step, the calcination process was responsible for increasing the number of defects on the crystal surface, which leads to a change in setting time and the microstructure of the recycled hemihydrate. Therefore, after the 1st reaction cycle of β-HH, the compressive strength decreases due to a decrease in the hemihydrate crystal size, an increase in the surface area, and an increase in the amount of water required to perform the hydration reaction. The obtained hemihydrate after the first hydration-dehydration process was in β form due to the applied calcination process after the first cycle.

1. Introduction

Calcium sulfate hemihydrate plaster is considered one of the most popular sustainable binders used in the construction industry due to low production energy, low market price, fire-resistant, and good thermal properties [1–5]. It is commonly used as an ingredient in paste and mortar plastering and production of some building components such as plasterboards and building blocks. Moreover, it can be used as an additive in polymers, cement, and food industries [1, 3, 6–11]. The annual production of calcium sulfate-based binders is more than 260 million tons worldwide, of that, over 80 million tons are applied in the production of gypsum plasterboards. The obtained gypsum can be founded either naturally or industrially as a byproduct [12–14]. The flue gas desulfurization process (FGD) delivers over one-half of this binder to the industrial

sectors [15, 16]. However, this source will not exist in the future due to the need for energy conservation and sustainable methods of production. Therefore, it is useful to recycle gypsum waste and consider the recycled material as an alternative resource to be used in cement, building, and ceramic industries [3–5, 11, 17–19]. The construction and demolition (CD) processes are considered as one of the largest contributors to waste in the world. Moreover, the obtained gypsum plaster waste from construction and demolition processes accumulates to 15 million tons annually [4, 20, 21]. One of the common destinations for these wastes is landfilling. However, it is feasible to develop a new technology to reuse these wastes in further applications due to limited space and contaminating groundwater sources in addition to the environmental regulation of some countries. It has been reported that gypsum plasterboard wastes can be recycled in a sequential process by crushing, separating, and

burning to transform the dihydrate into the hemihydrate phase [17]. According to their report, it is useful as geomaterial or ground improvement material due to its effectiveness in many engineering and economic aspects [17]. The conversion of gypsum into a recycled product has been interesting for many researchers due to its reaction reversibility, cycle-ability, stability, environmental safety, nontoxicity, and sustainability [4, 11, 18, 19, 22]. In this study, the pure β- and SA α-HH were recycled one time by applying similar calcination conditions in an attempt to understand the dehydration mechanism in detail. Furthermore, the changes in physiochemical properties of the newly generated hemihydrate were studied.

1.1. Experimental Procedure. In the first step, the cycling process was defined by hydration-dehydration process and considered as the first reaction cycle, because alpha- and beta hemihydrate were the starting material in the cycling process. The chemical composition of alpha hemihydrate (α-HH) from the steam autoclave process and beta hemihydrate (β-HH) were determined by XRD as shown in Table 1. In more detail, hemihydrate was added to water to perform the hydration reaction to obtain dihydrate, and then, the formed dihydrate was crushed and calcinated back to beta hemihydrate. The stoichiometric amount of water needed for hydration is around 15.7 ml per 100 g, but an excess amount of water is required to obtain gypsum slurry with good workability. Therefore, the rheological test is very important to determine the water to solid (w/s) ratio for any hemihydrate type individually since it is a function of particle size [22, 23]. Figure 1 represents the cycling mechanism of gypsum, starting from hemihydrate. In the first stage, the hydration reaction will take place immediately after hemihydrate addition to water. The hydration time varies depending on the physical properties of the hemihydrate used in this process. After the hydration is completed, the excess amount of water needs to be evaporated to achieve the mechanical strength of the dihydrate crystals. In the second stage, the calcination of the formed dihydrate crystals was performed at 140°C for at least 4 hours to ensure the complete dehydration of dihydrate.

Deionized water was used for all liquid phases. For the rheological test, 100 g of hemihydrate was added to water and mixed for 1 minute. The mix was filled into a hollow cylinder (inner diameter 30 mm and height 50 mm), which was placed on a glass plate, and then the cylinder was pulled up vertically. The glass plate was removed up and down five times by rotating a special handle attached to the stage clockwise in order to disperse the collapsed mix. The average of three perpendicular diameters of the dispersed slurry was defined as slump flow. The reaction kinetic was performed by differential calorimetric analysis (DCA) (Toni Technik Baustoffprüfsysteme GmbH-Germany) using (1 : 1) water to solid ratio. The measurement time and temperature were fixed at 24 hours and 25°C, respectively. From this measurement, the heat rate during the hydration was monitored, as well as the total heat released [24]. The calcium concentration was carried out by Ca-ion-selective electrode (ISE) (Mettler-Toledo GmbH-Germany). The samples were prepared according to gypsum solubility. Prior to each measurement, the Ca^{2+}-ISE was calibrated to ensure the electrode efficiency. Both electrodes (Ca^{2+}-ISE and conductivity electrode) were immersed in 200 ml deionized water to record the blank value before the addition of 3.2 g of hemihydrate. The changes in calcium concentration and reaction conductivity were recorded every 30 seconds for four hours at 20°C [25]. Particle size distribution was detected by Mastersizer 2000, Malvern Instruments GmbH-Germany. Before starting the measurement, the sample chamber was rinsed and filled with isopropanol; then, a small amount of the powdered sample was added to the sample chamber at a stirring speed of 2000 rpm to ensure sample delivery to the measuring cell. The amount of sample was controlled by the so-called obscuration range of the laser beam, which should lie between 10 and 20% according to the user manual of the instrument [26]. The specific surface area of powder was determined by the physical adsorption of a gas on the surface of the solid using the BET method (Micromeritics ASAP2020 (Micromeritics GmbH)) [27, 28]. Both quantitative and qualitative analyses of hemihydrate samples were measured using XRD. Rietveld refinement was used to analyze the samples quantitatively. The powder samples were filled in the XRD sample holders and transferred to the instrument; then the XRD pattern was taken using a Panalytical $x'pert\ pro$ diffractometer with a Cu Kα source operated at 40 kV and 40 mA. The range of 2θ was between 8° and 40° [29]. The morphology of the formed crystals was recorded by scanning electron microscopy (Quanta 250 FEG, FEI GmbH-Germany). To perform the measurement, the sample has to be glued on the sample holder of the SEM using either a carbon conductive tab or silver paint. Samples were prepared without pretreatment and results with high resolution were obtained [30]. To monitor the dehydration of the generated dihydrate before and after the first reaction cycle, a Simultaneous Thermal Analysis (STA) method was utilized (STA 449 Netzsch GmbH-Germany) at N_2 atmosphere with a gas flow of 20 ml/min. This device consists of the thermal gravimetry (TG) and differential scanning calorimetry (DSC) apparatus fused into one system with the sole purpose of obtaining vital information from the thermal events recorded in the investigation of the sample over time [6]. The time of dehydration can be determined with this method as well as the mass loss caused by dehydration at certain temperatures. To measure the water release of dihydrate, a small amount of dihydrate powder was placed in a platinum crucible and heated in the STA at 10 K/min.

2. Results and Discussion

In the beginning, the first reaction cycle starts with hemihydrate; therefore, this step is called the hydration-dehydration process. The impact of this process on hydration kinetic and calcium concentration changes was measured. Figure 2(a) shows the comparison in the heat rate between the pure β-HH and the same hemihydrate after the 1st reaction cycle. The heat rate of the recycled β-HH is slower

$CaSO_4 \cdot 0.5H_2O(S)$ — Hydration mechanism → $CaSO_4 \cdot 2H_2O(S)$

1st reaction cycle

β-Process

In dry conditions at temperature ranges between 110 and 140°C

$CaSO_4 \cdot 2H_2O(S)$ — Dehydration mechanism → $CaSO_4 \cdot 0.5H_2O(S)$

Autoclave or hydrothermal methods under certain temperature and pressure
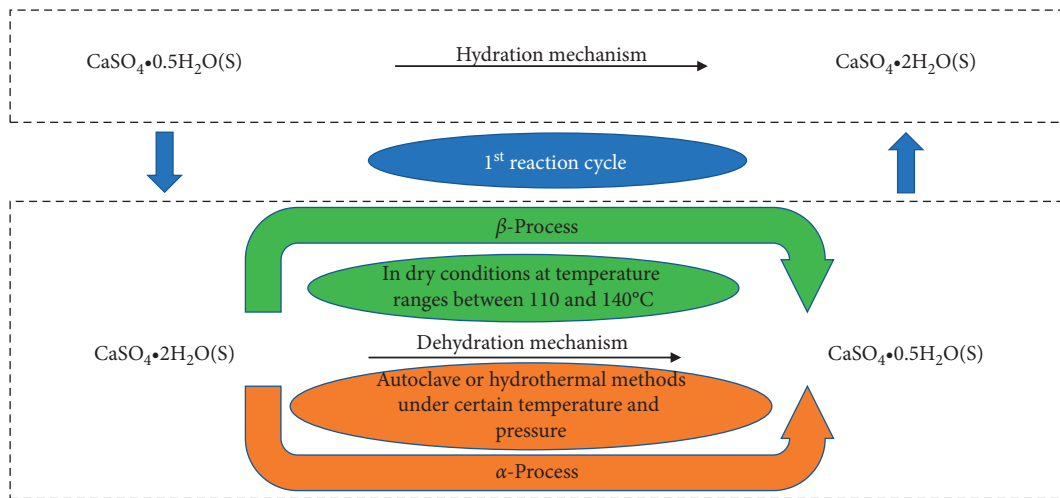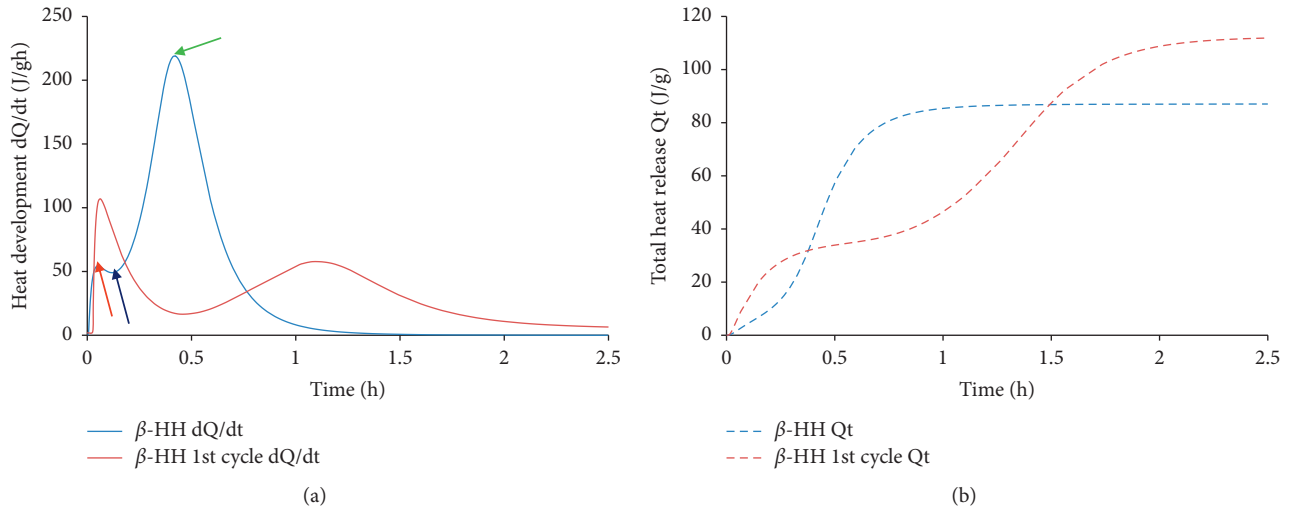
α-Process

FIGURE 1: The mechanism of the 1st reaction cycle [17, 31].

(a)

(b)

FIGURE 2: (a) Heat evolution curves and (b) total heat release of pure β-HH β-HH after 1st cycle.

than the pure β-HH due to the agglomeration of the hemihydrate particle which might hinder the solving of hemihydrate. In addition to the heat development changes, the total heat release in J/g was also measured during the recycling of β-HH, as shown in Figure 2(b). To verify that, the calcium ion concentration changes were measured during the hydration process.

The hydration reaction of β-HH before and after the 1st reaction cycle can be divided into four steps, as shown from the heat development curve in Figure 2(a). The first peak represents two hydration steps; in the first step, the hemihydrate becomes humidified, and a water film will be generated around the particles. This is followed by the solving process of the hemihydrate which should be exothermal because the solubility of hemihydrate has an inverse relation with temperature [12, 32, 33]. This results in the initial increase in heat development. The variation between pure β-HH and β-HH after the 1st reaction cycle in the first peak of the heat development was due to the presence of

finer HH particle of the recycled material, as shown from d_{10} and d_{50} in Table 2. Through the rapid solving of hemihydrate, the ions concentration increases rapidly until they reach the start supersaturation denoted in Figure 2(a) with the red arrow. In the next step, after reaching the supersaturation, the hydration energy decreases up to the point indicated by the blue arrow because of seed crystal formation. During this time period, both processes (solving and seeds formation) takes place. The amount and rate of seeds formation depend highly on the ion concentration generated from the solving process. It is very important to note that the supersaturation is the driving force behind seeds formation. Moreover, the higher the ion concentration in the reaction solution, the more seeds are generated [34, 35].

The second peak of the heat development curve also represents two hydration reaction steps. In the beginning, the reaction energy increases again due to the continuous solving of the hemihydrate without the formation of new seeds. In the period which lies between the blue and green

arrows, only solving the remaining hemihydrate, in addition to the growing of the created seeds from the previous step, takes place. In the last step, which is the retardation period, most of the hemihydrate is consumed and the solving process delivers insufficient ions for the dihydrate crystals to be grown. At this point, when the ions concentration is around the solubility of dihydrate, then hydration stops [12]. The purity of hemihydrate, as well as the milling process, plays an important role during its hydration. The existence of any dihydrate crystals changes the whole hydration process. Therefore, the purity of hemihydrate before and after the 1st reaction cycle was analyzed quantitatively using XRD as illustrated in Table 1.

As shown in Figure 3, a similar behavior as the heat rate development was observed. In the beginning, the solving of β-HH after the first cycle was similar to the uncycled β-HH, and then the dissolution rate varies due to the agglomeration that is generated from the hydration-dehydration process. The previous investigation of the pure β-HH displayed that the surface area and the numbers of defects were responsible for the hydration rate neglecting the effect of agglomeration. Hence, when the agglomeration of the particles increases, the hydration rate will be affected, as shown from the DCA and Ca^{2+}-ISE results in Figure 3. In order to explain that in detail, surface area and particle size distribution measurements were carried out. After the reaction cycle, two maxima of the particle size distribution were observed, as shown in Figure 4. This represents the formation of fine crystal d_{10} and d_{50} values in addition to an agglomeration of these crystals together with d_{90} value. As illustrated in Figure 3, at the beginning of the hydration, the ion delivery rate of the recycled β-HH was higher than the pure β-HH due to the generation of finer hemihydrate crystals after the 1st reaction cycle as presented form d_{10} and d_{50} values in Table 2 since the finer the particle size, the higher the rate of ion delivery. Therefore, the maximum supersaturation and conductivity of the recycled β-HH are higher than the pure β-HH, as shown in Figure 3. After a while, once the whole recycled β-HH fine crystals are dissolved, the hydration rate was retarded in comparison to the pure hemihydrate, as shown from DCA, Ca^{2+}-ISE, and conductivity measurements due to the agglomeration that is generated from the hydration-dehydration process as shown in Figure 4.

Table 2 summarizes the particle size distribution with surface area changes. The surface area increases after the first reaction cycle, and this implies that the size of the crystal decreases, as shown from d_{10} and d_{50} values. Figure 5 represents the SEM images of the pure β-HH and β-HH after the 1st cycle before and after four hours of hydration.

The crystal morphology differences between the pure β-HH and β-HH after the first cycle before hydration represent the generation of a fine hemihydrate crystal with agglomeration. After four hours of in situ hydration, SEM images were taken to view the morphology of the dihydrate crystals. As shown in Figure 5, the formed dihydrate crystals after the first cycle have the same crystal morphology as the formed dihydrate crystal from the pure hemihydrate before cycling. The differences in the physical properties, as shown from Table 2, have a large effect on the required amount of

water which is needed to achieve good workability as well as the mechanical properties. The w/s ratio was determined according to a certain slump flow in the range of 82–85 mm.

The changes in crystal morphology and particle size lead to a variation in the mechanical properties. Therefore, the compressive strength for the pure β-HH and β-HH after one cycle was measured and calculated, as shown in Figure 6. The drop in the compressive strength after the first reaction cycle was due to the significant increase in the w/s ratio from 0.8 to 1 and the changes in the microstructure.

Regarding this change in the compressive strength, both pore radius and the microstructure development were measured by Mercury porosimetry and SEM, respectively. The pore radius size increases from 0.76 to 1.97 μm. Furthermore, the voids between the dihydrate crystals after one cycle increase, as shown in Figure 7. Hence, the formed β-HH after the first hydration-dehydration process differs in its properties than the unrecycled β-HH due to the grinding process after the first hydration step. So, the grinding step beside the dehydration process of the recycled material decreases the particle size, increases the surface area, and changes the microstructure. The finer the particle size, the higher the amount of required water to perform better workability leading to a decrease in the compressive strength of the recycled hemihydrate. In addition, the grinding step increases the number of defects on the crystal surface, which leads to a change in the set time and the microstructure of the recycled hemihydrate. The only way to get a hemihydrate slurry with the needed workability is the usage of a superplasticizers, but those additives are influencing the hydration behavior of the hemihydrate and the morphology of the formed dihydrate crystals [36, 37]. That was the reason to keep the workability constant by adding more water. With a constant amount of water, mixing of the hemihydrate slurry was impossible.

From the XRD results obtained, the phase composition of both types of hemihydrates has no significant changes after the 1st reaction cycle, as shown in Table 1. This indicates that the hemihydrate was well dehydrated at 140°C as no dihydrate phase was discovered. The impurities which were presented before cycling remain unchanged. Commonly known impurities in gypsum are usually in the form of carbonates, silica, or soluble salts. These impurities varied depending on the mine source of gypsum [12, 13, 38].

The same hydration-dehydration process was applied to the SA α-HH. After the hydration of SA α-HH, the obtained dihydrate was calcined in a dry atmosphere at 140°C for four hours. Therefore, the obtained hemihydrate after the first hydration-dehydration process was in β form. Different properties, such as the particle size, specific surface area, and w/s ratio, were evaluated as shown in Table 3. The applied calcination condition on the obtained dihydrate was mainly responsible for the variation in the physical properties between the SA α-HH and the HH after the 1st reaction cycle.

The rate of change of calcium concentration and ion conductivity over time for SA α-HH and SA α-HH after the first cycle was recorded. As shown in Figure 8, the calcium ion concentration rate for SA α-HH after one cycle became faster than the uncycled sample. The ion conductivity

TABLE 1: Chemical composition of pure β-HH and SA α-HH before and after the first cycle.

Chemical composition (%)	Quartz	Anhydrite II	Hemihydrate	Dihydrate	Syngenite	Calcite
β-HH	0.3	2.1	94.3	1.8	0.2	1.3
β-HH-1st cycle	0.5	3.4	94.6	0.0	0.2	1.3
SA α-HH	0.6	0.7	97.3	0.0	0.3	1.0
SA α-HH 1st cycle	1.0	1.1	96.1	0.1	0.3	1.3

(a)

(b)
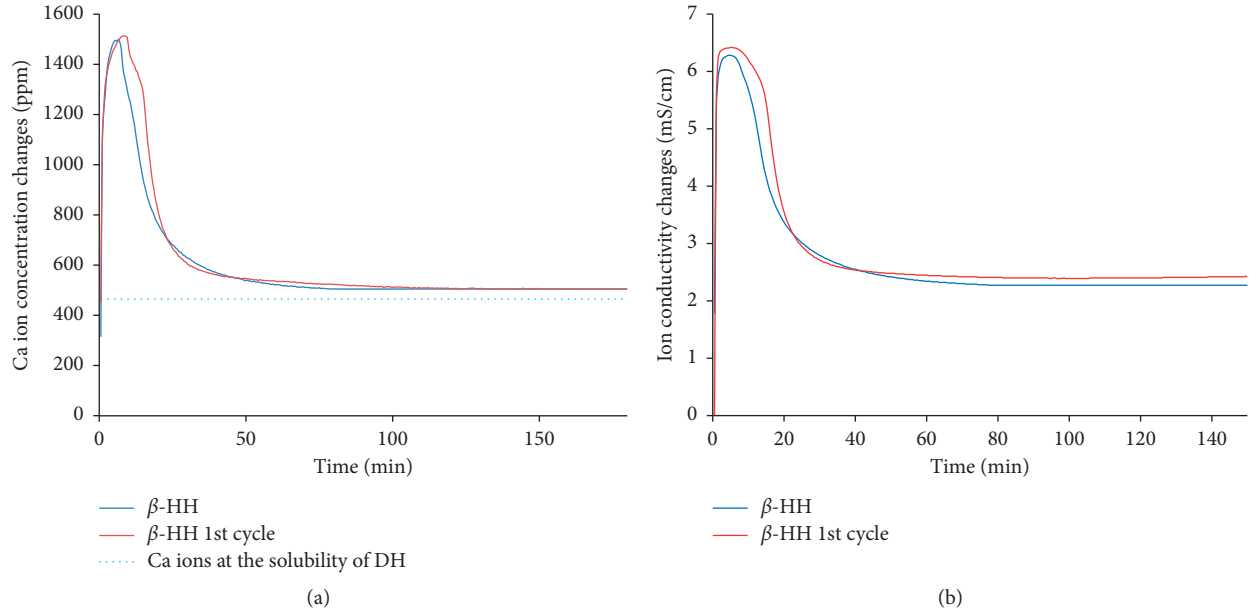
FIGURE 3: Ca^{2+}-Ion concentration and ion conductivity changes for pure β-HH and β-HH after the first cycle: (a) ion concentration changes and (b) ion conductivity changes.
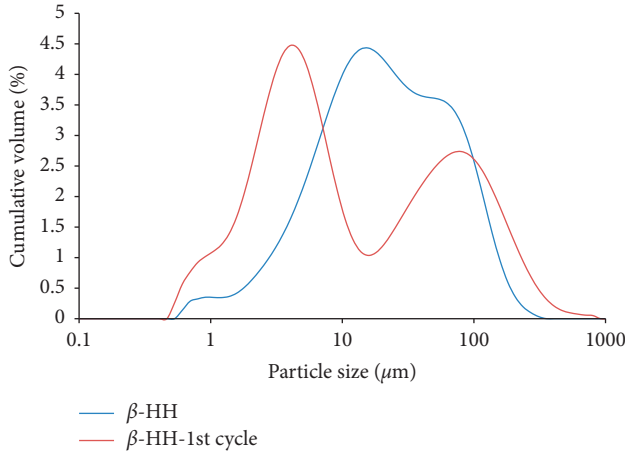
FIGURE 4: Particle size distribution of pure β-HH and β-HH after the first cycle.

changes maintain similar behavior like calcium ion changes. The main reason for such changes was the grinding process in addition to the applied calcination condition after the hydration-dehydration process of the SA α-HH. The original SA α-HH has large particles with nearly a smaller number of defects on its crystal surfaces, but due to the grinding process, the crystal size decreases, and the number of defect

positions on the outer surface of each crystal increases. The particle size distribution becomes smaller during the recycling processes with less agglomeration compared to the pure SA α-HH, as shown in Figure 9. Therefore, the surface area and the hydration rate of SA α-HH were significantly increased. The pure SA α-HH has a slower heat rate changes than its recycled sample because of the large difference between the sample before and after cycling since the generated hemihydrate is in a β form not in α form due to the applied calcination condition during the first recycling step.

The recycled β-HH had shown retardation in its rate of calcium ion concentration and ion conductivity changes in contrast to the unrecycled β-HH, whereas the generated hemihydrate after the first hydration-dehydration process of SA α-HH had shown a rapid change in its rate of calcium ion concentration and ion conductivity as illustrated in Figure 8. The reason is due to differences in the crystal morphology between the started hemihydrate types and the impact of recycling and grinding processes on the crystal surfaces.

The generated dihydrates before and after the 1st hydration cycle have been analyzed qualitatively using the XRD, as shown in Figure 10. The calcium sulfate dihydrate phase was the major component found in the diffractograms of all generated samples after hydration, as displayed in Figure 10. This indicates that the samples were well hydrated as no hemihydrate or anhydrite phases were discovered.

TABLE 2: Physical properties of pure β-HH and β-HH after the first cycle.

Sample name	d_{10} (μm)	d_{50} (μm)	d_{90} (μm)	BET surface area (m^2/g)	W/S ratio
β-HH	4.48	20.98	94.70	10.29	0.8
β-HH-1st cycle	1.80	8.18	135.90	11.86	1

(a)

(b)

(c)

(d)
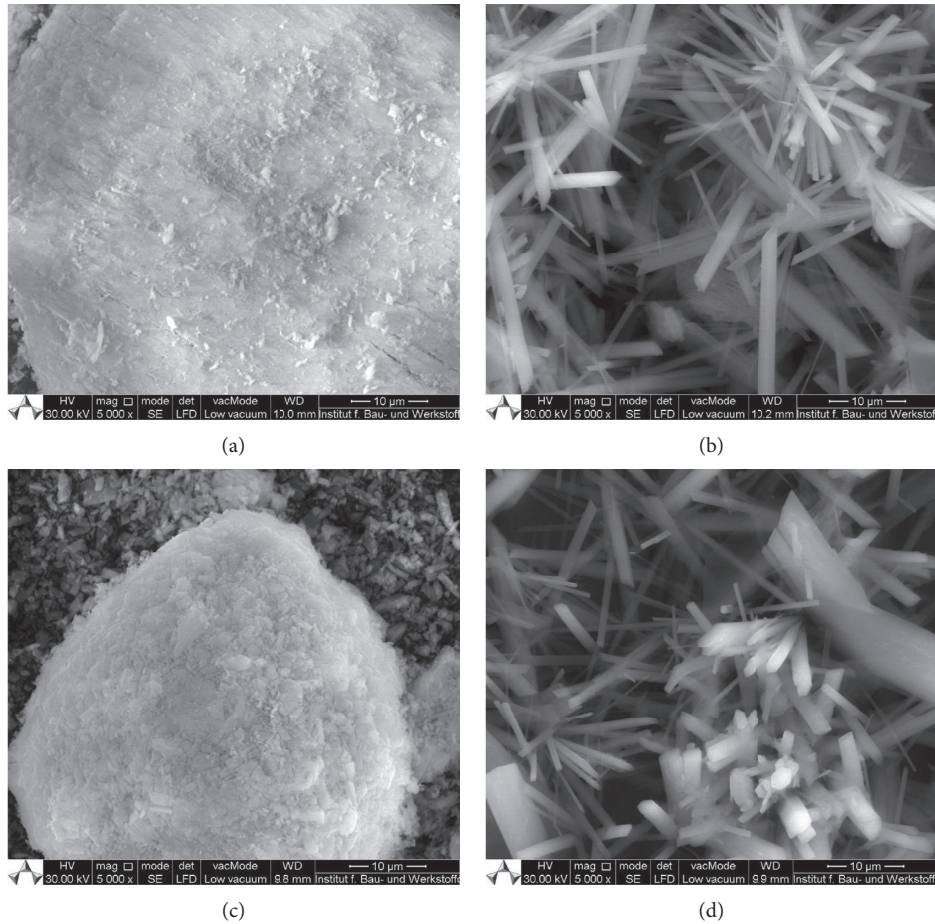
FIGURE 5: SEM images pure β-HH and β-HH after the first cycle before and after hydration: (a, b) pure β-HH before and after hydration, respectively, and (c, d) β-HH after the first cycle before and after hydration, respectively.
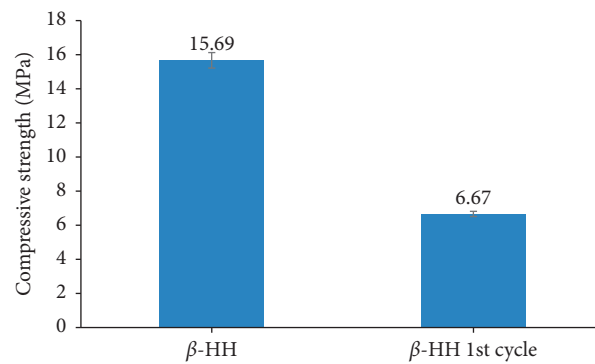
FIGURE 6: The compressive strength of the β-HH and β-HH after the first cycle.

(a)

(b)
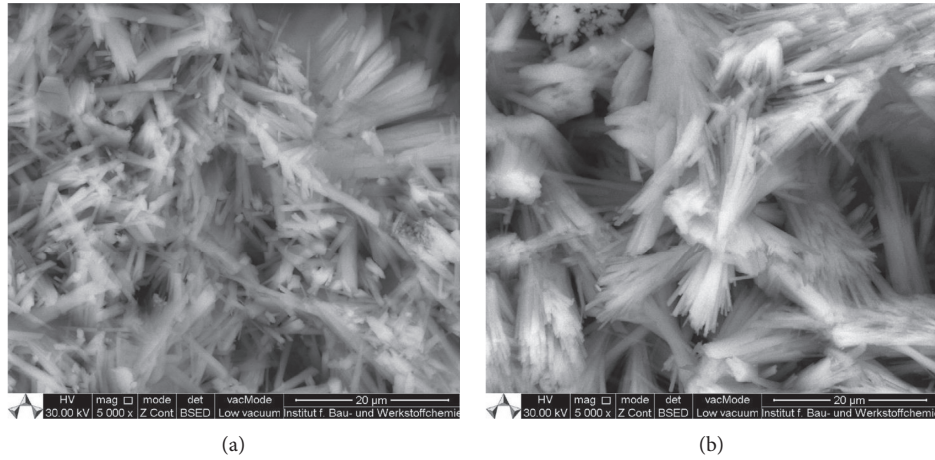
FIGURE 7: SEM images for dihydrate crystals formation from β-HH and β-HH after the first cycle.

TABLE 3: Physical properties of pure SA α-HH and SA α-HH after the first cycle.

Sample name	d_{10} (μm)	d_{50} (μm)	d_{90} (μm)	BET surface area (m^2/g)	W/S ratio
SA α-HH	6.30	70.88	192.30	1.28	0.35
SA α-HH 1st cycle	2.12	19.79	270.36	7.06	0.90

(a)

(b)
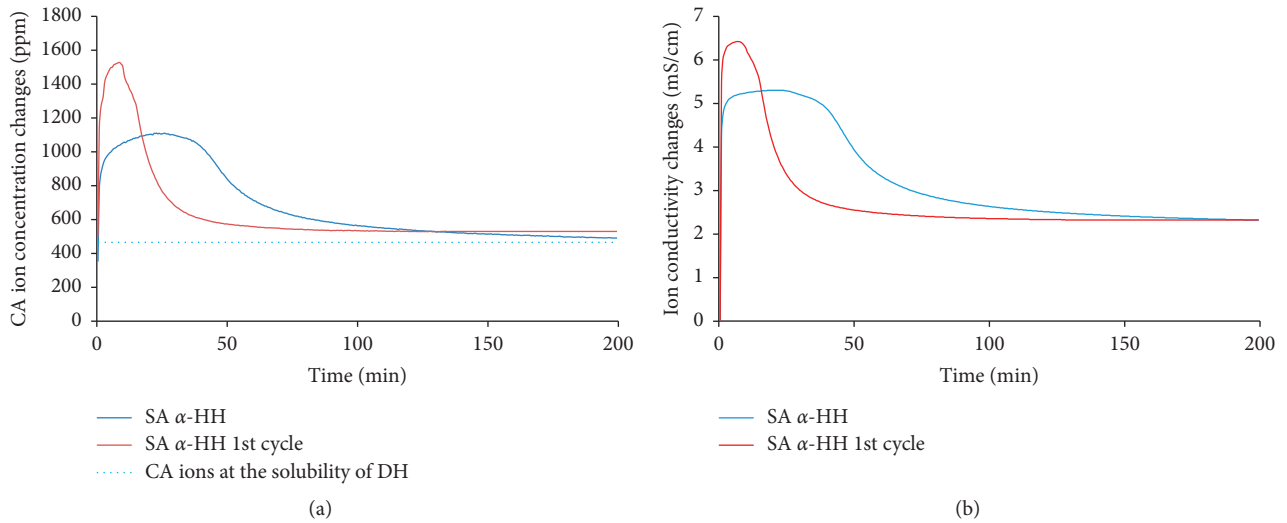
FIGURE 8: Ca^{2+}-Ion concentration and ion conductivity changes for pure SA α-HH and SA α-HH after the first cycle: (a) ion concentration changes and (b) ion conductivity changes.

However, the intensity of the peaks differs slightly in length and positions. A similar result was obtained in the investigations by Rabizadeh et al. [39]. The DSC signals of the generated dihydrate indicate the phase transformation from dihydrate to soluble anhydrite through a two-step dehydration process of $CaSO_4 \cdot 2H_2O \longrightarrow CaSO_4 \cdot 0.5H_2O \longrightarrow \gamma CaSO_4$ as displayed in Figure 11 [6]. Moreover, the TG curves are compatible with the theoretical stochiometric percentage mass loss of water (21%). For instance, the generated dihydrate crystals form β-HH before and after the

1st hydration cycle, as shown from SEM images in Figure 7, can be confirmed by STA and XRD results.

From the SEM image, as shown in Figure 12, the high influence of the grinding process on the crystal morphology generates very fine particles with a large number of defects. Therefore, the hydration rate after the first reaction cycle increased. Due to this change in the microstructure of hemihydrate, which was generated after the recycling of SA α-HH, the compressive strength fails.
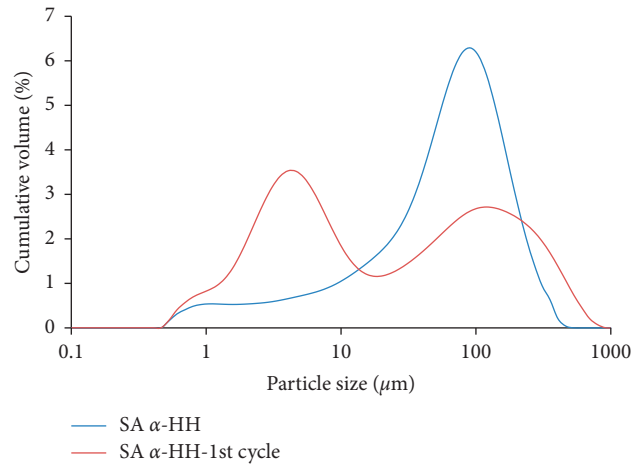
FIGURE 9: Particle size distribution of pure SA α-HH and SA α-HH after the first cycle.
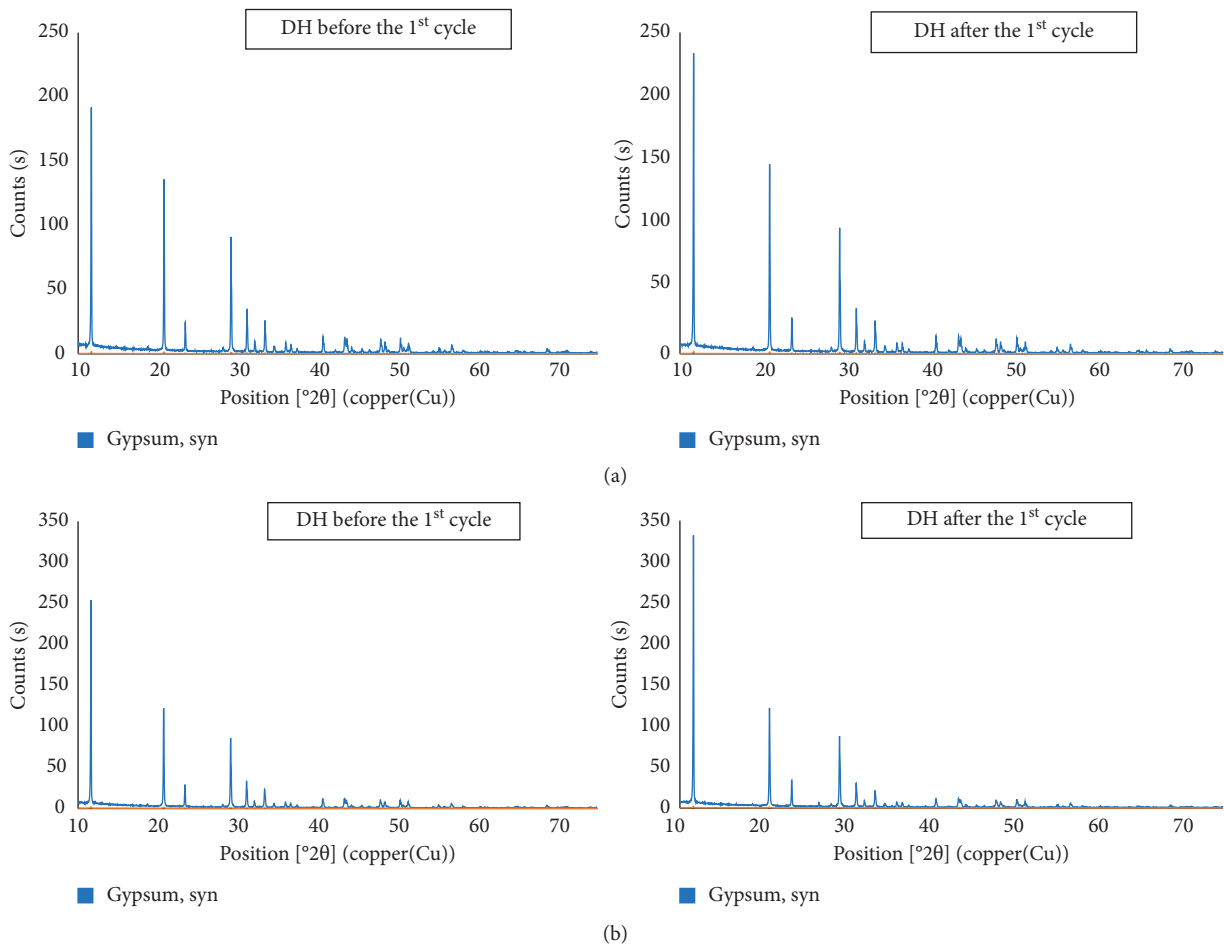

FIGURE 10: XRD patterns for the generated DH before and after the first hydration cycle from (a) β-HH and (b) α-HH.
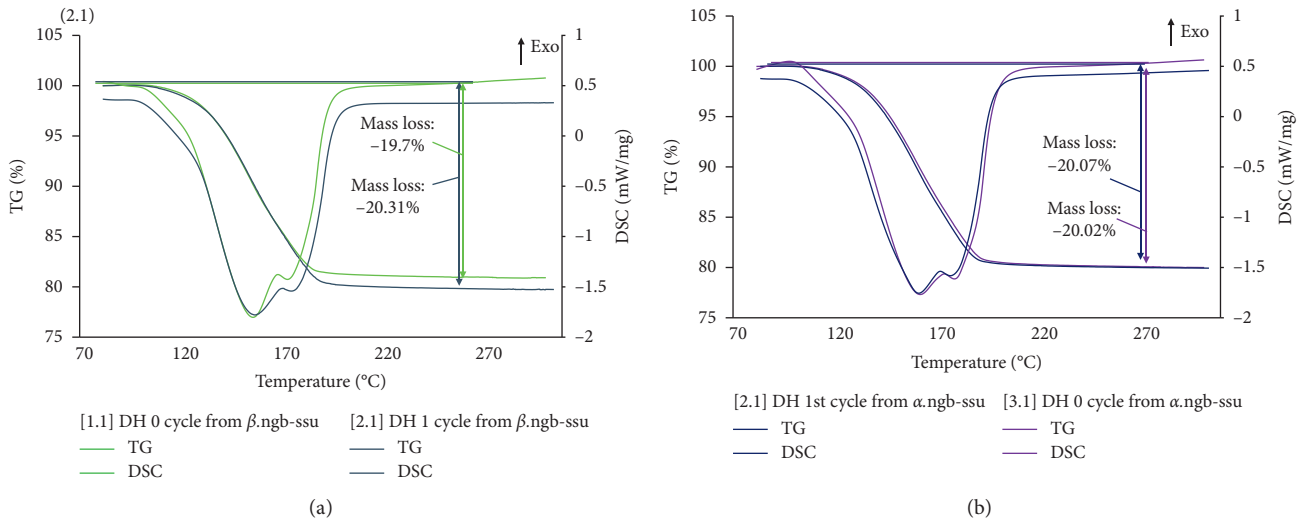
FIGURE 11: STA for the generated DH before and after the first hydration cycle from (a) β-HH and (b) α-HH.
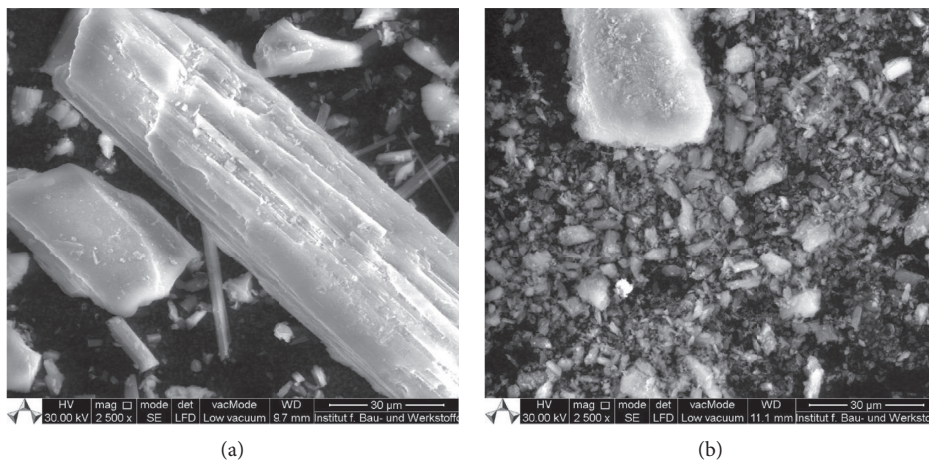

FIGURE 12: SEM images pure: (a) SA α-HH and (b) SA α-HH after the first cycle.

3. Conclusion

One of the major findings from this study was that the properties of the generated hemihydrate and dihydrate after the 1st reaction cycle were based on several factors such as type (α- or β-), purity, and properties of the hemihydrate in addition to the calcination mechanism and grinding procedure. The hydration rate of the recycled hemihydrate was varied due to the variation between the physical properties between the original hemihydrate and hemihydrate after the 1st reaction cycle. The differences in the mechanical properties of the formed dihydrate before and after cycling were based on several factors such as HH crystal size, HH surface area, water to hemihydrate ratio, pores generation during the drying process after hydration, the packing density, and the dihydrate crystal morphology. The grinding step of the recycled material decreases the particle size, increases the surface area, and changes the microstructure. The finer the particle size, the higher the amount of the required water to

perform better workability leading to a decrease in the compressive strength of the recycled hemihydrate. Grinding also leads to high surface defects on the crystals, which impacts the setting time and the microstructure of the recycled hemihydrate. With an increase of the surface area of the hemihydrate, the water demand and the maximum reached ion concentration in the reaction solution increase, which leads to more seed crystals formation. Because of that process, the dihydrate crystals get smaller, and the number of branches increases. On the basis of the obtained results of this study, the particle size, surface area, and surface morphology of the starting material of hemihydrate are very important which is altering the properties of hemihydrate during the recycling process. The recycled calcium sulfate hemihydrate has to be taken as a new resource with its own characteristics and special impurities. The reveled result of this study is significant for the normal production of beta hemihydrate from the natural or FGD-gypsum. For better results, the repetition of the recycling process is

recommended in order to improve the properties of the recycled material after several reaction cycles. Investigations of the following cycle steps are needed to understand the mechanism in detail and to prove if there is a limit in the surface increase of hemihydrate and dihydrate.

Data Availability

The data that support the findings of this study are available from the corresponding author upon request.

Conflicts of Interest

The authors declare that they have no conflicts of interest.

References

[1] K. Gupta, S. Singh, and M. S. R. Rao, "Direct and facile room-temperature synthesis of nanocrystalline calcium sulfate dihydrate (gypsum)," *Crystal Growth & Design*, vol. 16, no. 6, pp. 3256–3261, 2016.

[2] G. Camarini, M. C. C. Pinto, A. G. d. Moura, and N. R. Manzo, "Effect of citric acid on properties of recycled gypsum plaster to building components," *Construction and Building Materials*, vol. 124, pp. 383–390, 2016.

[3] R. H. Geraldo, S. M. M. Pinheiro, J. S. Silva et al., "Gypsum plaster waste recycling: a potential environmental and industrial solution," *Journal of Cleaner Production*, vol. 164, pp. 288–300, 2017.

[4] C. Zhu, J. Zhang, W. Yi, W. Cao, J. Peng, and J. Liu, "Research on degradation mechanisms of recycled building gypsum," *Construction and Building Materials*, vol. 173, pp. 540–549, 2018.

[5] H. C. F. Cordon, F. C. Cagnoni, and F. F. Ferreira, "Comparison of physical and mechanical properties of civil construction plaster and recycled waste gypsum from São Paulo, Brazil," *Journal of Building Engineering*, vol. 22, pp. 504–512, 2019.

[6] W. Lou, B. Guan, and Z. Wu, "Dehydration behavior of FGD gypsum by simultaneous TG and DSC analysis," *Journal of Thermal Analysis and Calorimetry*, vol. 104, no. 2, pp. 661–669, 2011.

[7] A. N. Christensen, M. Olesen, Y. Cerenius, and T. R. Jensen, "Formation and transformation of five different phases in the $CaSO_4–H_2O$ system: crystal structure of the subhydrate β-$CaSO_4 \cdot 0.5H_2O$ and soluble anhydrite $CaSO_4$," *Chemistry of Materials*, vol. 20, no. 6, pp. 2124–2132, 2008.

[8] C. Pritzel, R. Trettin, and Y. Sakalli, "Investigation of the hydration of hemihydrate with microscopic methods," in *Proceedings of the 14th European Microscopy Congress*, Aachen, Germany, September 2008.

[9] P. S. Bardella and G. Camarini, "Recycled plaster: physical and mechanical properties," *Advanced Materials Research*, vol. 374–377, pp. 1307–1310, 2011.

[10] G. Camarini, S. M. M. Pinheiro, and K. Tannous, "Thermal analysis of recycled gypsum from construction and demolition waste," *Applied Mechanics and Materials*, vol. 260-261, pp. 977–980, 2012.

[11] Z. Li, K. Xu, J. Peng, J. Wang, X. Ma, and J. Niu, "Investigation on the deterioration mechanism of recycled plaster," *Advances in Materials Science and Engineering*, vol. 2018, Article ID 4791451, 8 pages, 2018.

[12] G. Azimi, V. G. Papangelakis, and J. E. Dutrizac, "Modelling of calcium sulphate solubility in concentrated multi-component sulphate solutions," *Fluid Phase Equilibria*, vol. 260, no. 2, pp. 300–315, 2007.

[13] T. N. Harrison, "Experimental VNIR reflectance spectroscopy of gypsum dehydration: investigating the gypsum to bassanite transition," *American Mineralogist*, vol. 97, no. 4, pp. 598–609, 2012.

[14] Y.-W. Wang, Y.-Y. Kim, H. K. Christenson, and F. C. Meldrum, "A new precipitation pathway for calcium sulfate dihydrate (gypsum) via amorphous and hemihydrate intermediates," *Chemical Communications*, vol. 48, no. 4, pp. 504–506, 2012.

[15] S. J. Wang, Q. Chen, Y. Li, Y. Q. Zhuo, and L. Z. Xu, "Research on saline-alkali soil amelioration with FGD gypsum," *Resources, Conservation and Recycling*, vol. 121, pp. 82–92, 2017.

[16] S. Marinković, A. Kostić-Pulek, V. Logar, and P. Trifunović, "Recycling of waste FGD gypsum recycling of waste FGD gypsum," in *Proceedings of the 32 International Conference of Slovak Society of Chemical Engineering*, Tatranské Matliare, Slovakia, May 2005.

[17] S. Inazumi, H. Sano, and M. Yamada, "Estimation of gypsum hemihydrate content in recycled gypsums derived from gypsum boards," *Journal of Material Cycles and Waste Management*, vol. 18, no. 1, pp. 168–176, 2016.

[18] Z. Li, J. Peng, and X. Qiu, "Effect of different ways of STPP retarder addition on properties of recycled gypsum," *Journal of Wuhan University of Technology-Materials Science Edition*, vol. 32, no. 5, pp. 1125–1131, 2017.

[19] Z. Li, K. Xu, J. Peng, J. Wang, X. Ma, and J. Niu, "Study on hydration and mechanical property of portland cement-blended recycled plaster materials," *Advances in Materials Science and Engineering*, vol. 2018, Article ID 2692347, 8 pages, 2018.

[20] A. Ahmed and M. H. E. Naggar, "Effect of cyclic loading on the compressive strength of soil stabilized with bassanite-tire mixture," *Journal of Material Cycles and Waste Management*, vol. 20, no. 1, pp. 525–532, 2018.

[21] G. L. Vieira, A. P. Trovão, and C. R. Teles, "Perspective of environmental sustainability with waste recycling plaster in construction," in *Proceedings of the 16th International Waste Management and Landfill Symposium*, Cagliari, Italy, October 2017.

[22] S. M. M. Pinheiro and G. Camarini, "Characteristics of gypsum recycling in different cycles," *International Journal of Engineering and Technology*, vol. 7, no. 3, pp. 215–218, 2015.

[23] A. A. Khalil, A. Tawfik, A. A. Hegazy, and M. F. El-Shahat, "Effect of some waste additives on the physical and mechanical properties of gypsum plaster composites," *Construction and Building Materials*, vol. 68, pp. 580–586, 2014.

[24] T. Hofelich, L. Wadsö, A. L. Smith, S. Hamid, and S. Rose Mulligan, "The isothermal heat conduction calorimeter: a versatile instrument for studying processes in physics, chemistry, and biology," *Journal of Chemical Education*, vol. 78, 2001.

[25] 2018 Mettler-Toledo international inc. all rights reserved. perfection™ comb ca combination electrode, https://www.mt.com/de/en/home/products/Laboratory_Analytics_Browse/pH/sensor_electrode/Ion-selective_Electrodes/Combined_ISEs/perfectION_Ca_BNC.html.

[26] Malvern Instruments Ltd, *Mastersizer 2000*, Malvern Instruments Ltd., England, UK, 2006.

[27] S. Brunauer, P. H. Emmett, and E. Teller, "Adsorption of gases in multimolecular layers," *Journal of the American Chemical Society*, vol. 60, no. 2, pp. 309–319, 1938.

[28] I. Odler, "The BET-specific surface area of hydrated Portland cement and related materials," *Cement and Concrete Research*, vol. 33, no. 12, pp. 2049–2056, 2003.

[29] M. Ermrich and D. Opper, *XRD for the Analyst: Getting Acquainted with the Principles*, PANalytical, Almelo, Netherlands, 2nd edition, 2013.

[30] R. F. Egerton, *Physical Principles of Electron Microscopy: An Introduction to TEM, SEM, and AEM*, Springer, New York, NY, USA, 3rd edition, 2008.

[31] R. McCaffrey, *Recycling of gypsum and hydration of hemihydrate in the presence of retarding agents and other additives*, C. Pritzel, E. Abu Zeitoun, Y. Sakalli, and R. Trettin, Eds., Institut für Bau- und Werkstoffchemie, Universität Siegen, Siegen, Germany, 2018.

[32] O. Henning and D. Knöfel, *Baustoffchemie: Eine Einführung für Bauingenieure und Architekten; mit 104 Tafeln und zahlreichen Übungsbeispielen*, Verlag Bauwesen, Berlin, Germany, 6th edition, 2002.

[33] I. Berdugo, E. Romero, M. Saaltink, and M. Albis, "On the behaviour of the Ca-SO$_4$-H$_2$O system," *Revista de la Academia Colombiana de Ciencias Exactas*, vol. 32, no. 125, pp. 545–557, 2008.

[34] A. Lancia, D. Musmarra, and M. Prisciandaro, "Measuring induction period for calcium sulfate dihydrate precipitation," *AIChE Journal*, vol. 45, no. 2, pp. 390–397, 1999.

[35] G. Cao, *Nanostructures & Nanomaterials: Synthesis, Properties & Applications*, Imperial College Press, London, UK, 2004.

[36] H. Hamm, H. J. Kersten, and R. Hueller, "25 years experience gained in the European Gypsum Industry with the use of FGD gypsum," *Cement International*, vol. 4, pp. 92–102, 2004.

[37] D. Marchon, U. Sulser, A. Eberhardt, and R. J. Flatt, "Molecular design of comb-shaped polycarboxylate dispersants for environmentally friendly concrete," *Soft Matter*, vol. 9, no. 45, p. 10719, 2013.

[38] Jazmín Consuelo Aboytes Contreras, *Multi-Method Approach to Study the Influence of Additives in Ternary Systems: Gypsum, Water and Impurities*, Clausthal University of Technology, Clausthal-Zellerfeld, Germany, 2014.

[39] T. Rabizadeh, C. L. Peacock, and L. G. Benning, "Carboxylic acids: effective inhibitors for calcium sulfate precipitation?" *Mineralogical Magazine*, vol. 78, no. 6, pp. 1465–1472, 2014.

Research Article

Strength Properties of High-Strength Concrete Containing Coal Bottom Ash as a Replacement of Aggregates

In-Hwan Yang [ID],[1] Jihun Park,[1] Nhien Dinh Le,[1] and Sanghwa Jung[2]

[1]*Department of Civil Engineering, Kunsan National University, Daehak-ro 558, Kunsan, Jeonbuk 54150, Republic of Korea*
[2]*Korea Conformity Laboratories, Seoul 08503, Republic of Korea*

Correspondence should be addressed to In-Hwan Yang; ihyang@kunsan.ac.kr

Most previous studies on the strength properties of coal bottom ash (CBA) concrete have focused on concrete with a normal compressive strength, and thus, studies on the strength properties of high-strength concrete (HSC) containing CBA are limited. Therefore, the effects of replacing fine aggregates with CBA and variations in the curing age on the strength properties of HSC with a compressive strength of greater than 60 MPa were investigated in this study. The different CBA contents included 25, 50, 75, and 100%, and the different curing ages were 28 and 56 days. The mechanical properties of the HSC with CBA incorporated as fine aggregates were examined. The experimental results revealed that CBA could be partially or totally substituted for fine aggregates during HSC production. The test results also showed that the compressive, splitting tensile, and flexural strengths of the HSC containing CBA fine aggregates slightly decreased as the CBA content increased. Moreover, useful relationships between the compressive strength, splitting tensile strength, and flexural strength were suggested, and the predictions reasonably agreed with the measurements. Compared to those of the control specimen, the pulse velocities of the HSC specimens at various CBA contents decreased by less than 3%. In addition, equations for predicting the strength values of CBA concrete by using the ultrasonic pulse velocity were suggested.

1. Introduction

Coal bottom ash (CBA) is an industrial waste produced at the bottom of coal furnaces in thermal power plants [1–5]. Gollakota et al. [6] indicated that ash ponds or lagoons have caused numerous ecological problems and severe distress to local communities due to their increasing landfill space and escalating disposal costs. Therefore, CBA utilization is the best way to minimize the environmental concern of CBA and also conserves natural resources [7–9]. CBA was recently applied in several fields, especially in the construction industry [10–14].

The recycling rate of CBA in Korea was 7.1%, 11.3%, 14.6%, 17.3%, and 23.4%, respectively, in 2014 through 2018 [15]. Thus, the recycling rate of CBA in Korea has gradually increased over the past 4 years. In addition, according to a report [13] about recycling coal bottom ash, approximately

5% and 21% of the CBA were utilized as aggregate in mortar and concrete in the US and EU, respectively.

Moreover, CBA was recently used in the mixture of normal vibrating concrete and self-compacting concrete because the sizes of CBA and natural fine aggregate are similar and due to the pozzolanic activity of the CBA [11]. Several studies [16–22] actually reported that fine aggregates could be replaced by CBA in concrete fabrication. Singh et al. [16] reviewed the effect of using CBA as a natural fine aggregate replacement on the properties of normally vibrated and self-compacting concrete. This review reported that most of the compressive strength results of previous studies slightly decreased with increasing CBA contents, whereas some cases showed a high compressive strength at low replacement levels. Singh and Siddique [23] also implemented experimental tests to evaluate the strength properties of CBA concrete, which revealed that the compressive strengths of

CBA concrete at the different curing days were insignificantly reduced by using the CBA.

Regarding the tensile strength and flexural strength of conventional concrete containing CBA, test results in previous studies [24–27] showed that using CBA to replace fine aggregates decreased the splitting tensile strength and flexural strength of CBA concrete. Ngohpok et al. [26] estimated the mechanical properties of pervious concrete containing recycled concrete and bottom ash aggregates. The splitting tensile strength and flexural strength decreased as the recycled concrete and bottom ash aggregate contents increased. Ibrahim et al. [28] also investigated the utilization of CBA in self-compacting concrete. They showed that the greatest tensile strength of the self-compacting concrete containing CBA was 3.28 MPa, when fine aggregate was replaced by 10% CBA.

Due to the development of construction technology, high-strength concrete (HSC) has become commercially available [29–31]. However, most studies on the material properties of CBA concrete have focused on the strength properties of conventional concrete with a compressive strength of less than 40 MPa. Recently, Kim and Lee [32] investigated the influences of replacing fine and coarse aggregates with power bottom ash on the mechanical properties of HSC. This study reported that substituting CBA for natural fine and coarse aggregates affected the flexural strength more significantly than the compressive strength of the HSC. CBA utilization for HSC is still limited; therefore, experimental research on HSC with fine aggregates partially or fully replaced by CBA is essential.

In this study, the strength properties of concrete specimens with natural fine aggregates partially or fully replaced by CBA aggregates (25, 50, 75, and 100%) and with a compressive strength of greater than 60 MPa were investigated. For fresh concrete, a slump test was performed to examine the workability of the CBA concrete. For hardened concrete, the unit weight, compressive strength, tensile strength, flexural strength, and ultrasonic pulse velocity were investigated at different curing ages of 28 and 56 days. Finally, the relationships between the compressive strength, tensile strength, and flexural strength and the ultrasonic pulse velocity of the CBA concrete specimens were proposed.

2. Experimental Program

2.1. Aggregates. The natural fine and coarse aggregates used in this study were crushed, but the source of each aggregate was different. The natural fine aggregates are shown in Figure 1(a). The particle size distribution of the natural fine aggregates is shown in Figure 2. The maximum size of the natural coarse aggregates used in this study was 20 mm. The density and water absorption results of the natural fine and coarse aggregates are also shown in Table 1. The densities of the natural fine and coarse aggregates were 2.60 and 2.61 g/cm^3, respectively.

The CBA used in this study was collected from a thermal power plant company. The CBA fine aggregates, which passed through a 5.0 mm sieve and remained on a 0.15 mm

sieve, were applied to fabricate the concrete. The CBA used for this study is presented in Figure 1(b), and the particle size distribution of the CBA is also presented in Figure 2. The test results of the density and water absorption of the CBA are shown in Table 1. The test results indicated that the density of the CBA was smaller than that of natural fine aggregates. However, the water absorption of the bottom ash of 6.87% was approximately 10 times higher than that of the crushed fine aggregate of 0.69%. Additionally, the fineness modulus of the CBA was 3.83, whereas that of the fine aggregates was 3.17. The chemical compositions derived from energy dispersive spectrometry (EDS) analysis of the CBA are shown in Table 2. The CBA used in this study was mainly composed of SiO_2 (62.94%), Al_2O_3 (18.09%), and Fe_2O_3 (9.95%), and the total amount of these compositions was 90.98%. The minor compositions included CaO and Na_2O. Figure 3 shows the scanning electron microscopy (SEM) and EDS analysis results. The shape of the CBA is complex and irregular. In addition, there are small voids with different sizes in the CBA.

2.2. Mix Proportions. A concrete mix with a target compressive strength of 60 MPa at a curing age of 28 days was designed. The constituent materials used in the production of the control concrete and the CBA concrete are indicated in Table 3. There are five different mixtures of concrete with various percentages of CBA as fine aggregates.

In previous studies [18–20], the water-cement ratio ranged from 0.45 to 0.6, when the compressive strengths were less than 40 MPa, and also, the compressive strengths of the concrete gradually reduced as the water-cement ratio increased. Moreover, for a high-strength concrete mixture, a high water content is not recommended because unbound water may result in pores inside the concrete and cause the concrete to shrink, which adversely affects the compressive strength of concrete. Accordingly, in this study, the high compressive strength of CBA concrete could be achieved with a low water-cement ratio. A water-cement ratio of 0.3 was used in all the concrete mixtures in this study. This water-cement ratio was much less than that of the previous studies.

In addition to the control concrete mixture, for each mixture, CBA replaced 25, 50, 75, and 100% of the natural fine aggregates by volume in the concrete. The unit contents of cement and natural coarse aggregates were fixed at 595.0 kg/m^3 and 878.5 kg/m^3, respectively, when fabricating all the mixtures. Ordinary Portland cement (OPC) was used as the basic binder. A high water-reducing agent (HWRA) with a unit content of 3.6 kg/m^3, which corresponded to 0.6% OPC by weight, was used to enhance the workability of the CBA concrete at a low water-cement ratio. The CBA concrete mixtures were designated M00, M25, M50, M75, and M100, in which the number in each mixture label represents the percentage of the fine aggregates replaced by CBA.

2.3. Casting and Curing the Specimens. Cylindrical specimens with dimensions of 100 mm × 200 mm were cast to measure the unit weight, compressive strength, and splitting

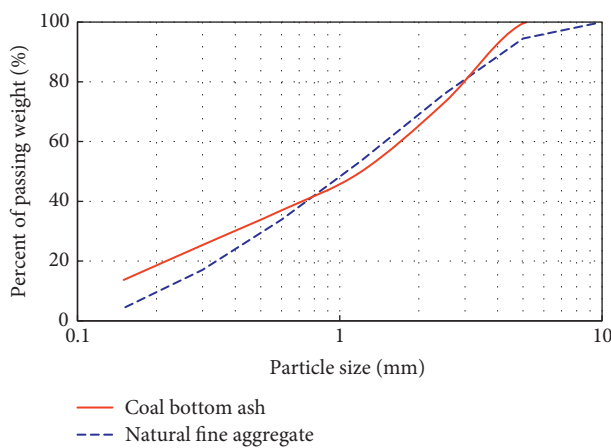FIGURE 1: Natural fine aggregates and CBA aggregates. (a) Natural fine aggregates. (b) CBA aggregates.

FIGURE 2: Grading curves of the CBA and natural fine aggregates.

tensile strength of the CBA concrete, and prism specimens with dimensions of 100 mm × 100 mm × 400 mm were fabricated to measure the flexural strength of the concrete. As soon as the specimens were cast, they were covered with plastic wrap and moist-cured for one day after casting. Then, the specimens were demolded at a curing age of 24 ± 1 hour and then cured in the water tank at $23 \pm 2°C$ until the specified testing age.

2.4. Test Procedure. For the fresh concrete, a slump test was performed to examine the workability of the concrete. For the hardened concrete, the unit weight, compressive strength, splitting tensile strength, flexural strength, and ultrasonic pulse velocity of the concrete were measured at curing ages of 28 and 56 days. The compressive strength of the CBA concrete specimens was measured by testing cylindrical specimens with a hydraulic testing machine in accordance with the KS F 2405 test method [33]. The splitting tensile strength test was also determined by testing cylindrical specimens in accordance with the KS F 2423 test method [34]. The flexural strength of the CBA concrete was measured by testing prism specimens under four-point loading in accordance with the KS F 2408 test method [35]. The average values of the three specimens

were recorded to obtain the mechanical properties of the concrete.

An ultrasonic pulse velocity test was also implemented, and the test results were used to estimate the uniformity and relative quality of the CBA concrete. The ultrasonic pulse velocity tests conformed to the ASTM C597-09 test method [36]. Three cylindrical specimens of each mixture were prepared, and both ends of each specimen were polished to ensure flat contact between the transducers and end surfaces of the specimen. Moreover, to achieve accurate pulse travel time measurements, the applied frequency of the transducers was 54 kHz. During this test, one transducer was held on the surface of a cylindrical specimen, which transmitted pulses of compressional waves through the concrete specimen. These pulses were received and converted into electrical energy by another transducer, which was held on another surface of the concrete specimen.

3. Test Results and Discussions

Concrete applications in the construction industry may be considered in terms of two concrete properties. One is the mechanical properties of the concrete, and the other is the durability of the concrete. This study investigated the mechanical properties of HSC including CBA, but the concrete durability was beyond the scope of this study.

3.1. Workability. The workability of the fresh CBA concrete was determined by performing a slump test. The test results are shown in Figure 4. The slump of the CBA concrete mixtures declined as the crushed fine aggregate replacement by CBA increased. The slumps of CBA concrete mixtures M25, M50, M75, and M100 were 75, 70, 67.5, and 45 mm, respectively, whereas that of the control concrete mixture was 80 mm. The reduction in the workability of CBA concrete was caused by the increase in surface area and the irregular shapes of the CBA particles. In addition, utilization of CBA as fine aggregates enhanced the concrete texture, which had more irregular and porous particles than the control concrete. For that reason, the interparticle friction increased, which led to an obstruction of the workability of the fresh concrete. The test results in this study are

TABLE 1: Physical properties of the CBA, natural fine, and coarse aggregates.

Material	Density (g/cm^3)	Water absorption (%)	Fineness modulus
Natural fine aggregates	2.60	0.69	3.17
Natural coarse aggregates	2.61	1.44	6.77
CBA	1.84	6.87	3.83

TABLE 2: Chemical composition of the CBA.

Compound	CBA (%)
SiO_2	62.94
Al_2O_3	18.09
Fe_2O_3	9.95
CaO	5.08
Na_2O	1.58
K_2O	0.99
MgO	1.37

comparable to those reported by Singh and Siddique [20]. Their test results indicated that the water demand of CBA concrete increased to attain the same slump values as control concrete and that the water requirement decreased, when a water-reducing admixture was used.

3.2. Unit Weight.

The unit weight test results of the concrete specimens with different CBA contents are presented in Figure 5. This figure shows that the unit weights of the concrete decreased as the CBA content increased. At a curing age of 28 days, the unit weight of CBA concrete mixtures M25, M50, M75, and M100 slightly decreased by 2.1, 3.2, 5.3, and 7.6% compared to that of the control concrete mixture (2370.2 kg/m^3), respectively. At a curing age of 56 days, the unit weight of the CBA concrete mixtures M25, M50, M75, and M100 decreased by 2.0, 3.7, 5.8, and 6.7% compared to that of the control concrete mixture (2386.5 kg/m^3), respectively. The decline in the unit weight of the CBA concrete mixtures might be attributed to the smaller density of the CBA aggregate compared to that of natural fine aggregates. Hence, the CBA aggregates play the role of lightweight aggregates rather than conventional crushed aggregates.

The unit weights of the concrete specimens with different curing ages are also shown in Figure 5. When the curing age increased from 28 to 56 days, the unit weights of the concrete with 0, 25, 50, 75, and 100% replacement of crushed fine aggregate by CBA insignificantly increased by 0.7, 0.9, 0.2, 0.1, and 1.6%, respectively. With the interaction of the chemical components of the CBA with cement paste, the concrete matrix at a curing age of 56 days was slightly more packed than that at a curing age of 28 days. That was why the unit weight of the CBA concrete increased slightly with increasing curing age.

3.3. Compressive Strength.

The compressive strength test results of concrete specimens with different CBA contents are presented in Figure 6. At a curing age of 28 days, the overall compressive strength of the CBA mixtures decreased as the CBA content increased. The compressive strength of CBA concrete mixture M25 increased insignificantly by 1.2% in comparison to that of the control concrete mixture (69.4 MPa). In contrast, the compressive strength values of CBA concrete mixtures M50, M75, and M100 declined by 3.0, 4.6, and 8.8% compared to that of the control concrete mixture, respectively. At a curing age of 56 days, the compressive strength values of CBA concrete mixtures M25, M50, M75, and M100 declined by 2.0, 3.0, 4.8, and 6.2% compared to that of the control concrete mixture (76.7 MPa), respectively. The decline in the compressive strengths of the CBA concrete can be explained by the increase in the porosity in the concrete because the pores in the CBA concrete cause a negative influence on the compressive strength of the concrete specimens. The test results in this study were comparable with the previous experimental studies reported by Muthusamy et al. [37] and Abdulmatin et al. [3]. In their studies, the incorporation of CBA aggregates instead of natural fine aggregates had an adverse effect on the compressive strength of concrete at a curing age of 28 days. The substitution of stronger materials (natural aggregates) by weaker materials (CBA) was the factor causing the decline in the compressive strength of the concrete specimens.

Moreover, the compressive strength values of the CBA concrete in all mixtures exceeded 60 MPa, which could be regarded as HSC. The test results in this study implied that CBA could be used for the fabrication of HSC.

The long-term strength of CBA concrete may be higher than that of control concrete because of the pozzolanic activity of the CBA [3, 38]. For example, Abdulmatin et al. [3] showed that the compressive strength of a CBA mortar increased by 16.1–26.8%, when the curing ages increased from 28 to 90 days, whereas the compressive strength of the control mortar increased by 17.7%, when the curing ages increased from 28 to 90 days. However, in this study, the effect of curing for only 28 and 56 days on the strengths of CBA concrete was investigated, because the strengths at these curing ages are usually considered when designing concrete structures.

The compressive strength values of the concrete specimens with different curing ages are also shown in Figure 6. When the curing ages increased from 28 to 56 days, the compressive strength values of the concrete with 0, 25, 50, 75, and 100% replacement of fine aggregates by CBA increased by 10.4, 6.9, 10.4, 10.2, and 13.6%, respectively. The substantial increase in the compressive strength of the CBA concrete mixtures at a curing age of 56 days was due to the pozzolanic activity of the CBA. For the CBA concrete with a longer curing age, calcium hydroxide begins to react with the CBA particles and create calcium silicate hydrate (C-S-H) gel [23]. With increasing curing age, calcium silicates and aluminates are formed by the reaction between reactive silica in the CBA and alkali calcium hydroxide from the hydration of cement. These calcium silicates and aluminates fill the voids in the interfacial transition zone and enhance the compressive strength.
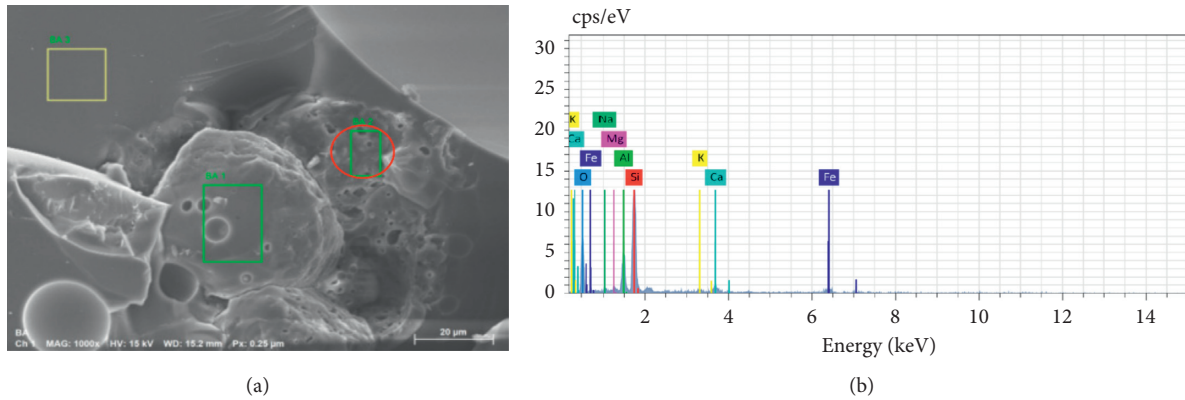
(a)

(b)

FIGURE 3: SEM and EDS results of the CBA. (a) SEM morphology of the CBA. (b) EDS spectra of the CBA (at the red circle in (a)).

TABLE 3: Mixing proportions of the CBA concrete.

| Mixture | Replacement of fine aggregates with CBA (%) | W/C | Water | Cement (OPC)[a] | Unit content (kg/m^3) | | | |
					Natural coarse aggregates	Natural fine aggregates	CBA	HWRA[b] (0.6% × cement)
M00	0	0.3	178.5	595.0	878.5	663.0	0.0	3.6
M25	25	0.3	178.5	595.0	878.5	497.2	117.7	3.6
M50	50	0.3	178.5	595.0	878.5	331.5	235.3	3.6
M75	75	0.3	178.5	595.0	878.5	165.7	353.0	3.6
M100	100	0.3	178.5	595.0	878.5	0.0	470.7	3.6

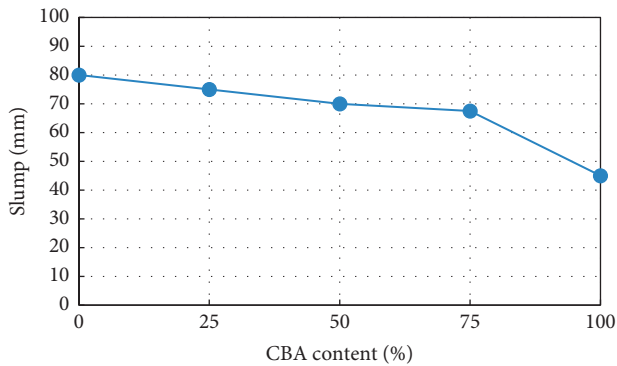[a]OPC: ordinary Portland cement. [b]HWRA: high water-reducing agent.

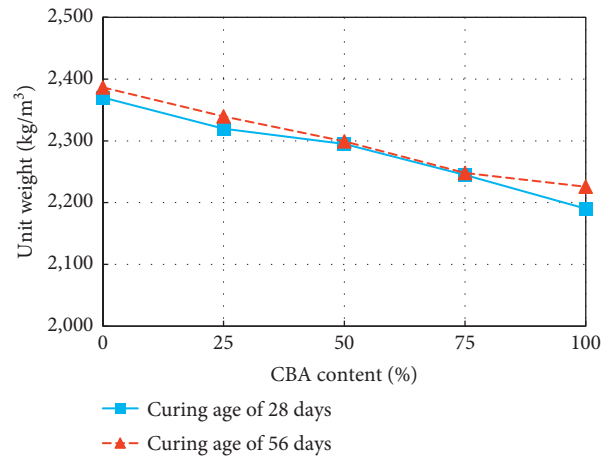FIGURE 4: Effect of the CBA on the slump of the concrete.

FIGURE 5: Unit weight test results.

3.4. Splitting Tensile Strength.

The splitting tensile strength values of the concrete specimens with different CBA contents are shown in Figure 7. The tendency of the tensile strength test results with the increase in the CBA contents was less clear than that of the compressive strength. At a curing age of 28 days, the splitting tensile strength of the CBA concrete mixtures including 25% CBA as fine aggregates was 15.8% lower than that of the control concrete mixture. However, the splitting tensile strength values of the CBA concrete mixtures incorporating 50, 75, and 100% CBA as fine aggregates were 9.7, 4.0, and 17.2% lower than that of the control concrete mixture, respectively. At a curing age of 56 days, the splitting tensile strengths of the concrete mixtures incorporating 25, 50, 75, and 100% CBA as fine

aggregates were 6.8, 7.4, 6.4, and 4.9% lower than that of the control concrete mixture, respectively. The splitting tensile strength difference between the CBA concrete and the control concrete became less distinct at a curing age of 56 days than at 28 days. The decrease in the splitting tensile strength with increasing CBA content was due to the increase in the volume of pores in the concrete gained by replacing the fine aggregates with CBA.

In addition, the splitting tensile strength of each mixture exceeded 4 MPa. This meant that the splitting tensile strength of HSC containing CBA as fine aggregates in this
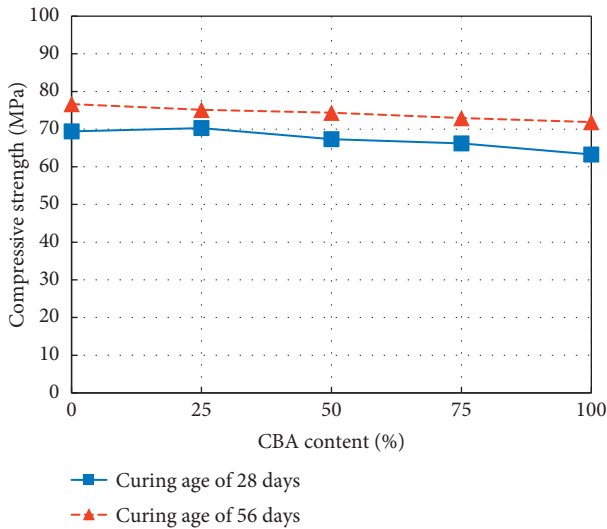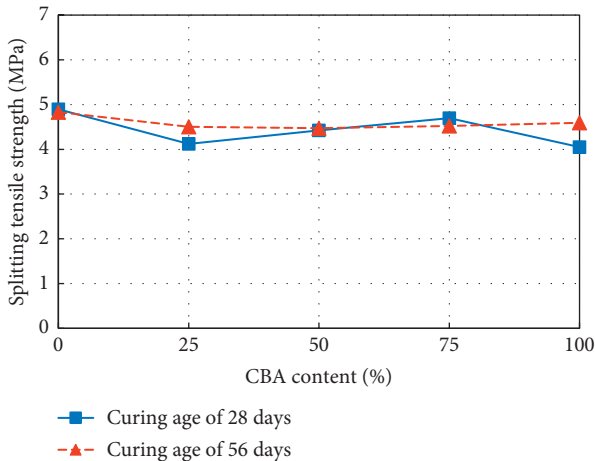
FIGURE 6: Compressive strength test results.

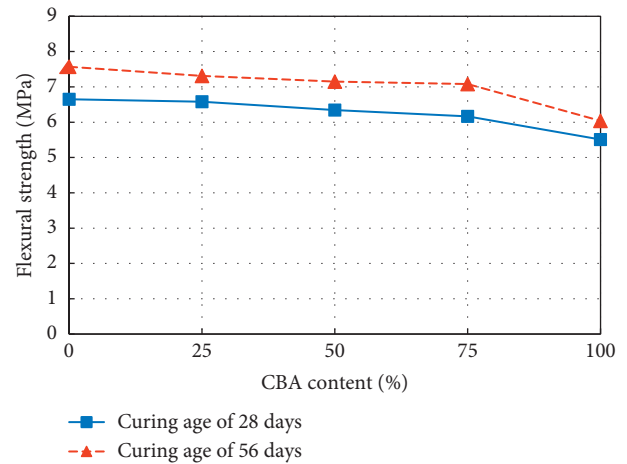FIGURE 7: Splitting tensile strength test results.

FIGURE 8: Flexural strength test results.

values of CBA concrete mixtures M25, M50, M75, and M100 were reduced by 3.4, 5.5, 6.5, and 20.2% in comparison with that of the control mixture (7.6 MPa), respectively. The flexural strength difference between the CBA concrete and the control concrete at a curing age of 56 days was quite similar to that at a curing age of 28 days. At both curing ages of 28 and 56 days, compared to the flexural strength of the mixture containing natural fine aggregates only, the reduction in the flexural strength of the mixture containing 100% CBA fine aggregates was more remarkable than that of mixtures containing 25, 50, and 75% CBA fine aggregates.

The flexural strength values of the concrete specimens with different curing ages are also shown in Figure 8. When the curing age increased from 28 to 56 days, the flexural strength values of the concrete containing 0, 25, 50, 75, and 100% replacements of fine aggregates by CBA increased by 13.8, 11.1, 12.7, 14.9, and 9.6%, respectively. The increase in flexural strength of the CBA concrete with increasing curing time primarily resulted from the pozzolanic reaction of the CBA, as described in the earlier section regarding compressive strength.

3.6. Relationship between the Compressive Strength, Splitting Tensile Strength, and Flexural Strength. In this study, to examine the relationship between the different strengths of CBA concrete, a regression analysis was performed. In the regression analysis, the coefficient of determination (R^2), normally ranging from 0 to 1, represents the goodness of a model fit. An R^2 value close to 1 indicates that the regression accurately fits the data and vice versa. Regression analysis was performed based on two approaches. The first regression analysis incorporated the test results obtained only in this study, and the second incorporated the test results obtained in this study and in previous studies by using exponential functions.

The relationship between the splitting tensile strength and compressive strength of the CBA concrete under two different curing ages is demonstrated in Figure 9(a). Moreover, the relationship between the splitting tensile strength and compressive strength of the CBA concrete,

study would be comparable to that of conventional normal-strength concrete containing natural aggregates.

The splitting tensile strength values of the concrete specimens with different curing ages are also shown in Figure 7. When the curing age increased from 28 to 56 days, the tensile strengths of concrete with the substitution of 0 and 75% of CBA as fine aggregates decreased by 1.3 and 3.8%, respectively, whereas the tensile strength values of the concrete with 25, 50, and 100% replacement of fine aggregates by CBA increased by 9.2, 1.1, and 13.4%, respectively.

3.5. Flexural Strength. The flexural strength test results with different CBA contents are shown in Figure 8. At a curing age of 28 days, the flexural strength values of the CBA concrete mixtures incorporating 25, 50, 75, and 100% CBA as fine aggregates were reduced by 1.0, 4.6, 7.3, and 17.1% in comparison with that of the control mixture (6.6 MPa), respectively. At a curing age of 56 days, the flexural strength

which are based on the test results in this study, is derived by the following equation:

$$f_t = 2.9085e^{0.0062f_c}, \quad R^2 = 0.19, \tag{1}$$

where f_t is the splitting tensile strength (MPa) and f_c is the compressive strength (MPa).

The splitting tensile strength of the CBA concrete was nearly exponentially proportional to that of the compressive strength. The porosity in the concrete matrix derived from replacing fine aggregates with CBA increased, which resulted in decreases in both the compressive strength and the splitting tensile strength of the concrete. However, increasing the curing time led to an increase in both the compressive strength and the splitting tensile strength. The relationship between the splitting tensile strength and compressive strength of the CBA concrete based on the test results in this study and in previous studies [24, 39] is shown in Figure 9(b). The compressive strengths of the CBA concrete varied from 15 to 37 MPa in the study by Rafieizonooz et al. [24] and ranged from 40 to 59.5 MPa in the study by Nikbin et al. [39]. The compressive strength values of CBA concrete in previous studies were less than approximately 60 MPa, whereas the compressive strength values of the CBA concrete in this study ranged from 63.3 to 76.7 MPa, thereby exceeding 60 MPa.

The proposed exponential equation used to predict the relationship between the compressive strength and the splitting tensile strength of CBA concrete, as obtained from the test results in this study and in previous studies, is expressed as follows:

$$f_t = 1.6635e^{0.0175f_c}, \quad R^2 = 0.66, \tag{2}$$

where f_t is the splitting tensile strength (MPa) and f_c is the compressive strength (MPa).

Overall, this equation underestimated the tensile strength values, when the compressive strength values ranged from approximately 40 to 60 MPa, whereas it overestimated the tensile strength values, when the compressive strength values ranged from approximately 60 to 80 MPa.

The relationship between the flexural strength and compressive strength of the CBA concrete under two different curing ages is shown in Figure 10(a). The flexural strength of the CBA concrete increased as the compressive strength increased. The relationship tendency between the flexural strength and compressive strength of the CBA concrete was similar to that between the splitting tensile strength and compressive strength of the CBA concrete. The relationship between the flexural strength and compressive strength of the CBA concrete, based on the test results in this study, is derived by the following equation:

$$f_r = 1.5192e^{0.0208f_c}, \quad R^2 = 0.81, \tag{3}$$

where f_r is the flexural tensile strength (MPa) and f_c is the compressive strength (MPa).

Rafieizonooz et al. [24] and Nikbin et al. [39] also implemented an experimental program for measuring the flexural strength of concrete containing CBA aggregates. The relationship between the flexural strength and compressive strength of the CBA concrete based on the test results in this study and in their studies is shown in Figure 10(b). An exponential equation for predicting the relationship between the flexural strength and compressive strength of CBA concrete is suggested as follows:

$$f_r = 2.627e^{0.0151f_c}, \quad R^2 = 0.71, \tag{4}$$

where f_r is the flexural tensile strength (MPa) and f_c is the compressive strength (MPa).

This equation underestimated the flexural strength values when the compressive strength values ranged from 40 to 60 MPa, whereas it overestimated the flexural strength values, when the compressive strength values ranged from 60 to 80 MPa.

Finally, the relation between the splitting tensile strength and flexural tensile strength of the CBA concrete under two different curing ages is shown in Figure 11(a). Overall, the splitting tensile strength values of the CBA concrete were nearly proportional to the flexural strength values of the CBA concrete. The relationship equation between the splitting tensile and flexural strength of the CBA concrete, based on the test results in this study, is proposed by the following equation:

$$f_t = 3.3715e^{0.0436f_r}, \quad R^2 = 0.21, \tag{5}$$

where f_t is the splitting tensile strength (MPa) and f_r is the flexural tensile strength (MPa).

The relationship between the splitting tensile strength and flexural tensile strength of the CBA concrete based on the test results in this study and in previous studies [24, 39] is shown in Figure 11(b). An exponential equation for predicting the splitting tensile strength of the CBA concrete by using the flexural strength is suggested as follows:

$$f_t = 1.2717e^{0.195f_r}, \quad R^2 = 0.64, \tag{6}$$

where f_t is the splitting tensile strength (MPa) and f_r is the flexural tensile strength (MPa).

3.7. Ultrasonic Pulse Velocity.

The ultrasonic pulse velocity experimental results of concrete specimens with different CBA contents are illustrated in Figure 12. At a curing age of 28 days, the ultrasonic velocities of the CBA concrete mixtures M25, M50, M75, and M100 were reduced by 0.4, 0.9, 2.1, and 2.7% compared to the control mixture M00, respectively. At a curing age of 56 days, the ultrasonic velocities of CBA concrete mixtures M25, M50, M75, and M100 were also reduced by 0.9, 1.4, 2.1, and 2.6% compared to that of the control mixture M00, respectively. Ultrasonic pulse waves pass faster through a solid body than through space [40]. Hence, increases in the void content of the CBA aggregate might cause a decrease in the ultrasonic pulse velocity. Moreover, when the curing age increased from 28 to 56 days, the ultrasonic velocities of the CBA concrete mixtures with CBA fine aggregate contents of 0, 25, 50, 75, and 100% increased by 1.0, 0.5, 0.5, 1.0, and 1.1%, respectively. Therefore, the test results indicated that the ultrasonic
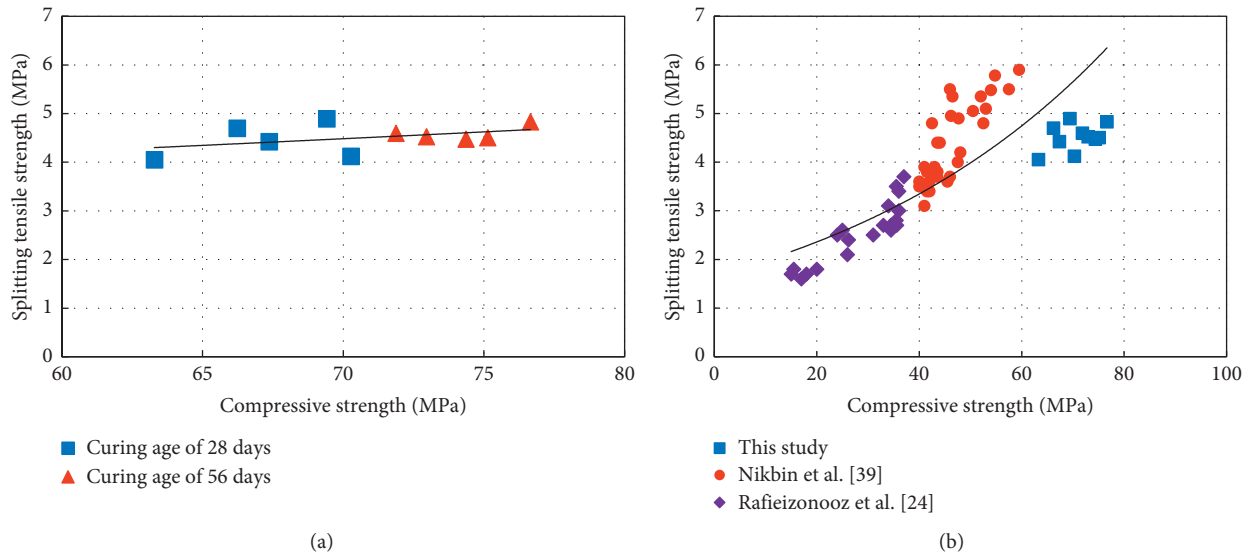
(a)

(b)

FIGURE 9: Relationship between the splitting tensile strength and compressive strength. (a) Test results in this study. (b) Test results in this study and previous studies.
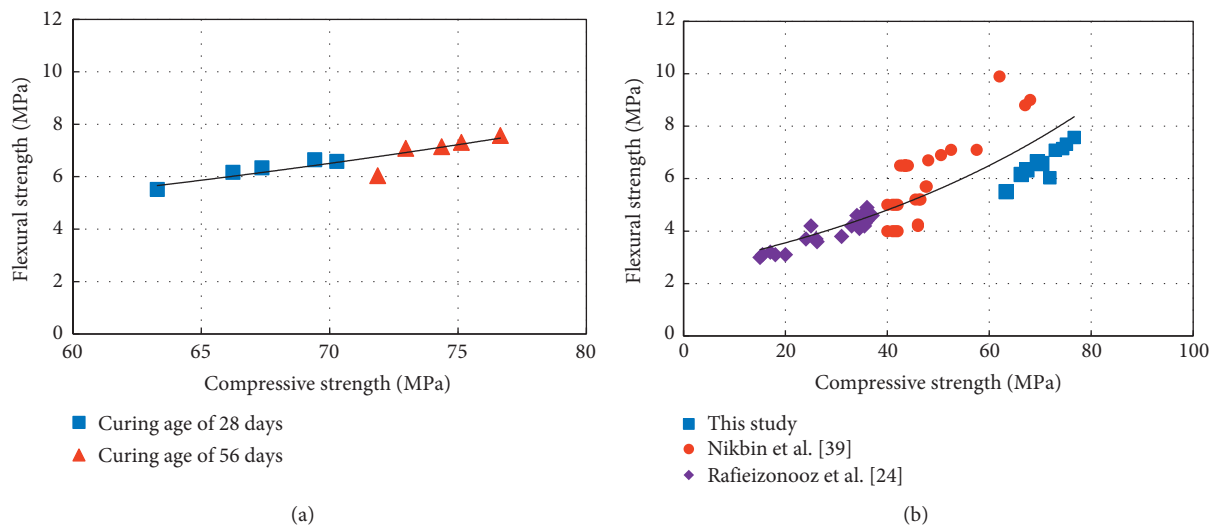

(a)

(b)

FIGURE 10: Relationship between the flexural strength and compressive strength. (a) Test results in this study. (b) Test results in this study and previous studies.

pulse velocities of the CBA concrete mixtures decreased with increasing CBA content but slightly increased with increasing curing age.

The relationship between the compressive strength and ultrasonic pulse velocity of the CBA concrete obtained in this study is shown in Figure 13(a). As expected, the overall compressive strength of the CBA concrete increased as the ultrasonic pulse velocity of the CBA concrete increased. The relationship between the compressive strength and the ultrasonic pulse velocity of the CBA concrete is shown in Figure 13(b), in which the test results in this study and in other studies [18, 24] are included. The measured values in this study and those in the existing studies represented significant deviations. This phenomenon might be due to the

difference between the chemical components of the CBA used in this study and those in the existing studies. By using these test results, an equation for predicting the relationship between the compressive strength and the ultrasonic pulse velocity of the CBA concrete is suggested as follows:

$$f_c = 0.6968e^{0.001V}, \quad R^2 = 0.17, \tag{7}$$

where f_c is the compressive strength (MPa) and V is the ultrasonic pulse velocity (m/s).

As expected, the coefficient of determination (R^2) in (4) was not high, meaning that the relationship between the test results and predictions was not good because there were significant deviations between the test results in this study and those in the existing studies, as shown in Figure 13(b).
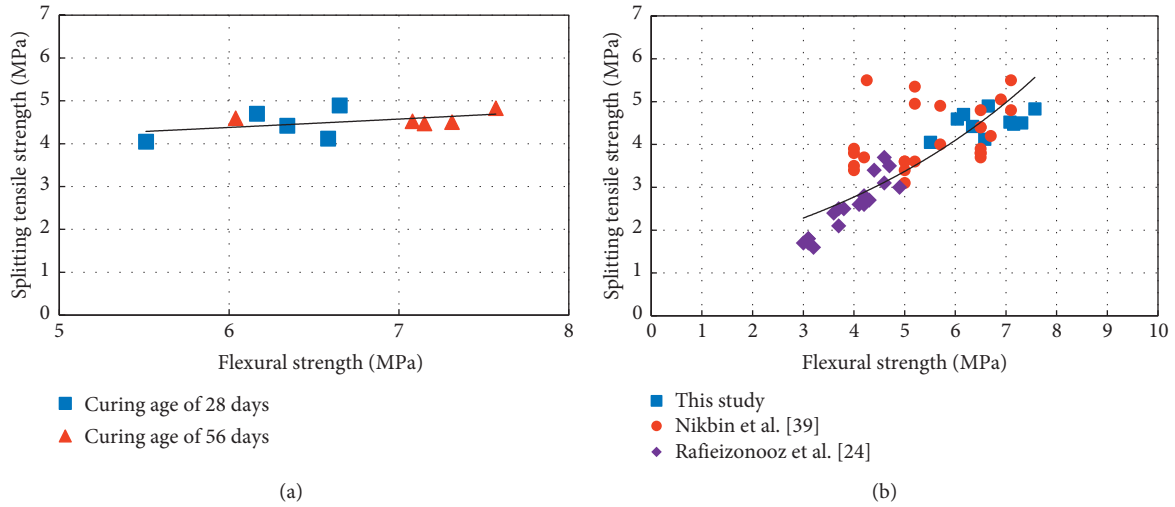
(a)

(b)

FIGURE 11: Relationship between the splitting tensile strength and flexural strength. (a) Test results in this study. (b) Test results in this study and previous studies.
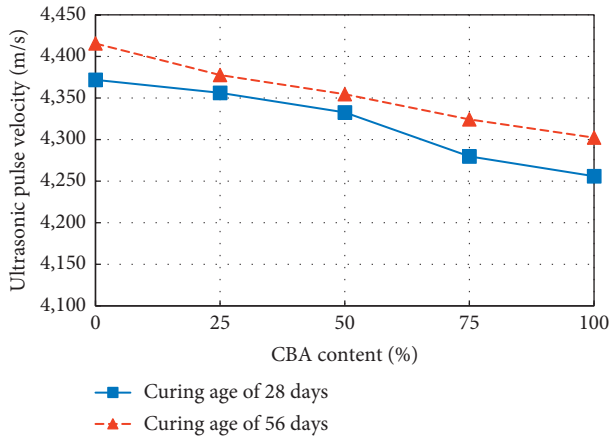

FIGURE 12: Ultrasonic pulse velocity test results.

Figure 14(a) shows the relationship between the splitting tensile strength and ultrasonic pulse velocity of the CBA concrete obtained in the study. As the ultrasonic pulse velocity increased, both the compressive strength and the splitting tensile strength of the CBA concrete increased.

The relationship between the splitting tensile strength and the ultrasonic pulse velocity of the CBA concrete is shown in Figure 14(b), in which the test results in this study and in another study [24] are included. By using these test results, an equation for predicting the relationship between the splitting tensile strength and the ultrasonic pulse velocity of the CBA concrete is suggested as follows:

$$f_t = 0.0004e^{0.0021V}, \quad R^2 = 0.71, \tag{8}$$

where f_t is the splitting tensile strength (MPa) and V is the ultrasonic pulse velocity (m/s).

In the figure, there are some deviations in predicting the splitting tensile strength when the ultrasonic pulse velocities were between approximately 4200 and 4500 m/s. The

predictions underestimated the measurements in this study but overestimated the measurements in the other study.

Finally, the relationship between the flexural strength and ultrasonic pulse velocity of the CBA concrete measured in this study is shown in Figure 15(a). The CBA concrete flexural strength was closely related to the ultrasonic pulse velocity.

The relationship between the flexural strength and the ultrasonic pulse velocity of the CBA concrete is shown in Figure 15(b), in which the test results in this study and in another study [24] are also included. An equation for predicting the relationship between the flexural strength and the ultrasonic pulse velocity of the CBA concrete is suggested as follows:

$$f_r = 0.0062e^{0.0016V}, \quad R^2 = 0.59, \tag{9}$$

where f_r is the flexural strength (MPa) and V is the ultrasonic pulse velocity (m/s).

As the predictions underestimated the splitting tensile strength values of the CBA concrete, which were measured in this study, the predictions also underestimated the flexural strength values of the CBA concrete, which were measured in this study. These phenomena occurred because the splitting tensile strength of the CBA concrete was related to the flexural strength, as shown in Figures 11(a) and 11(b).

4. Conclusions

The strength properties of CBA concrete with compressive strength values greater than 60 MPa were investigated in this study. Based on the extensive experimental results, the following conclusions can be drawn:

(1) The test results showed that, at low CBA contents, the unit weight of the HSC concrete slightly reduced by approximately 2%-3%. These results implied that low CBA contents could be applied to fabricate HSC with a normal weight.
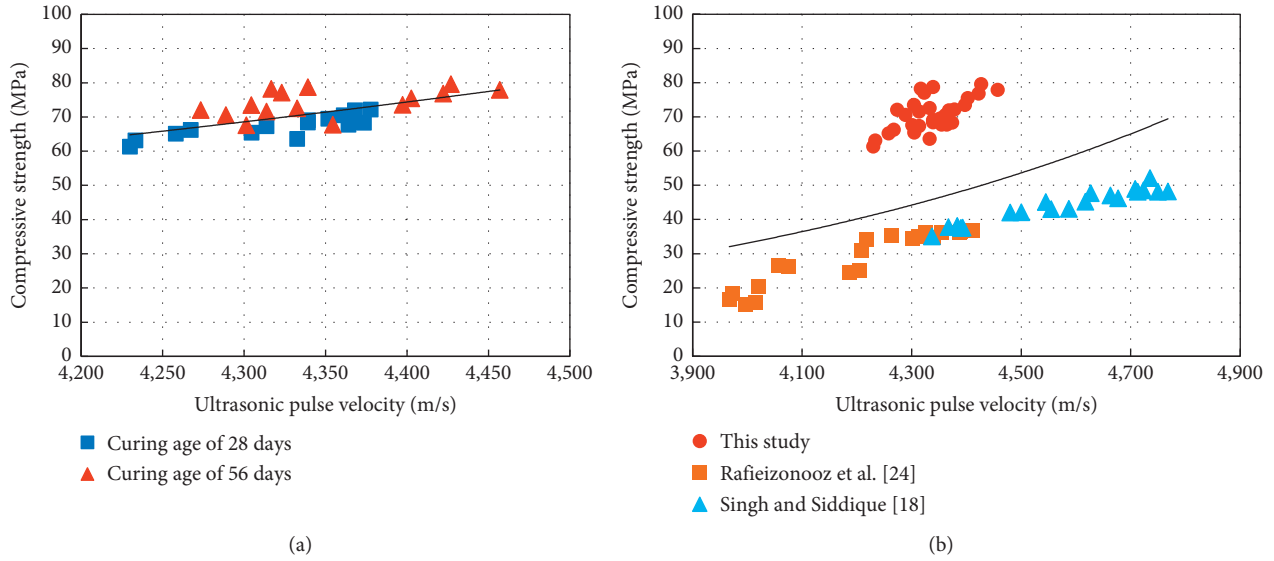
(a)

(b)

FIGURE 13: Relationship between the compressive strength and ultrasonic pulse velocity. (a) Test results in this study. (b) Test results in this study and previous studies.
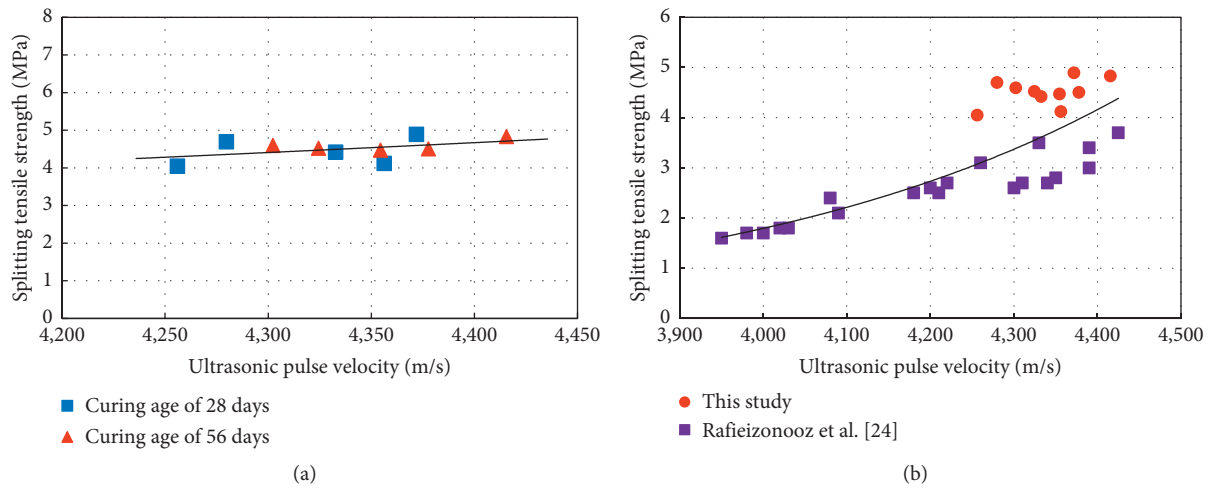

(a)

(b)

FIGURE 14: Relationship between the splitting tensile strength and ultrasonic pulse velocity. (a) Test results in this study. (b) Test results in this study and previous study.
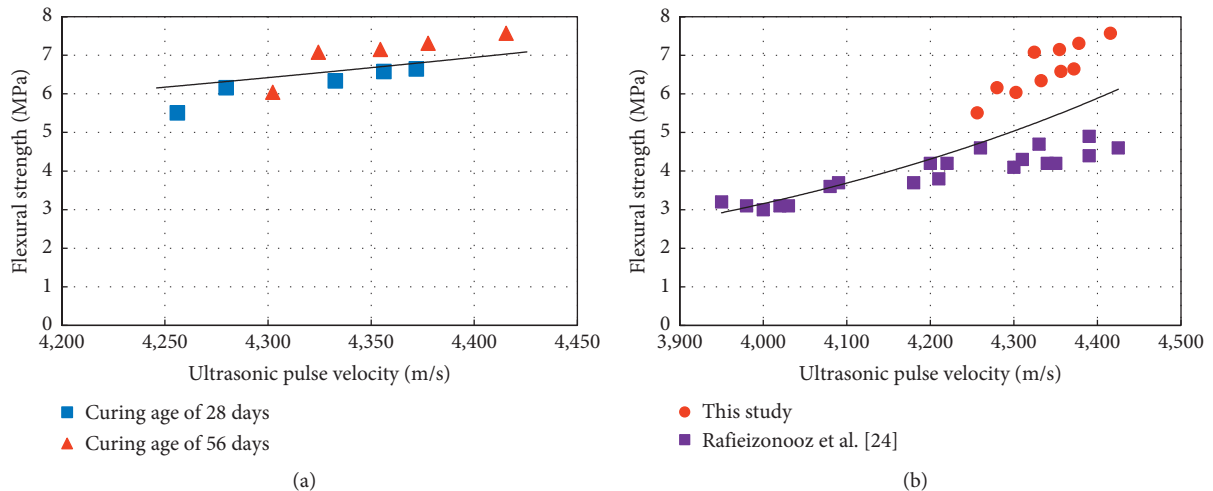

(a)

(b)

FIGURE 15: Relationship between the flexural strength and ultrasonic pulse velocity. (a) Test results in this study. (b) Test results in this study and previous study.

(2) For the CBA concrete, even if it contained total replacement for fine aggregates, the compressive strength exceeded 60 MPa. The test results implied that the CBA concrete possibly reached the level of HSC. Therefore, CBA could be utilized for fabricating HSC as a partial or total substitution for fine aggregates.

(3) Overall, replacing fine aggregates by CBA insignificantly affected the splitting tensile strength of the HSC. Particularly, at the curing age of 56 days, the splitting tensile strengths of HSC including CBA slightly reduced at the various CBA contents. However, clear reducing tendencies were observed in the flexural strengths of the CBA concrete mixtures at the curing age of 28 and 56 days.

(4) The experimental results showed that the ultrasonic pulse velocity of the HSC specimens with various CBA contents reduced by approximately 3%. This phenomenon indicated that the density of the HSC specimens decreased. Accordingly, utilizing CBA as fine aggregates in HSC would reduce the concrete strength. The test results actually showed that the strengths of the CBA concrete decreased as the ultrasonic pulse velocity of the CBA concrete decreased.

(5) Equations to predict the compressive strength, splitting tensile strength, and flexural strength of the CBA concrete by using the ultrasonic pulse velocity were suggested. The coefficient of determination in predicting the strengths of the CBA concrete was not high because the measurements in this study and in previous studies were scattered. Therefore, further extensive experimental studies are needed to improve the accuracy of the predictions.

Data Availability

The data used to support the findings of this study are available from the corresponding author upon request.

Conflicts of Interest

The authors declare that they have no conflicts of interest regarding the publication of this manuscript.

Acknowledgments

References

[1] S. Oruji, N. A. Brake, R. K. Guduru et al., "Mitigation of ASR expansion in concrete using ultra-fine coal bottom ash," *Construction and Building Materials*, vol. 202, pp. 814–824, 2019.

[2] T. Çiçek and Y. Çinçin, "Use of fly ash in production of lightweight building bricks," *Construction and Building Materials*, vol. 94, pp. 521–527, 2015.

[3] A. Abdulmatin, W. Tangchirapat, and C. Jaturapitakkul, "An investigation of bottom ash as a pozzolanic material," *Construction and Building Materials*, vol. 186, pp. 155–162, 2018.

[4] H.-K. Kim, "Utilization of sieved and ground coal bottom ash powders as a coarse binder in high-strength mortar to improve workability," *Construction and Building Materials*, vol. 91, pp. 57–64, 2015.

[5] S. Oruji, N. A. Brake, L. Nalluri, and R. K. Guduru, "Strength activity and microstructure of blended ultra-fine coal bottom ash-cement mortar," *Construction and Building Materials*, vol. 153, pp. 317–326, 2017.

[6] A. R. K. Gollakota, V. Volli, and C.-M. Shu, "Progressive utilisation prospects of coal fly ash: a review," *Science of the Total Environment*, vol. 672, pp. 951–989, 2019.

[7] V. Bruder-Hubscher, F. Lagarde, M. J. F. Leroy, C. Coughanowr, and F. Enguehard, "Utilisation of bottom ash in road construction: a lysimeter study," *Waste Management & Research*, vol. 19, no. 6, pp. 557–566, 2001.

[8] M. E. Munawer, "Human health and environmental impacts of coal combustion and post-combustion wastes," *Journal of Sustainable Mining*, vol. 17, no. 2, pp. 87–96, 2018.

[9] S. Jung and S.-J. Kwon, "Engineering properties of cement mortar with pond ash in South Korea as construction materials: from waste to concrete," *Central European Journal of Engineering*, vol. 3, pp. 522–533, 2013.

[10] N. Singh, Shehnazdeep, and A. Bhardwaj, "Reviewing the role of coal bottom ash as an alternative of cement," *Construction and Building Materials*, vol. 233, Article ID 117276, 2020.

[11] N. Singh, P. Kumar, and P. Goyal, "Reviewing the behaviour of high volume fly ash based self compacting concrete," *Journal of Building Engineering*, vol. 26, Article ID 100882, 2019.

[12] C. Argiz, A. Moragues, and E. Menéndez, "Use of ground coal bottom ash as cement constituent in concretes exposed to chloride environments," *Journal of Cleaner Production*, vol. 170, pp. 25–33, 2018.

[13] H. K. Kim and H. K. Lee, "Coal bottom ash in field of civil engineering: a review of advanced applications and environmental considerations," *KSCE Journal of Civil Engineering*, vol. 19, no. 6, pp. 1802–1818, 2015.

[14] S. Pal, M. Shariq, H. Abbas, A. K. Pandit, and A. Masood, "Strength characteristics and microstructure of hooked-end steel fiber reinforced concrete containing fly ash, bottom ash and their combination," *Construction and Building Materials*, vol. 247, Article ID 118530, 2020.

[15] Korea Environment Institute (KEI), *Minimizing Environmental Impact of Ash Treatment in Thermal Power Plants*, Korea Environment Institute, Seoul, Republic of Korea, 2019.

[16] N. Singh, M. Mithulraj, and S. Arya, "Influence of coal bottom ash as fine aggregates replacement on various properties of concretes: a review," *Resources, Conservation and Recycling*, vol. 138, pp. 257–271, 2018.

[17] L. B. Andrade, J. C. Rocha, and M. Cheriaf, "Influence of coal bottom ash as fine aggregate on fresh properties of concrete," *Construction and Building Materials*, vol. 23, no. 2, pp. 609–614, 2009.

[18] M. Singh and R. Siddique, "Properties of concrete containing high volumes of coal bottom ash as fine aggregate," *Journal of Cleaner Production*, vol. 91, pp. 269–278, 2015.

[19] J. W. Bang, G. Ganesh Prabhu, Y. I. Jang, and Y. Y. Kim, "Development of ecoefficient engineered cementitious

composites using supplementary cementitious materials as a binder and bottom ash aggregate as fine aggregate," *International Journal of Polymer Science*, vol. 2015, Article ID 681051, 12 pages, 2015.

[20] M. Singh and R. Siddique, "Effect of coal bottom ash as partial replacement of sand on workability and strength properties of concrete," *Journal of Cleaner Production*, vol. 112, pp. 620–630, 2016.

[21] N. Singh, M. Mithulraj, and S. Arya, "Utilization of coal bottom ash in recycled concrete aggregates based self compacting concrete blended with metakaolin," *Resources, Conservation and Recycling*, vol. 144, pp. 240–251, 2019.

[22] I.-H. Yang and J. Park, "A study on the thermal properties of high-strength concrete containing CBA fine aggregates," *Materials*, vol. 13, no. 7, p. 1493, 2020.

[23] M. Singh and R. Siddique, "Strength properties and microstructural properties of concrete containing coal bottom ash as partial replacement of fine aggregate," *Construction and Building Materials*, vol. 50, pp. 246–256, 2014.

[24] M. Rafieizonooz, J. Mirza, M. R. Salim, M. W. Hussin, and E. Khankhaje, "Investigation of coal bottom ash and fly ash in concrete as replacement for sand and cement," *Construction and Building Materials*, vol. 116, pp. 15–24, 2016.

[25] S. B. Park, Y. I. Jang, J. Lee, and B. J. Lee, "An experimental study on the hazard assessment and mechanical properties of porous concrete utilizing coal bottom ash coarse aggregate in Korea," *Journal of Hazardous Materials*, vol. 166, no. 1, pp. 348–355, 2009.

[26] C. Ngohpok, V. Sata, T. Satiennam, P. Klungboonkrong, and P. Chindaprasirt, "Mechanical properties, thermal conductivity, and sound absorption of pervious concrete containing recycled concrete and bottom ash aggregates," *KSCE Journal of Civil Engineering*, vol. 22, no. 4, pp. 1369–1376, 2018.

[27] W. Wongkeo, P. Thongsanitgarn, K. Pimraksa, and A. Chaipanich, "Compressive strength, flexural strength and thermal conductivity of autoclaved concrete block made using bottom ash as cement replacement materials," *Materials & Design*, vol. 35, pp. 434–439, 2012.

[28] M. H. W. Ibrahim, A. F. Hamzah, N. Jamaluddin, P. J. Ramadhansyah, and A. M. Fadzil, "Split tensile strength on self-compacting concrete containing coal bottom ash," *Procedia—Social and Behavioral Sciences*, vol. 195, pp. 2280–2289, 2015.

[29] B. Lai, J. Y. R. Liew, and A. L. Hoang, "Behavior of high strength concrete encased steel composite stub columns with C130 concrete and S690 steel," *Engineering Structures*, vol. 200, p. 109743, 2019.

[30] B. Lai, J. Y. R. Liew, and M. Xiong, "Experimental study on high strength concrete encased steel composite short columns," *Construction and Building Materials*, vol. 228, Article ID 116640, 2019.

[31] M. F. Sulaiman, C.-K. Ma, N. M. Apandi et al., "A review on bond and anchorage of confined high-strength concrete," *Structures*, vol. 11, pp. 97–109, 2017.

[32] H. K. Kim and H. K. Lee, "Use of power plant bottom ash as fine and coarse aggregates in high-strength concrete," *Construction and Building Materials*, vol. 25, no. 2, pp. 1115–1122, 2011.

[33] Korea Industrial Standard, *Standard Test Method for Compressive Strength of Concrete; KS F 2405*, Korea Industrial Standards, Seoul, Repubic of Korea, 2010.

[34] Korea Industrial Standard, *Standard Test Method for Compressive Strength of Concrete; KS F 2423*, Korea Industrial Standards, Seoul, Republic of Korea, 2016.

[35] Korea Industrial Standard, *Standard Test Method for Compressive Strength of Concrete; KS F 2408*, Korea Industrial Standards, Seoul, Republic of Korea, 2016.

[36] American Society for Testing and Materials (ASTM), *Standard Test Method for Pulse Velocity through Concrete; ASTM C597-02*, ASTM, West Conshohocken, PA, USA, 2002.

[37] K. Muthusamy, M. H. Rasid, G. A. Jokhio, A. Mokhtar Albshir Budiea, M. W. Hussin, and J. Mirza, "Coal bottom ash as sand replacement in concrete: a review," *Construction and Building Materials*, vol. 236, Article ID 117507, 2020.

[38] M. Singh and R. Siddique, "Compressive strength, drying shrinkage and chemical resistance of concrete incorporating coal bottom ash as partial or total replacement of sand," *Construction and Building Materials*, vol. 68, pp. 39–48, 2014.

[39] I. M. Nikbin, S. Rahimi, H. Allahyari, and M. Damadi, "A comprehensive analytical study on the mechanical properties of concrete containing waste bottom ash as natural aggregate replacement," *Construction and Building Materials*, vol. 121, pp. 746–759, 2016.

[40] E. Baite, A. Messan, K. Hannawi, F. Tsobnang, and W. Prince, "Physical and transfer properties of mortar containing coal bottom ash aggregates from Tefereyre (Niger)," *Construction and Building Materials*, vol. 125, pp. 919–926, 2016.